HABILITATION THESIS

FLOW HYDRODYNAMICS IN ENGINEERING and BIOMEDICAL APPLICATIONS

Dr.ing. **Sandor Ianos BERNAD**

Timişoara
2017

Submitted as **Habilitation Thesis**

by

Dr.ing. **Sandor I. BERNAD,**
Senior Researcher degree 1

Romanian Academy – Timişoara Branch
Center of Advanced Research in Engineering Sciences
B-dul. Mihai Viteazul 24, RO-300223, Timisoara
Romania

April, 2017

2017

CONTENTS

(A) REZUMAT

Teza de Abilitare

"Flow Hydrodynamics in Engineering and Biomedical Applications"

În concordanță cu legislația în vigoare, prezenta Teză de Abilitare, se bazează pe rezultatele ştiințifice în domeniile de interes al candidatului, realizate şi publicate ulterior obținerii titlului de doctor în ştiințe inginereşti, prin intermediul referințelor punctuale prezentate în cadrul lucrării de față.

Astfel,

Perioada scursă de la finalizarea tezei de doctorat (anul 2000) se concretizează prin promovarea a două direcții de cercetare şi anume:

- Hidrodinamica curgerii în aplicații industriale precum: maşini şi echipamente hidraulice, cavitație în echipamente hidraulice, unde principalele aspecte abordate au fost:

  - Modele cavitaționale (modelare numerică, validare numerică şi experimentală);
  - Cavitația în jurul profilelor hidrodinamice;
  - Cavitația în echipamente de acționare hidraulică
  - Cavitația în turbine hidraulice

respectiv,

- Aplicații biomedicale ale mecanicii fluidelor, cu precădere aplicații în domeniul curgerii în sistemul circulator uman.

Principalele realizări şi rezultatele semnificative sunt prezentate, în detaliu, în cadrul *Capitolului (b-i):Realizări ştiințifice, profesionale şi academice.*

Acest capitol prezintă exemplificat atât realizările ştiințifice în cele două direcții de activitate enumerate, cât şi activitatea de diseminare al acestor rezultate la nivel național şi internațional prin intermediul articolelor publicate în jurnale de prestigiu cât şi prin prezentarea şi publicarea rezultatelor la manifestări internaționale şi naționale de prestigiu în domeniile abordate de autor.

Dintre elemente definitorii asociate acestui capitol amintim:

1. Activiatea editorială şi publicistică: In perioada de după susținerea tezei de doctorat autorul a publicat un număr de 4 cărți de specialitate, a contribuit ca şi coautor la un număr de 4 capitole de cărți, respectiv a publicat în calitate de editor 9 volume de de cărți şi proceedings-uri de conferițe internaționale şi naționale.

2. Activitatea ştiințifică: concretizată prin intermediul următoarelor exemple, un număr de 25 de articole de jurnal indexate ISI şi BDI, 24 articole publicate în proceedings-uri indexate ISI, 26 articole publicate în proceedings-uri la conferințe intenaționale, 4 proiecte naționale în calitate de director de contract, 14 contracte cu industria în calitate de director de contract, participare ca şi membru în derularea a 10 proiecte naționale/internaționale şi 25 contracte naționale/internaționale.

3. Activitatea educațională: activitate concretizată prin îndrumarea elaborării lucrărilor de licență, masterat şi doctorat în colaborare cu Domnul Prof.dr.ing. Romeo SUSAN-RESIGA

de la Universitatea Politehnica Timişoara, Departamentul de Maşini Mecanice, Utilaje şi Transport, după cum urmează: în perioada 2009 – 2016 un număr de 4 lucrări de licență, 2 lucrări de master, comisii de îndrumare pentru elaborarea tezelor de doctorat.

Deasemenea, teză prezintă propunerea pentru evoluția carierei academice, ştiințifice şi profesionale, precum şi a direcțiilor principale de dezvoltare viitoare, în contextul realizărilor ştiințifice semnificative şi de actualitate din domeniul de specialitate al autorului.

În acest context ca şi direcții de cercetare se definesc :

1. Investigarea curgerii de tip elicoidal şi dezvoltarea bypass-ului aorto-coronarian de tip elicoidal, prin abordare următoarelor aspecte:

    a. Punerea în evidență a efectului de inhibare/reducere a fenomenului de inflamației al peretelui arterial, datorat curgerii elicoidale induse de o nouă geometrie de bypass.
    b. Coantificarea caracteristicilor curgerilor secundare în zona de impact cu peretele vascular.
    c. Corelarea parametrilor hemodinamici cu parametri morfologici si funcționali ai peretelui vascular pentru desvoltarea unor noi geometrii de bypass coronarian.

2. Investigarea curgerii în arterele sangvine supuse intervenției terapeutice de stentare, prin:

    a. Investigarea efectului prezenței stentului asupra plăcii de aterom existent.
    b. Investigarea şi prognozarea poziționării optime al stentului astfel încât să se minimizeze efectul secundar negativ de infalmație post procedură de stentare.
    c. Investigarea procelui de dozare locală a medicație prin procedeul de “drug targeting”.

În ultima parte a lucrării, autorul prezintă propria viziune de dezvoltare academică şi profesională, bazându-se atât pe experiența de 17 ani acumulată în domeniul hidrodinamicii curgerii fluidelor complexe, cât şi în baza tratatelor de specialitate de ultimă oră cu privire la modul de pregătire şi implementare a unor strategii care să asigure o evoluție profesională de calitate şi cu impact ridicat atât în mediul academic cât şi în mediul economic.

Autorul prezintă câteva direcții concrete de acțiune precum:

1. Dezvoltarea unui suport logistic şi de personal în vederea creării premizelor necesare pentru obținerea rezultatelor scontate in direcțiilor de dezvoltare stabilite.
2. Recrutarea, dezvoltarea şi specializarea unui personal de calitate care să asigure continuitatea activităților atât la nivel academic cât şi la nivel ştiințific.
3. Crearea unui context facil pentru crearea unei mase critice de calitate care să permită câştigarea recunoştinței nivelului ştiințific atât la nivel internațional cât şi național.

(A) ABSTRACT

Habilitation Thesis

"Flow Hydrodynamics in Engineering and Biomedical Applications"

In agreement with the legislation in force, this sentence of empowerment, is based on scientific results in the fields of interest of the candidate and published at a later date to obtain the title Ph.D. in Engineering Sciences, through specific references presented in the thesis.

Thus, the period which has elapsed since the completion of my Ph.D. thesis (2000) is materialized through the promotion of research in two directions:

- Flow hydrodynamics in industrial applications such as hydraulic machinery and equipment, cavitation in hydraulic equipment, where the main issues addressed were:
  - Cavitation model (numerical modeling, numerical and experimental validation of the model);
  - Cavitation around the hydrofoil;
  - Cavitation in the hydraulic equipments;
  - Cavitation in hydraulic turbines.

- Biomedical Applications of the fluid mechanics, especially fluid flow in the human circulatory system.

The main achievements and significant results are presented in detail, within the framework of Chapter II (b): *Scientific, professional and academic achievements*.

This chapter presents scientific achievements exemplified for the both directions of activity listed, as well as dissemination activity of these results at national and international level through articles published in prestigious journals and through the presentation and publication of the results at national and international events in the areas addressed by the author.

Defining elements associated with this chapter are:

1. Editorial and publishing activity: in the period after defense the PhD thesis, the author has published four books, contributed as co-author of a some of four books chapter, published as editor a some of nine books and proceedings of international and national conferences.

2. Scientific activity: My research activity is emphasised by the publication of a number of 25th articles indexed in ISI or BDI journals, a number of 24 articles indexed in ISI proceedings, a number of 26 articles published in Proceedings of the International Conferences, 4 national projects as project director, 12 contracts with industry as contract director, member in the 10 national and/ or international projects and 25 national/international contracts.

3. Educational Activity: co-adviser for bachelor, master and thesis in collaboration with Prof.dr.ing. Romeo SUSAN-RESIGA from Politehnica University Timişoara, Department of Mechanical Machines, Equipment and Transportation, as follows: in the period from 2009-2016 some four bachelor thesis, two masters thesis, and active member of the guidance committees for the preparation of the Ph.D. thesis.

The habilitation thesis, also presents the proposal for academic, scientific and professional career evolution, and the main directions of future development in the context of significant scientific achievements in field of the topic of the author.

In this context, the following research directions are defined:

1. Helical type flow investigation and developing of the new aorto-coronary bypass graft, approaching the following issues:
   - Put in evidence the advantages of the helical geometry, namely provide evidence that swirl flow generates by the helical graft operate to inhibit the development of vascular diseases such as thrombosis, atherosclerosis, and intimal hyperplasia.
   - Investigation of the swirling characteristics of the secondary flow produced by helical graft tube with various shapes.
   - Investigation of the helical graft geometries both by numerical simulation and experimental measurements for different geometrical configurations (different turns and helix amplitude, anastomosis angle, bypass graft diameter, a combination of the successive helix with various aspects of the helix amplitude).

2. Investigation of blood flow in the arteries subjected to therapeutic intervention of stenting through:
   - Investigation of the three-dimensional stent model is required to capture spatial variations of flow hydrodynamics and drug distributions.
   - Development and investigations a stent should provide optimum vessel coverage to ensure that the vessel tissue does not prolapse between the stent struts; however, a low artery-stent contact surface area should also be maintained, because the foreign material of the stent can initiate an aggressive thrombotic response.
   - Investigations of the complex interplay between stent design (distribution of struts, link design, strut thickness, and circumferential ring design) and stent performance, from the perspective of the drug delivery performance.

In the last part of the thesis, the author presents his own vision of academic and professional development, from both the perspective of the 17-year experience gained in the field of hydrodynamics, fluid flow and also based on the latest international results in preparation and implementation of strategies to ensure a high-quality professional development, and high-impact in academia and in the economic environment.

The author presents several directions of action such as:

1. Recruit, Retain and develop a cadre of brilliant researchers and academic staff.
2. Establish and support the next generation of senior researcher and scientific leaders.
3. Build sufficient capacity and expertise to support new/challenging research themes, in my field of specialization.
4. Create and develop laboratory facilities and learning environments to provide world-class research facilities while simultaneously creating modern, flexible education instructional spaces.

Based on the foundation and my scientific activity, I shall be able to achieve, consolidate and develop the goals presented in this thesis, thus contributing to outlining my academic personality and not least, to honour the institution that trained me, to be able to believe that my purpose is to add a plus to the prestige of its professors.

(B) ACHIEVEMENTS AND DEVELOPMENTS PLANS

(b-i) Scientific, professional and academic achievements

(b-i)_01 Summary of my professional, scientific, and academic career

The academic and professional career splits in two parts, namely over a period of the **6 years before** the PhD Thesis defence (September 1994 ÷ November 2000), and a period of the **16 years after the PhD Thesis defence (December 2000 ÷ March 2017)**.

Before PhD thesis defense	Professional career	- September 1995 – September 1996, Mechanical Engineer, Department of hydraulic power system, Machine Building Factory UMT, Timisoara, Romania. - July 1995, Master in Science, Master program in hydrodynamics of machines and systems, "Politehnica" University of Timisoara - June 1994, Mechanical Engineering Diploma, Technical University of Timisoara

	Academic career	- October 1996 – October 1998, Assistant Professor, Mechanical Engineering School, Hydraulic Machinery Department "Politehnica" University of Timisoara, Teaching applications in:
		  - Fluid Mechanics: Fall 1996, Spr 1997; Fall 1997
		  - Numerical Methods in Mechanical Engineering – Programing with Pascal: Spr 1996, Fall 1997, Spr 1998;
		  - Hydraulic Power Systems, Fall 1997, Spr 1997, Fall 1998.

	Scientific career	- November 2000, PhD in Mechanical Engineering, PhD thesis "Hydraulic poppet valve optimization for stationary and transient regim" graduated with cum Laude, thesis advisor Acad.Prof.Dr.Doc.Ing. Ioan Anton, according to the Ord. of the Min. of Education and Research nr. 3467/16.03.2001. - October 1996 – November 2000, PhD program in hydrodynamics of machines and systems, "Politehnica" University of Timisoara. Scientific results (1996 – 2000) (Figure 1): ➢ Papers indexed in BDI journals: 3 ➢ Papers in national journals: 1 ➢ Papers in international conference proceedings: 3 Short Term Professional Visits (1996 - 2000): ❖ September, 1997 – University "Albert Szentgyorgyi" Szeged, Hungary, Department of Informatics

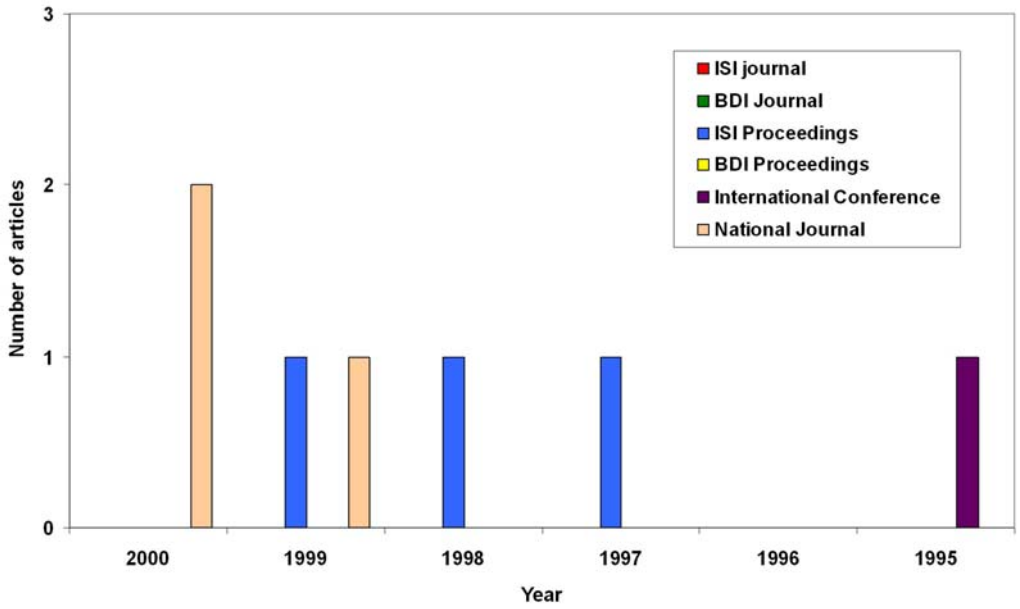

Figure 1. Articles publication evolution before PhD Thesis defence **(period 1995 – 2000)**.

After PhD thesis defense

Professional career	- 2014 – to date, Senior Researcher, grade I, Romanian Academy – Timisoara Branch - 2007 – 2014, Senior Researcher, grade II, Romanian Academy – Timisoara Branch - 2002 – 2007, Senior Researcher, grade III, Romanian Academy – Timisoara Branch
Academic career	- July 2002 – to date, Executive Director, Research Center for Engineering of Systems for Complex Fluids, University Politehnica Timisoara. - May 2001 – June 2002, Administrative Director, National Center for Engineering of Systems for Complex Fluids, ”Politehnica” University of Timisoara.
Scientific career	Short Term Professional Visits (2001 to date): ❖ July, 2005 - CISM International Center for Mechanical Sciences, Udine, Italy ❖ October, 2002 - SimTec Ltd., Software & Services for Design and Development, Thessaloniki, Grecee Summary of the scientific results (2001 to date) (Figure 2): ➢ Papers in ISI/BDI journals: 14 / 14 ➢ Papers in ISI / BDI conference proceedings: 24 / 6 ➢ Papers in international conference proceedings: 26 ➢ Papers in national journals: 40 ➢ Books/Books chapter/Editors: 2 / 4 / 9 ➢ Citations in ISI/BDI journals: 61 / 8

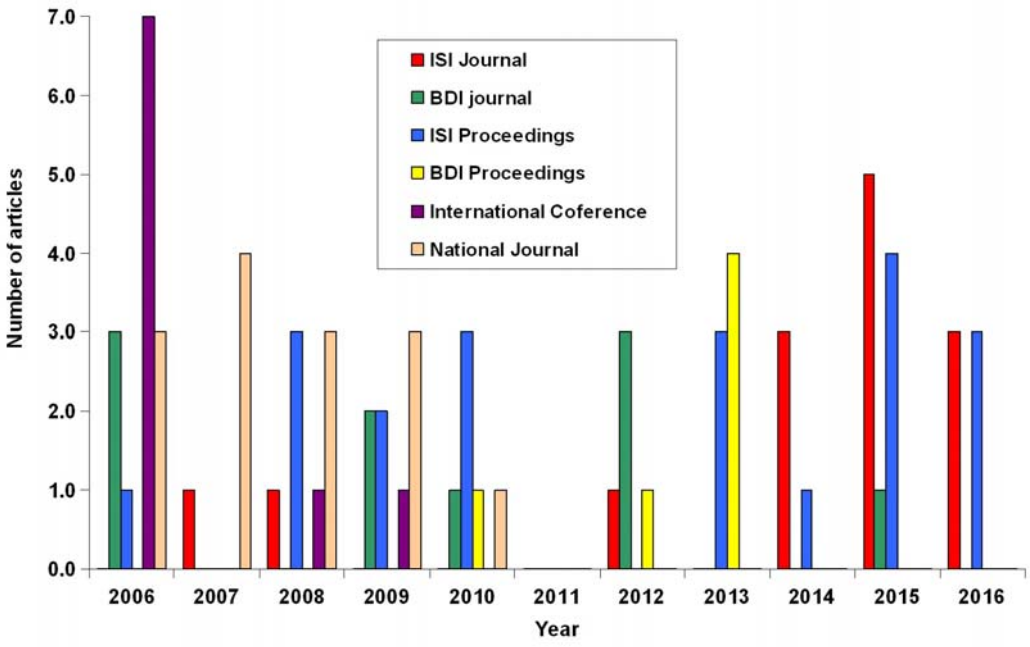

Figure 2. Evolution of the articles publications in the last ten years **(period: 2006 – 2016)**.

Ability to transfer knowledge and results to the economic or social environment and dissemination of my scientific results

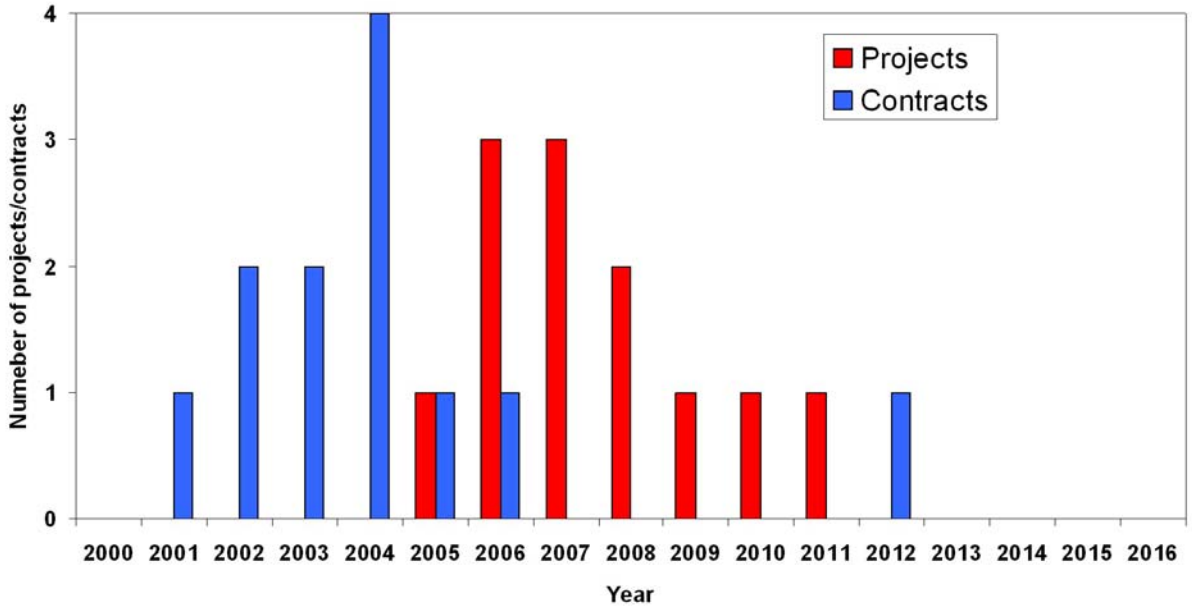

Figure 3. Projects and grants conducted as director after PhD Thesis defence **(period: 2001 – 2016)**

Ability to tutor students, young specialists, researchers and PhD students

Bachelor Student Advised

- Summer 2016: Claudia Hudrea (collaboration with University of medicine and Pharmacy Timisoara, Department of Cardiology, co-adviser Prof.dr. Dan Gaiță).
- Summer 2010: Alin Totorean (collabotation with Politehnica University Timisoara, Faculty of Mechanical Engineering, Department of MMUT, co-adviser Prof.dr.ing. Romeo Susan-Resiga).
- Summer 2010: Vlad Vânătu (collabotation with Politehnica University Timisoara, Faculty of Mechanical Engineering, Department of MMUT, co-adviser Prof.dr.ing. Romeo Susan-Resiga).
- Summer 2009: Alexandra Ersek ((collabotation with Politehnica University Timisoara, Faculty of Mechanical Engineering, Department of MMUT, co-adviser Prof.dr.ing. Romeo Susan-Resiga).

M.S. Student Advised

- Summer 2014: Andreea Daogaru (collabotation with Politehnica University Timisoara, Faculty of Mechanical Engineering, Department of MMUT, co-adviser Prof.dr.ing. Romeo Susan-Resiga).
- Summer 2012: Alin Totorean (collabotation with Politehnica University Timisoara, Faculty of Mechanical Engineering, Department of MMUT, co-adviser Prof.dr.ing. Romeo Susan-Resiga).

Ability for teamwork and scientific collaboration efficiency:

The ability for teamwork demonstrated in:

1. Research project (example as director or partner responsible):
   - Collaborative Research Project CEEX-M1-C2-1180, contract VIASAN no: 81/2006, *Fundamental research regarding the particular aspects associated with the blood flow in the pathology of the human circulatory system with quantification of their implications on the placental circulation – CARDIOCOMP*, period 2006-2008, (coordinator: Romanian Academy – Timisoara Branch, P1 – University Politehnica Timisoara, P2 – University Politehnica Bucharest REOROM Laboratory, P3 – University of Medicine and Pharmacy „Victor Babes" Timisoara, P4 – Institute of Cardiology Timisoara).
   - Collaborative Research Project CEEX-M1-C2-2566 - THARVEST, contract AMCSIT no. 192/2006, *Interinfluence of the vertical axis, stabilized, Achard type hydraulic turbines - THARVEST*, period 2006-2008 (coordinator: University Politehnica Bucharest, P1 – University of Civil Engineering Bucharest, P2 – Romanian Academy – Timisoara Branch).

2. As the organizer of the scientific conferences (example):
   - *25nd IAHR Symposium on Hydraulic Machinery and Systems*, Timisoara, 20-24 Sept. 2010, with 154 participants from 18 countries;
   - *2nd IAHR International Meeting of the Workgroup on Cavitation and Dynamic Problems in Hydraulic Machinery and Systems*, Timisoara, 24-26 Oct. 2007, with 56 participants from 9 countries.

(b-i)_02. Research Results in Hydrodynamics, Cavitation and Biomedical Applications

Articles constituting support for the habilitation thesis

The present habilitation thesis is a survey of the scientific results obtained in the field of the hydrodynamics and cavitation in hydraulic equipment and biomedical applications of the fluid dynamics respectively, based on the following representative articles:

Hydrodynamics

1. **BERNAD Sandor,** SUSAN-RESIGA Romeo, (2012), Numerical Model for Cavitational Flow in Hydraulic Poppet Valves, Modelling and Simulation in Engineering, Volume (2012), Article ID 742162, 10 pages, ISSN: 1687-5605, doi:10.1155/2012/742162, http://dx.doi.org/10.1155/2012/742162.
2. **Bernad S.**, Susan-Resiga R., Muntean S., Anton I., (2007), Cavitation phenomena in hydraulic valves. Numerical modelling, Proceedings of the Romanian Academy, Series A, Vol. 8, No. 2, pp: 117-126. ISSN 1454-8267, **(WOS: 000255027200010, IF = 1.735)**.
3. **Bernad S**, Georgescu A, Georgescu SC, Susan-Resiga R, Anton I, (2008), Flow investigations in Achard turbine, Proceedings of the Romanian Academy, Series A-Mathematics Physics Technical Sciences Information Sciences, vol 9, no 2, pp:129-140, ISSN 1454-8267, **(WOS: 000259537100008, IF = 1.735)**.

Biomedical Applications

4. **Sandor I. Bernad**, Alin F. Totorean, Ladislau Vekas, (2016), Particles deposition induced by the magnetic field in the coronary bypass graft model, Journal of Magnetism and Magnetic Materials, 2016, vol 401, pp: 269-286, doi:10.1016/j.jmmm.2015.10.020, **(WOS: 000366585200041, IF = 2.357)**.
5. Alin F.Totorean, **Sandor I. Bernad**, Romeo F. Susan-Resiga, (2016), Fluid dynamics in helical geometries with applications for by-pass grafts, Applied Mathematics and Computation, vol 272 part 3, pp: 604-613, http://dx.doi.org/10.1016/j.amc.2015.05.030, **(WOS: 000364991600004, IF =1.345)**.
6. **Sandor I. Bernad**, Alin I. Bosioc, Elena S. Bernad, Marius L. Craina, (2015), Helical type coronary bypass graft performance: Experimental investigations, Bio-Medical Materials and Engineering, vol. 26, no. s1, pp: 477-486, http://dx.doi.org/10.3233/BME-151337, **(WOS: 000361671800055, IF = 0.988).**
7. Alin F. Totorean, Alin I. Bosioc, **Sandor I. BERNAD**, Romeo Susan-Resiga, (2015), Critical flow regions in the coronary by-pass graft anastomosis, Proceedings of the Romanian Academy, Series A, vol 16, no 2, pp: 201–208, ISSN 1454-8267, **(WOS: 000357362300011, IF = 1.735)**.
8. Elena S. Bernad, **Sandor I. Bernad**, Marius L. Craina, (2014), Hemodynamic parameters measurements to assess severity of serial lesions in patient specific right coronary artery, Bio-Medical Materials and Engineering, Vol. 24, No. 1, pp: 323-334, DOI: 10.3233/BME-130814, ISSN: 0959-2989, **(WOS: 000327312600039, IF = 0.988)**.
9. **Sandor I. Bernad**, Alin Bosioc, Elena S. Bernad, Marius L. Craina, (2014), Comparison between experimentally measured flow patterns for straigth and helical type graft, Bio-Medical Materials and Engineering, Vol. 24, No. 1, pp: 853-860, DOI: 10.3233/BME-130877, ISSN: 0959-2989, **(WOS: 000327312600098, IF = 0.988)**.
10. A.F. Totorean, A.I. Bosioc, **S.I. Bernad**, R. Susan-Resiga, (2014), Identification an visualization of the vortices in by-pass graft flow, Proceedings of the Romanian Academy, Series A: Mathematics, Physics, Technical Sciences, Information Science, vol 15, no 1, pp:52-59, **(WOS: 000333795600007, IF = 1.735)**.

(b-i)_1 The research activity and achievements in the thematic direction of:

Hydrodynamics and cavitation in the hydraulic equipment (Post-PhD Thesis period)

Scientific activity related to the topic of the "Hydrodynamics and cavitation"

❖ **Journal articles** (selection)**:**

1. **BERNAD Sandor**, SUSAN-RESIGA Romeo, MUNTEAN Sebastian, (2012) Two-Phase Cavitating Flow in Turbomachines, Research Journal of Applied Sciences, Engineering and Technology 4(22), 4685-4695, http://maxwellsci.com/jp/abstract.php?jid=RJASET&no=232&abs=18 **(SCOPUS)**.
2. **BERNAD Sandor**, SUSAN-RESIGA Romeo, Numerical Model for Cavitational Flow in Hydraulic Poppet Valves, Modelling and Simulation in Engineering, Volume (2012), Article ID 742162, 10 pages, doi:10.1155/2012/742162, 2012, **(SCOPUS)**.
3. **Bernad S**, Georgescu A, Georgescu SC, Susan-Resiga R, Anton I, (2008), Flow investigations in Achard turbine, Proceedings of the Romanian Academy, Series A-Mathematics Physics Technical Sciences Information Sciences, vol 9, no 2, pp:129-140, ISSN 1454-8267, **(WOS: 000259537100008, IF = 1.735)**.
4. **Bernad S.**, Susan-Resiga R., Muntean S., Anton I., (2007), Cavitation phenomena in hydraulic valves. Numerical modelling, Proceedings of the Romanian Academy, Series A, Vol. 8, No. 2, pp: 117-126. ISSN 1454-8267, **(WOS: 000255027200010, IF = 1.735)**.
5. **Bernad S**, Susan-Resiga R, Muntean S, Anton I., (2006), Numerical analysis of the cavitating flows. Proceedings of the Romanian Academy, Series A: Mathematics, Physics, Technical Sciences, Information Science, 7(1):1–13, **(ISI master journal list)**.

❖ **Articles in international and national conference proceedings** (selection):

1. **Bernad S.I.**, Georgescu A., Georgescu S., Resiga R., (2008), Numerical Investigation of the Unsteady Flow in the Achard Turbine, In New Aspects of Fluid Mechanics and Aerodynamics" WSEAS Mechanical Engineering Series WSEAS Press, ISSN 1790-5095, ISBN 978-960-6766-98-5, pp. 59-65, **(WOS:000260495700005)**.
2. **Bernad S.**, Susan-Resiga R., Muntean S., Anton I., (2004) Numerical Simulation of Two-Phase Cavitating Flow in Turbomachines, Scientific Bulletin of the 'Politehnica' University of Timisoara, Transactions on Mechanics, Tom 49(63), Special Issue, pp: 439- 446, ISSN 1224-6077.
3. R. Susan-Resiga, S. Muntean, **S. Bernad**, I. Anton, (2003), Numerical investigation of 3D cavitating flow in Francis turbines. Proceedings of the Conference on Modelling Fluid Flow [CMFF'03], Budapest, Hungary, September 2003, pp: 950-957, 2003, ISBN 963 420 778 2.
4. **Bernad S.**, Susan-Resiga R., Anton I., Ancuşa V., (2001), Vortex Flow Modeling Inside The Poppet Valve Chamber, Proceedings of the Bath Workshop on Power Transmission & Motion Control, PTMC 2001, In Fluid Power Series, Series Ed. Prof. C.R. Burrows, Research Studies Press LTD, Taunton, Somerset, England, pp: 161-176, 2001, ISBN 0 86380 107 2, **(WOS:000173073000012)**.

❖ **Books and book chapters:**

Books:

1. **Sandor I. Bernad**, Hidrodinamica echipamentelor de reglare pentru actionari hidraulice, Editura Orizonturi Universitare, 2005, (224 pp.), ISBN 973-638-249-4. (in Romanian). (National Library of Romania, cota III 279564).

2. Susan-Resiga R., **Bernad S.**, Muntean S. (Editors), (2007), *Vortex Hydrodynamics and Applications*, Eurostampa Publishing House, (492 pp.), ISBN: 978-973-687-659-2, (National Library of Romania, cota IV 78273).

Book chapters:

1. Resiga R., Muntean S., **Bernad S.**, Balint D., Balint I., Modern methods for fluid flow simulation using parallel computing. Orizonturi Universitare Publishing House, (296 pp.), ISBN 973-638-064-5, 2003. (in Romanian), (personal contribution: chapter 4 – 45 pages), (National Library of Romania, cota III 259590).
2. Hodor V., Bode F., Vaida L.I., Vaida C., Opruta D., Baran G., Bunea F., Oprina G., **Bernad S.I.** Chapter 8. Vortex Flows in fluid Equipments, pp: 387-427; pages 40. In Susan-Resiga R., Bernad S., Muntean S. (Editors): Vortex Hydrodynamics and Applications, Eurostampa Publishing House, Timisoara, 2007, (personal contribution 10 pages), (National Library of Romania, cota IV 78273).

❖ Editor of the conference proceedings:

1 Susan-Resiga R., Muntean S., **Bernad S.**, (Editors), (2010), *Proceedings of the "25nd IAHR Symposium on Hydraulic Machinery and Systems"*, Timisoara, 20-24 Sept. 2010, in Institute of Physics. Conference Series Earth and Environment Science, Issue 12, ISSN 1775-1315. (http://iopscience.iop.org/1755-1315/12/)

2 Georgescu A.M, Georgescu Sanda-C, **Bernad S.**, (Editors), (2008), *Proceedings of the* 4td Workshop on Vortex Dominated Flows. Achievements and Open Problems", Bucuresti, 12 - 13 sept. 2008, in Scientific Bulletin of the "Politehnica" University of Timisoara, Transactions on Mechanics, Issue 3, Tom 53(67), ISSN 1224-6077.

3 Susan-Resiga R., **Bernad S.**, Muntean S. (Editors), (2007), *Proceedings of the "2nd IAHR International Meeting of the Workgroup on Cavitation and Dynamic Problems in Hydraulic Machinery and Systems*, Timisoara, 24-26 Oct. 2007, in Scientific Bulletin of the "Politehnica" University of Timisoara, Transactions on Mechanics, Issue 6, Tom 52(66), (244 pp.), ISSN 1224-6077.

4 **Bernad S.**, Muntean S., Susan-Resiga R. (Editors), (2007), *Proceedings of the "3rd Workshop on Vortex Dominated Flows. Achievements and Open Problems*", in Scientific Bulletin of the "Politehnica" University of Timisoara, Transactions on Mechanics, Issue 3, Tom 52(66), (158 pp.), ISSN 1224-6077.

5 **Bernad S.**, Muntean S., Susan-Resiga R. (Editors), (2006), *Proceedings of the 2nd Workshop on Vortex Dominated Flows Achievements and Open Problems*, in Scientific Bulletin of the "Politehnica" University of Timisoara, Romania, Transactions on Mechanics, Special Issue, (196 pp.), ISSN 1224-6077.

6 **Bernad S.**, Muntean S., Susan-Resiga R. (Editors), (2005), *Proceedings of the Workshop on Vortex Dominated Flows Achievements and Open Problems*, in Scientific Bulletin of the "Politehnica" University of Timisoara, Romania, Transactions on Mechanics, Special Issue, (214 pp.), ISSN 1224-6077.

7 R. Susan-Resiga, **Bernad S.**, Muntean S., Popoviciu M. (Editors), (2004), *Proceedings of the 6th International Conference on Hydraulic Machinery and Hydrodynamics*, Scientific Bulletin of the 'Politehnica' University of Timisoara, Romania, Transactions on Mechanics, Tom 49(63), Special Issue, (740 pp.), ISSN 1224-6077.

8 Anton I., Resiga R., Sofonea S., **Bernad S.**, Muntean S., (Editors), (2003), *Proceedings of Workshop on Numerical Methods in Fluid Mechanics and FLUENT Applications*, Orizonturi Universitare Publishing House, (312 pp.), ISBN 973-638-022-X.

❖ Conference committees:

1. The 25nd IAHR Symposium on Hydraulic Machinery and Systems, Timisoara, 20-24 Sept. 2010.

2. The 4td Workshop on Vortex Dominated Flows. Achievements and Open Problems, Bucuresti, 12 - 13 sept. 2008.
3. The 2nd IAHR International Meeting of the Workgroup on Cavitation and Dynamic Problems in Hydraulic Machinery and Systems, Timisoara, 24-26 Oct. 2007.
4. The 3rd Workshop on Vortex Dominated Flows. Achievements and Open Problems, Timişoara, June 1-2, 2007.
5. the 6th International Conference on Hydraulic Machinery and Hydrodynamics, Timişoara, 21-22 October 2004.

❖ **Research projects** (selection)**:**

1. **Bernad S.**, Resiga R., Muntean S., Balint D., Frunza T., Mathematical models and numerical simulation for two-phase cavitating flows with industrial and biomedical applications. National Research Project no. 730, period 2005-2007. Total value: 58.000 RON. **(Project director)**.
2. **Bernad S.**, Muntean S., Anton L., Baya A., Balint D., Stuparu A., Collaborative Research Project CEEX-M1-C2-2566 - THARVEST, contract AMCSIT no. 192/2006, Interinfluence of the vertical axis, stabilized, Achard type hydraulic turbines - THARVEST, period 2006-2008. Total value: 200.000 RON. **(Coordinator of the partner nr. 2: Romanian Academy – Timisoara Branch).**
3. Susan-Resiga R., Muntean S., L. Vekas, Bica D., **Bernad S.**, Balint D., Stuparu A., Giula G., Turbomachinery swirling flow optimisation and control with technology of magnetorheological fluid systems. SWISS National Science Fundation, Grant SCOPES 2006-2008, IB7320-110942/1, period 2006-2008. Total value: 54.000 CHF. **(Research team member)**.
4. Resiga R., Muntean S., **Bernad S.**, Hasmatuchi V., Taming the Vortex Rope Project – TAVORO, Contract UPT nr. 5214/19.04.2007, beneficiary: General Electric Hydro Canada, period 2007-2008. Total value: 7.500 USD **(Research team member)**.
5. Resiga R., Bernad S., **Muntean S.**, Thermo-hydrodynamic optimization of a cooling cell with partial cross-walls, Contract UPT nr. 16126/21.12.2005, beneficiar SIEMENS VDO Automotive, Germany, January-march 2006. Total value: 5.400 EUR. **(Research team member)**.
6. Anton I, Susan-Resiga R., **Muntean S.**, Bernad S., Modelarea numerică şi analiza curgerilor cavitaționale bifazice în turbinele hidraulice, Grantul Academiei Române, (Gar 103/2004, Gar 362/2003), period: 2003-2004. Total value: 6.000 RON. **(Research team member)**.

Summary of the research activity in the field of the "Hydrodynamics and cavitation" in period 2000-2013:

1	**Journal articles**	ISI:	2	First or corresponding author
		BDI:	5	First or corresponding author
		National:	27	Firs or author
2	**Conference articles**	ISI:	3	First author
		BDI:	0	-
		International (non BDI):	15	Firs or author
3	**Projects**	National:	2	Director or partner responsible
		International:	1	member
4	**Contracts**	National:	12	Director
		International:	4	member

Introduction

In many engineering applications, cavitation has been the subject of extensive theoretical and experimental research since it has predominantly been perceived as an undesirable phenomenon. This is mainly due to the detrimental effects of cavitation such as erosion, noise, and vibrations, caused by the growth and collapse of vapor bubbles.

The ability to model cavitating flows has drawn keen interest in CFD community. It covers a broad range of applications, such as pumps, hydraulic turbines, inducers and fuel cavitation in orifices as commonly encountered in fuel injection systems.

Fluid machinery is a common application where low pressures are routinely generated by the machine action, e.g. on blade surfaces, with a consequent possibility of cavitation. The existence of cavitation is often undesired because it can degrade the device performance, pro¬duce undesirable noise, lead to physical damage to the device and affect the structural integrity. Details of the existence, extent and effects of cavitation can be of significant help during the design stages of fluid machinery, in order to minimize cavitation or to account for its effects and optimize the design.

Past several decades have seen considerable research on cavitation and extensive reviews are available in the literature [1-3]. Different aspects of this complex phenomenon have been explored, including, e.g., cavitation bubble collapse [4] and erosion damage, cavitation acoustics, cloud cavitation [4, 5], and rotating cavitation [6, 7].

Based on the assumption that the flow is inviscid, various numerical methods have been thus far proposed to simulate cavitating flows; the conformal mapping method, the singularity method, and the panel method. The flow around hydrofoil [8 - 10] and within a centrifugal impeller [11] could be calculated using these inviscid flow models. Experimental observations have revealed that the cavitation appearance relates closely to the viscous phenomena of the liquid-phase, such as the boundary layer and the vortex motion. Recently, viscous flow models, which regard the cavitating flow as the bubbly flow containing spherical bubbles, were introduced to provide highly accurate calculations. In the viscous flow models, the Navier-Stokes equation including cavitation bubble is solved in conjunction with Rayleigh's equation governing the change in the bubble radius. Kubota et al. [9] analyzed the flows around a hydrofoil by the Finite Difference method, and Bunnell et al. [12] calculated the flow in a fuel injection pump for diesel engines by the control volume method. The predominating regions of high volumetric fraction of bubbles obtained by these methods agree well with the cavitation regions observed experimentally.

To account for the cavitation dynamics in a more flexible manner, recently, a transport equation model has been developed. In this approach volume or mass fraction of liquid (and vapor) phase is convected. Singhal et al. [3], Merkle et al. [15] and Kunz et al. [16] have employed similar models based on this concept with differences in the source terms. Merkle et al. [15] and Kunz et al. [16] have employed the artificial compressibility method. Kunz et al. [16] have adopted a non-conservative form of the continuity equation and applied the model to different geometries. Their solutions are in good agreement with experimental measurements of pressure distributions.

The present work addresses the computational analysis of sheet hydrofoil cavitation. Other types of cavitation that occur with sheet cavitation include cloud and bubble cavitation. Sheet Cavitation is very common on hydraulic machinery, and the present study was motivated by exploring the literature concerning the experimental observations and theoretical aspects. A sheet cavity is characterized by a distinct thin vapor bubble attached to the blade surface. Over the years several models have been developed that describe finite cavities. These are characterized by the manner in which the cavity is terminated.

Two-phase cavitating flow models based on homogeneous mixture approach, with a transport equation for the vapor volume fraction, have been included in expert commercial codes such as FLUENT [17]. We first evaluate this model for the benchmark problem of a blunt cavitation and compare the numerical results with experimental data of Rouse & McNown [18]. We have performed such an evaluation for the hemispherical cavitator in [19]. Second, we address the computational analysis of sheet hydrofoil cavitation. The test case corresponds to an NACA 0009 isolated hydrofoil, where experimental data are available in [20].

We conclude that for steady cavitating flow, the model evaluated in this paper correctly captures the pressure distribution on the hydrofoil.

The current effort is based on the application of the recently developed full cavitation model that utilizes the modified Rayleigh-Plesset equations for bubble dynamics and includes the effects of turbulent pressure fluctuations and non-condensible gasses (ventilated cavitation) to rotating cavitation in different types of fluid turbomachines.

Cavitating flow modeling

Cavitating flow is very sensitive to the formation and transport of vapor bubbles, the turbulent fluctuations of pressure and velocity and to the magnitude of non-condensible gasses, which are dissolved or ingested in the operating liquid [13], [21].

Numerical simulation of two-phase cavitating flows is an ongoing research effort with the ambitious goal to compute the unsteady evolution for cavities grow and collapse. The CFD community has developed so far a set of mature techniques for simulating single-phase viscous flows, and the past half century of accumulated experience may very well serve to shape the numerical cavitating flow research. Early studies rely on the potential flow theory [22]. This approach is now able to correctly describe partially cavitating two-dimensional hydrofoils, including the re-entrant jet cavity closure model [23]. However, an extension to 3D problems and other types of cavitating flows seems to be out of reach for the potential flow model.

Although basic cavitation theoretical studies deal with bubble (or bubble clouds) dynamics by solving for the vapour-liquid interface, most of the practical cavitating flows are approached using a homogeneous flow theory. The main idea is to consider a single variable density fluid, without explicit phase interfaces. This model has emerged after carefully examining available experimental investigations, as well as by evaluating the computational costs involved in cavitating flows modeling. A review of cavitating flows numerical studies over the past decade can be found in [5], where various Reynolds Averaged Navier-Stokes (RANS) solvers have been modified to account for the secondary phase (vapor and gas) dynamics.

The mixture model is used in the current work for the numerical simulation of cavitating flows with the FLUENT expert code [17]. In this model, the flow is assumed to be in thermal and dynamic equilibrium at the interface where the flow velocity is assumed to be continuous.

The mixture is a hypothetical fluid with variable density,

$$\rho_m = \alpha \rho_v + (1-\alpha)\rho_l \ , \tag{1}$$

ranging from liquid density for $\alpha = 0$ to vapour density ρ_V for $\alpha = 1$. The vapour volume fraction

$$\alpha = \frac{Vol_{vapor}}{Vol_{liquid} + Vol_{vapor}} \ , \tag{2}$$

is an additional unknown of the problem. The mixture will of course satisfy the continuity equation

$$\frac{d\rho_m}{dt} + \rho_m \nabla \cdot \mathbf{u}_m = 0 \, , \tag{3}$$

where d/dt denotes the material derivative. Next, one has to consider a momentum equation for the mixture. A simple choice would be to neglect the viscous effects and use the Euler equation. The system of equations can be then closed with a relationship density-pressure (equation of state). This approach can take advantage of a reach legacy of inviscid compressible solvers [24]. However, when considering a barotropic mixture, i.e. the density depends solely on the pressure, some physics is lost. This can be easily seen when writing the vorticity transport equation

$$\frac{\partial \boldsymbol{\omega}}{\partial t} + \mathbf{u} \cdot \nabla \boldsymbol{\omega} = \boldsymbol{\omega} \cdot \nabla \mathbf{u} + \frac{1}{\rho^2} \nabla \rho \times \nabla p + \text{viscous terms} \ . \tag{4}$$

The second term in the right-hand-side, which accounts for the baroclinic vorticity generation, vanishes when $\rho = \rho(p)$. As a results, an important vorticity source is lost, especially in the cavity closure region [21].

Practical computations of industrial flows are using RANS equations with various turbulence modelling capabilities. This approach is embedded in most commercial codes currently available, e.g. FLUENT [17]. As a result, it seems natural to build a cavitating flow model on top of such computational infrastructure.

An alternative to the equation of state is to derive a transport equation for the vapour volume fraction. The continuity Eq. (3), together with Eq. (1), give the velocity divergence as

$$\nabla \cdot \mathrm{u}_m = -\frac{1}{\rho_m}\frac{d\rho_m}{dt} = \frac{\rho_l - \rho_v}{\rho_m}\frac{d\alpha}{dt} \ . \tag{5}$$

Using Eq. (5), the conservative form of the transport equation for *α* can be easily written,

$$\frac{\partial \alpha}{\partial t} + \nabla \cdot (\alpha\, \mathrm{u}_m) = \frac{1}{\rho_v}\left[\frac{\rho_v\, \rho_l}{\rho_m}\frac{d\alpha}{dt}\right] \ . \tag{6}$$

Eq. (6), can be also written for the liquid volume fraction, $1-\alpha$,

$$\frac{\partial (1-\alpha)}{\partial t} + \nabla \cdot \left[(1-\alpha)\,\mathrm{u}_m\right] = \frac{1}{\rho_l}\left[-\frac{\rho_v\, \rho_l}{\rho_m}\frac{d\alpha}{dt}\right] \ . \tag{7}$$

The factor in square brackets in the r.h.s. of Eqs. (6) and (7) is the interphase mass flow rate per unit volume:

$$\dot{m} = \frac{\rho_v\, \rho_l}{\rho_m}\frac{d\alpha}{dt} \ . \tag{8}$$

If we add term by term Eqs. (6) and (7), we end up with an inhomogeneous continuity equation of the form

$$\nabla \cdot \mathrm{u}_m = \dot{m}\left(\frac{1}{\rho_v} - \frac{1}{\rho_l}\right) , \tag{9}$$

which is used in [11] to replace homogeneous Eq (3).

Finally, the vapour volume fraction transport equation is written as:

$$\frac{\partial \alpha}{\partial t} + \nabla \cdot (\alpha\, \mathrm{u}_m) = \frac{1}{\rho_v}\dot{m} \ . \tag{10}$$

This is the equation for the additional variable α, to be solved together with the continuity and momentum equations.

Most of the efforts in cavitation modeling are focused on correctly evaluating. One approach has been proposed by Merkle et al. [15], by modeling the phase transition process similar to the chemically reacting flows. This model was successfully employed by Kunz et al. [16] in a variety of cavitating flows. However, the model constants are chosen somehow arbitrary, and this choice ranges several orders of magnitude from one problem to another. Senocak and Shyy attempt a derivation of an empiricism-free cavitation model [21] to avoid the evaporation/condensation parameters introduced by Merkle.

A different approach is proposed by Schnerr and Sauer [25], who consider the vapour-liquid mixture as containing a significant number of spherical bubbles. As a result, the vapor volume fraction can be written as

$$\alpha = \frac{n_b \frac{4}{3}\pi R^3}{1 + n_b \frac{4}{3}\pi R^3} , \tag{11}$$

where the number of bubbles per volume of liquid, n_b, is a parameter of the model.

From (11) we can easily get

$$\frac{d\alpha}{dt} = \alpha(1-\alpha)\frac{3\dot{R}}{R} , \tag{12}$$

where $\dot{R}$ is the bubble vapour-liquid interface velocity. A simplified Rayleigh equation can be used to compute

$$\dot{R} \equiv \frac{dR}{dt} = \mathrm{sgn}(p_v - p)\sqrt{\frac{2}{3}\frac{|p_v - p|}{\rho_l}} . \tag{13}$$

Of course, the bubble grows if the mixture pressure is less than the vaporization pressure, $p < p_v$, and collapses when $p > p_v$. The bubble collapse, as modeled by the Rayleigh second order differential equation, is much more rapid than the bubble growth. However, the above model seems to make no such difference between growing and collapse.

The present paper employs the mixture model, as implemented in the FLUENT commercial code, with the cavitation model described by Eqs. (8), (12) and (13).

Physically, the cavitation process is governed by thermodynamics and kinetics of the phase change process. The liquid-vapor conversion associated with the cavitation process is modeled through two terms, which represents, respectively, condensation and evaporation. The particular form of these phase transformation rates constitutes the basis of the cavitation model.

The numerical approach

To simulate the cavitating flow the numerical code FLUENT [17] was used. The code uses a control-volume-based technique to convert the governing equations in algebraic equations that can be solved numerically. This control volume technique consists of integrating the governing equations at each control volume, yielding discrete equations that conserve each quantity on a control-volume basis. The governing integral equations for the conservation of mass and momentum, and (when appropriate) for energy and other scalars, such as turbulence and chemical species, are solved sequentially. Being the governing equations non-linear (and coupled), several iterations of the solution loop must be performed before a converged solution is obtained. The flow solution procedure is the SIMPLE routine [17]. This solution method is designed for incompressible flows, thus being implicit. The full Navier-Stokes equations are solved. The flow was assumed to be steady, and isothermal. In these calculations, turbulence effects were considered using turbulence models, as the k-ε RNG models, with the modification of the turbulent viscosity for multiphase flow. To model the flow close to the wall, the standard wall function approach was used, then the enhanced wall functions approach has been used to model the near-wall region (i.e., laminar sublayer, the buffer region, and fully-turbulent outer region). For this model, the used numerical scheme of the flow equations was the segregated implicit solver. For the model discretization, the SIMPLE scheme was employed for pressure-velocity coupling, second-order upwind for the momentum equations, and first-order upwind for other transport equations (e.g. vapor transport and turbulence modeling equations). The computational domain is discretized using the GAMBIT preprocessor [17]. The flow close to the body surface is of particular importance in the current study, the mesh structure in the computational domain deliberately reflects this concern by heavily clustering the mesh close to the solid surface of the body so that the boundary layer mesh is used the body surface.

Validation of the cavitating flow model

Before any attempt of computing cavitating hydrofoil flows, we have tested the model described in Section 2 on a benchmark problem. In a previous paper [19] we have computed the cavitating flow over a hemispherical body, with a good agreement which data a Rouse & McNown [18]. In this paper, we analyze the more difficult case of a blunt cavitator. The flow with and without cavitation computed for the axisymmetric cavitator with blunt fore-body and numerical results are compared with experimental data. For this particular axisymmetric body, Rouse and McNown [18] have provided the pressure coefficient distribution along the body.

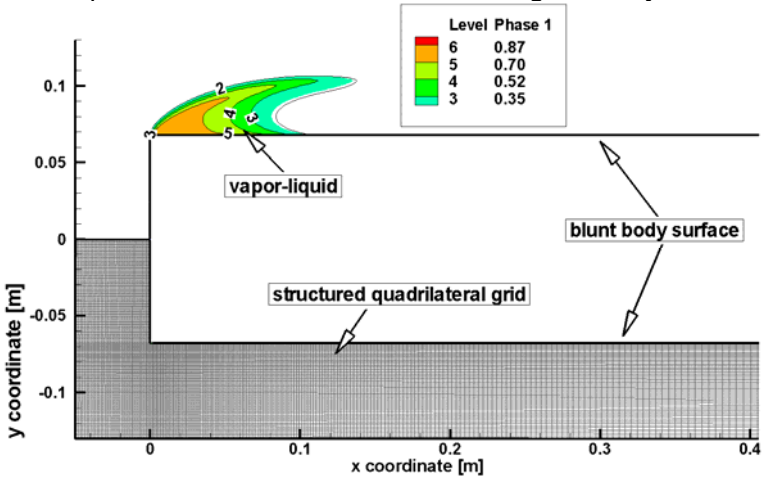

Figure 2.1. Predicted liquid volume fraction and surface pressure contours, selected streamlines and computational grid for a blunt-body, at cavitation number σ = 0.4 (Bernad, [44]).

In Figure 2.1, field liquid volume fraction contours and the computational grid are illustrated for the σ = 0.4 case. The results include steady-state computations of non-cavitating and cavitating flows. From the physical point of view, the steady-state assumption is sensible for sheet cavitation, which has a quasi-steady behavior, with most of the unsteadiness localized in the rear closure region [22].

The inlet boundary condition is specified velocity, using a constant velocity profile. Upper and lower boundaries are slip walls, i.e., a symmetry condition. The outlet used is a constant pressure boundary condition. The cavitator itself is a no-slip wall. The inlet velocity is set to 1 m/s. This is in the same range as the experimental data.

Figure 1 shows the distribution of α around a hemispherical forebody, for a cavitation number

$$\sigma = \frac{p_\infty - p_v}{\frac{1}{2}\rho_l U_\infty^2} = 0.3 \tag{14}$$

Most of the computational domain constrains only liquid, $\alpha = 0$, but within the region with $p < p_v$ the vapour phase is formed with $0 < \alpha < 1$.

Cavitation occurs as a result of the flow acceleration over the body surface resulting in regions with pressures lower than the vapor pressure. Then the water transforms to vapor in these areas, thereby forming vapor-filled cavities. These cavities collapse when the local pressure becomes larger than vapor pressure, with a reentrant water jet and the flow becomes unsteady. Thus an irregular cyclic process of bubble formation and growth occurs, followed by the filling and finally breaking off of the bubble. Due to cavitation, large density and viscosity gradients arise at the interfaces between nearly incompressible fluids.

Within the cavity, there are regions practically filled with gas (the first half), and areas with a gas-liquid mixture corresponding to the re-entrant jet dispersion and vaporization, Figure 2.2.

The present simulation considers a steady flow, corresponding to a stable attached cavitation. However, when the re-entrant jet crosses the cavity boundary a large part of the cavity detaches and is transported downstream, while the remaining part starts growing again.

Visualizations of the velocity field show the development of a re-entrant jet along the hydrofoil, which is in agreement with the classical theory explaining the periodic shedding of vapor structures downstream from a cavity [9], [16], [23]. The qualitative analysis of the re-entrant jet formation is shown in Figure 2.3.

The cavity closure is the region where the external flow re-attaches to the wall. The flow which originally moves along the cavity has locally the structure of a jet impinging obliquely upon the wall. The falling stream divides into two parts flowing parallel to the wall. One is the re-entrant jet which moves upstream towards the cavity detachment. The other one makes the flow re-attach to the wall.

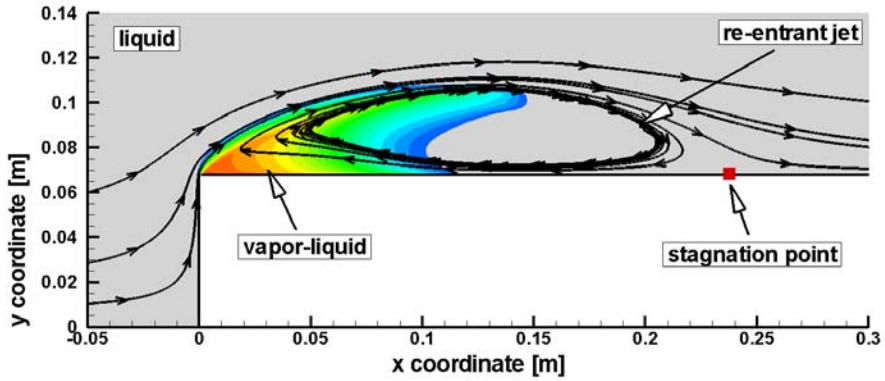

Figure 2.2. Vapour volume fraction ad selected streamlines for cavitating flow around a blunt fore-body for $\sigma = 0.4$, (Bernad, [44]).

The complexity of the problem regarding the region downstream of the cavity is such that all numerical models must introduce some simplifications. The cavity closure region is, in fact, a two-phase, turbulent zone where vaporization and condensation generate unsteadiness and instabilities. However, for certain flow configurations, the cavity end-zone is only moderately perturbed, thus allowing for a steady solution.

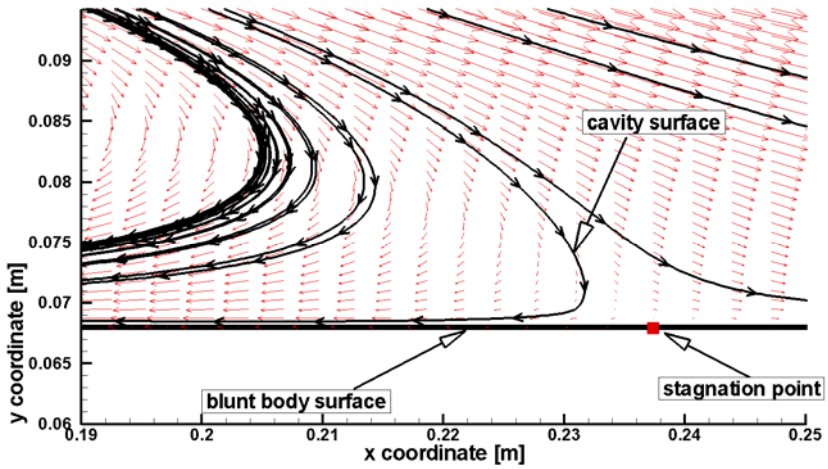

Figure 2.3. Velocity vector field on the cavity end-zone showing the re-entrant jet formation under cavitating condition for blunt fore-body at $\sigma = 0.3$ (Bernad, [44].

It was widely assumed that the character of the cavity termination model only affected the local behavior of the flow for sufficiently long cavities. However, as observed by Li [2], the cavity shape and length can depend critically upon the termination model and the cavity detachment point.

The pressure coefficient is plotted against the dimensionless curvilinear abscissa along the body, originating at the axis,

$$c_p = \frac{p - p_\infty}{\frac{1}{2}\rho_l U_\infty^2} \tag{15}$$

Figure 2.4 shows predicted and measured surface pressure distributions at several cavitation numbers for a blunt fore-body with cylindrical afterbody. The model is seen to accurately capture the bubble size as manifested by the decrease in magnitude and axial lengthening of the suction peak with decreasing cavitation number. Also captured is the overshoot in pressure recovery associated with the local stagnation due to bubble closure.

The numerical results correspond to the dashed line and agree very well with the experimental data [18]. In the cavitation model, the vaporization pressure is adjusted to obtain the cavitation number or $\sigma = 0.3$ or $\sigma = 0.5$. As a result, the negative values of pressure coefficient are limited within the cavity at $-\sigma$. However, at cavitation inception (upstream and of the cavity) the pressure coefficient still drops below $-\sigma$ as the bubbles are transported faster than they can grow. At the end of the cavity, there is a sharp increase in c_p, corresponding to the exact location of the downstream stagnation point from Figure 2.3.

A number of $n_b = 10^7$ bubbles per unit of liquid volume, Eq. (11) have been used in this simulation. Our numerical experiments have shown that the value does not modify the results of steady flows even if is reduced by an order of magnitude. However, for unsteady flow simulation, this is not true.

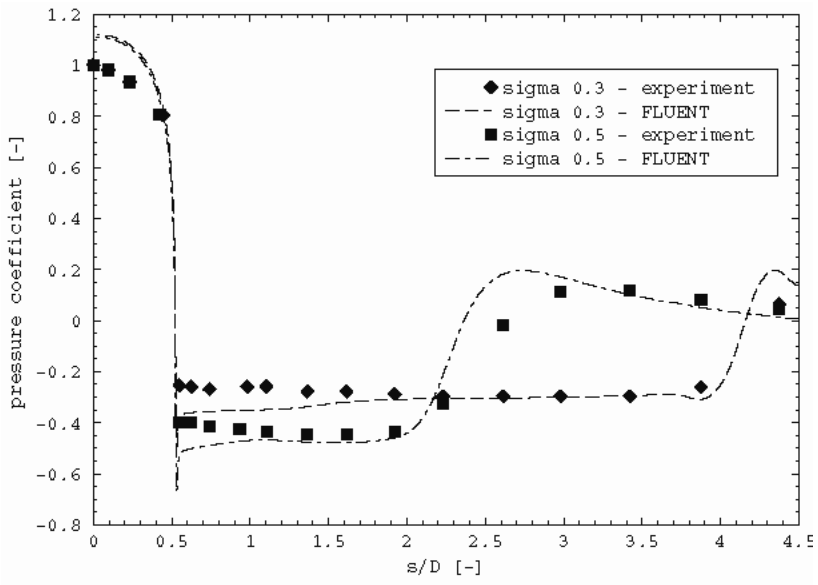

Figure 2.4. Comparison of predicted and measured surface pressure distributions at several cavitation numbers for a blunt-body (experimental data of Rouse and McNown [18]) (Bernad, [44]).

Cavitating flow of a NACA 0009 hydrofoil

In this section, we examine the fully wetted flow and the partially cavitating flow for two-dimensional hydrofoils. The main reason for focusing on two-dimensional flow is that particular attention will be given to the method of simulating the movement at the end of the cavity which is a highly turbulent zone characterized by two-phase flow, unsteadiness, and instabilities. Thus the rationale is to formulate an accurate model to simulate the two-dimensional flow before extending to three dimensions. Most cavity closure models have been formulated to comply with the theoretical analysis of the cavitating flow problem while at the same time attempting to model the physical reality.

The first case we shall present is that of an NACA 0009 hydrofoil at 2.50 angle of attack and a cavitation number equal to 0.81, investigated experimentally in [20]. The computational domain is consistent with the experimental setup presented by Dupont [20]. A structured quadrilateral mesh is used for computational domain discretization. Most of the cells are located around the foil, and a contraction of the grid is applied in its upstream part, to obtain a particularly fine discretization of the areas where cavitation is expected, Figure 2.6a.

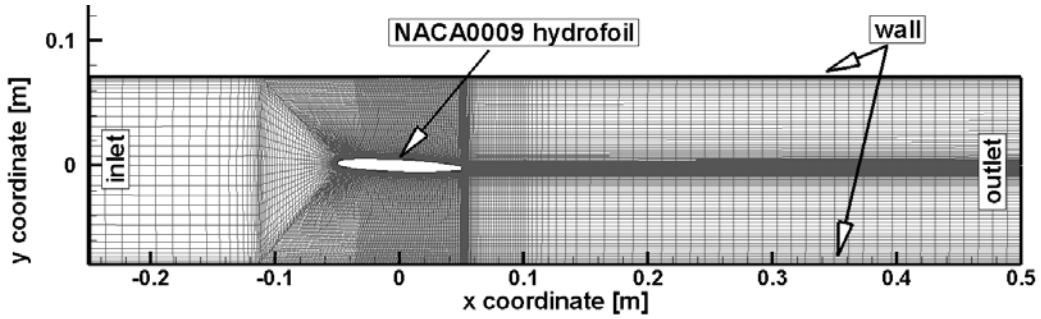

Figure 2.5. Computational domain and boundary conditions for NACA 0009 hydrofoil. (Bernad, [44])

Standard boundary conditions for incompressible flow are applied: the velocity is imposed at the inlet (V_{ref} = 20 m/s in the present case) and the pressure is fixed at the domain outlet. Then, the pressure is lowered slowly at each new time-step, down to the value corresponding to the desired cavitation number σ defined as $(P_{downstream}-P_{vap})/(\rho_{ref}V_{ref}^{2}/2)$. Vapor appears during the pressure decrease. The cavitation number is then kept constant throughout the computation.

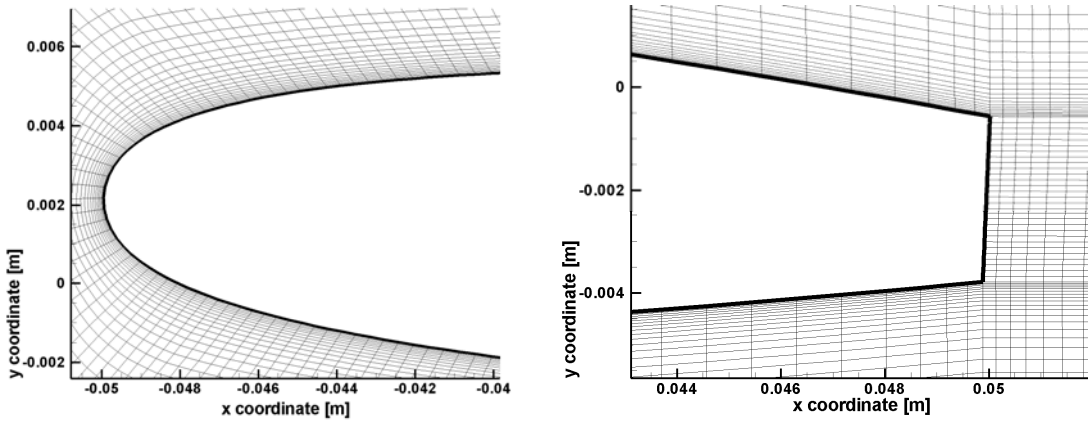

Figure 2.6. Grid system surrounding the NACA 0009 hydrofoil at 2,5 degree angle of attack; a) A close-up near the leading edge, b) A close-up near the trailing edge, (Bernad, [44]).

The presence of a boundary layer will modify the main flow streamlines and subsequently the pressure distribution along the guiding surface. It is important however to distinguish between a cavitation pocket which forms when the liquid detaches itself from the guiding surface, leaving a liquid-free zone, and a separation pocket which forms when the boundary layer separates, leaving a liquid-filled zone. In nearly all cases, the initial point of separation will occur downstream from the point of minimum pressure as the flow up to this point is accelerating. However, cavitation is caused due to the reaching of a particular absolute pressure at any point in the flow. In general, this absolute pressure will be reached at or very close to the guiding surface. Thus at inception, cavitation will occur close to the point of minimum pressure on the surface.

Experiments have revealed that the location of the cavity detachment point can have a significant effect on the cavity extent and the cavity volume. In the case of a sharp leading edge, the cavity will develop from this point. If however, the leading edge is a smooth curve, the cavity detaches from a point downstream of the laminar boundary layer separation point (Figure 2.7). The position of the separation and the detachment point and the correlation between them have been studied extensively in the literature.

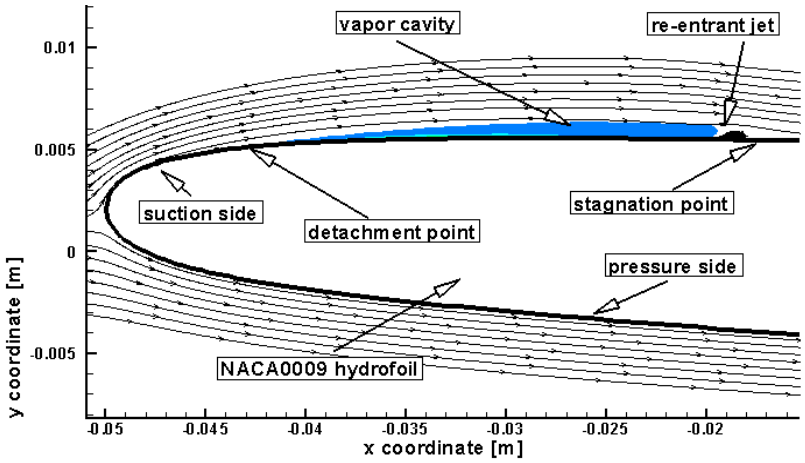

Figure 2.7. Computed total volume franctions distributions and selected streamlines for NACA 0009 hydrofoil at cavitation number = 0.81., (Bernad, [44])

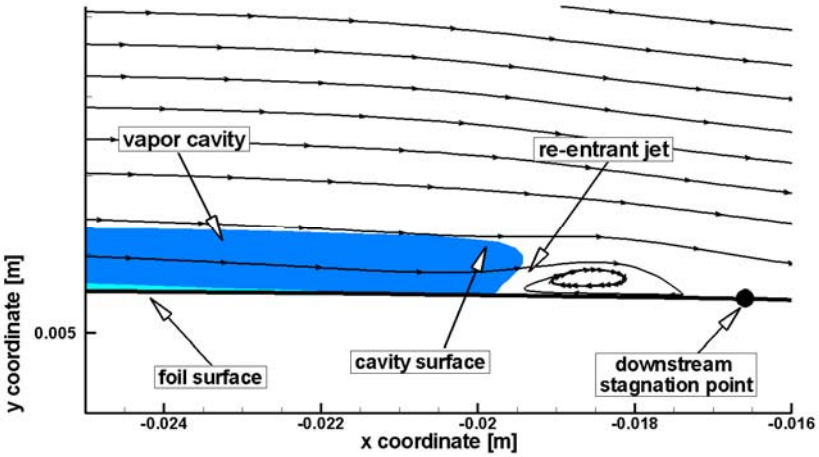

Figure 2.8. Velocity vector field on the cavity and zone showing the re-entrant jet formation under cavitating condition for an NACA 0009 hydrofoil at cavitation number = 0.81., (Bernad, [44])

Visualizations of the velocity field show the development of a re-entrant jet along the hydrofoil, which is in agreement with the classical theory explaining the periodic shedding of vapor structures downstream from a cavity (Kubota et al., 1992; Kunz et al., 1999; Krishnaswamy, 2000). The qualitative analysis of the re-entrant jet formation is shown in Figure 2.8.

The cavity closure is the region where the external flow re-attaches to the wall. The flow which originally moves along the cavity has locally the structure of a jet pinging obliquely upon the wall. The falling stream divides into two parts flowing parallel to the wall. One is the re-entrant jet which moves upstream towards the cavity detachment. The other one makes the flow reattach to the wall.

The gas void fraction contours at the specific cavitation numbers are shown in Figure 2.7. The simulation results indicate the cavity generated on this foil under cavitation number of 0.81 is of stable sheet cavity type. Typical instantaneous pressure contour plots of a cavitating hydrofoil NACA 0009 at non-cavitating and cavitating condition (cavitation number 0.81), are presented in Figures 2.9 and 2.10. A region of nearly constant pressure indicating sheet cavity is clearly observable from these figures.

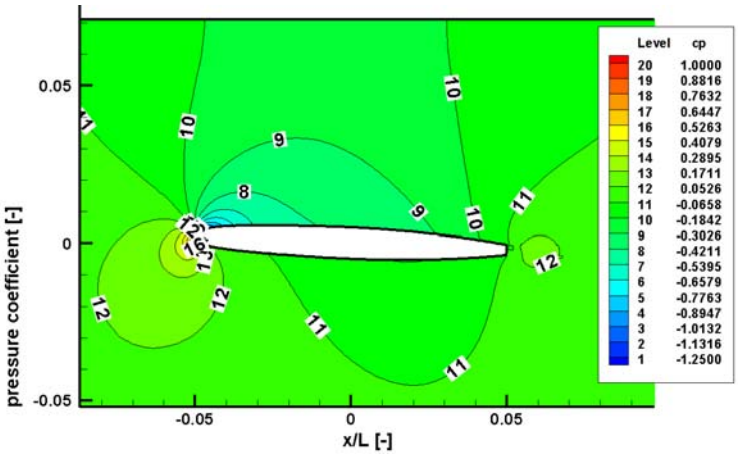

Figure 2.9. Pressure coefficient distribution on the NACA 0009 hydrofoil at 2,5 degree angle of attack. No cavitation, (Bernad, [44]).

The pressure contours for the flow field at a cavitation number of 0.81 are plotted in Figure 2.9. We observe that the pressure contours cluster around the cavitation boundary where the density gradient is very large and the flow turns around the cavity.

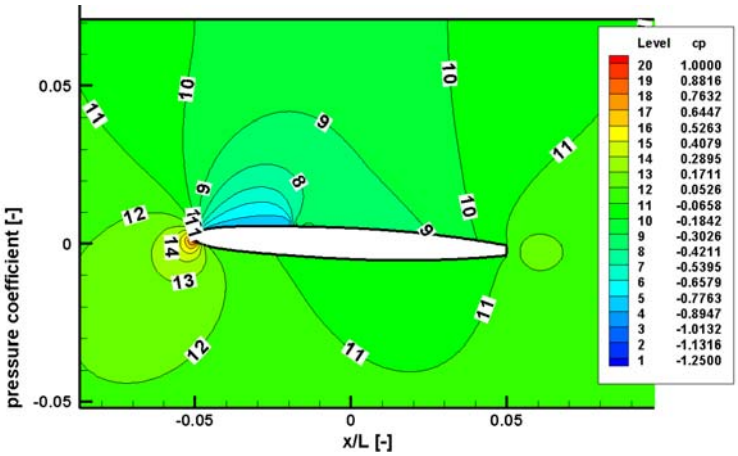

Figure 2.10. Pressure coefficient distribution on the NACA 0009 hydrofoil at 2,5 degree angle of attack and cavitation number 0.81, (Bernad, [44]).

For the cavitation number of 0.81, the cavity extends up to 30 percent of chord. As the cavitation number increases the gas bubble region decreases in length and comes closer to the surface.

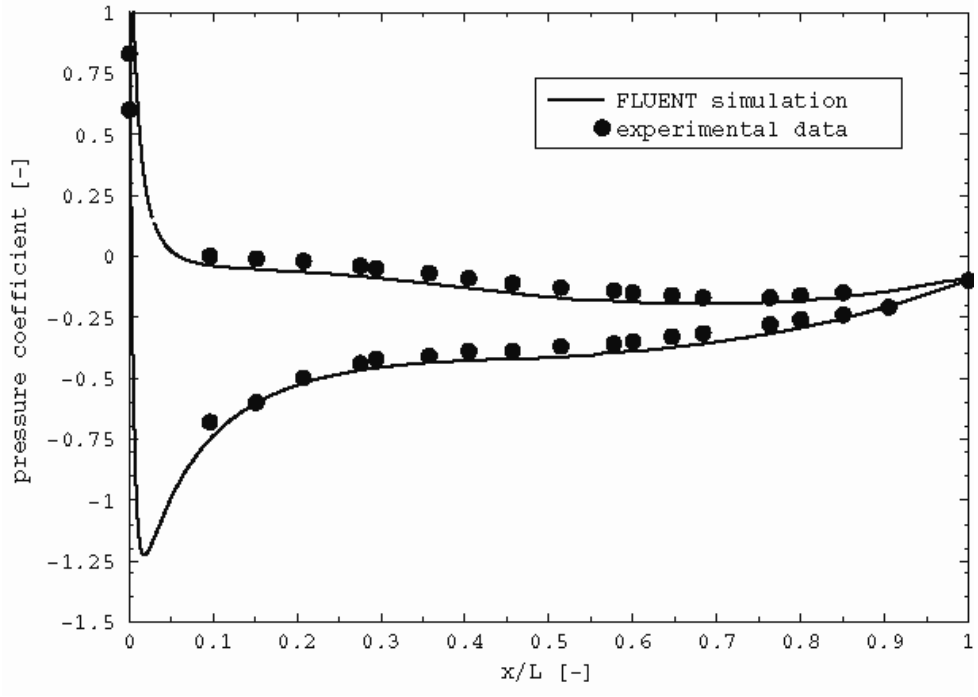

(a)

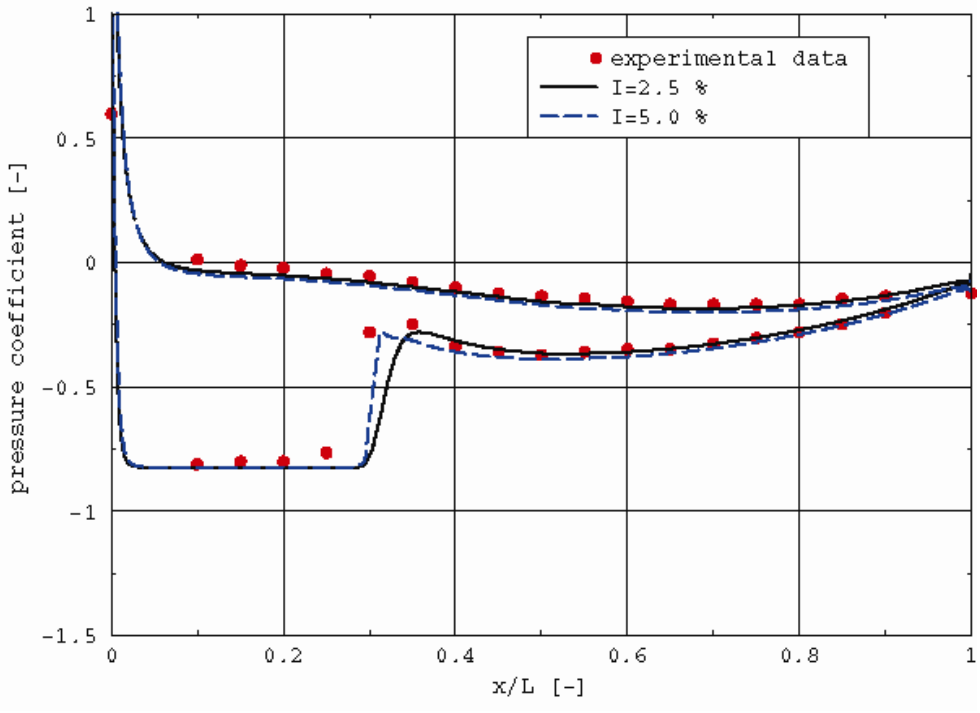

(b)

Figure 2.11. Pressure coefficient distribution of the different turbulence intensity for NACA 0009 hydrofoil at no-cavitating condition (a) and (b) cavitation number =0.81 (experimental data of Dupont [20]), (Bernad, [44]).

Figure 2.11b shows the comparison of numerical results with experimental data for both non-cavitating and cavitating flows over an isolated NACA 0009 hydrofoil at 2,50 angle of attack. An excellent agreement is obtained between simulation and experiment. Moreover, for cavitating flow, we have investigated the effect of turbulence intensity on pressure distribution near the cavity closure. One can see that higher turbulence intensity tends to a sharper cavity closure (dashed line).

Although the incoming turbulence intensity is one order of magnitude smaller in the cavitation tunnel, the turbulence intensity levels considered in the present investigation try to account for the flow induced hydrofoil vibrations.

CONCLUSIONS

The paper presents a numerical investigation of cavitating flows using the mixture model implemented in the FLUENT commercial code [17]. The inter-phase mass flow rate is modeled with a simplified Rayleigh equation applied to bubbles uniformly distributed in computing cells, resulting in an expression for the interphase mass transfer. This is the source term for the vapor phase transport equation. As a result, the density of the liquid-vapor mixture is allowed to vary from the vapor density up to the liquid density.

The cavitation model is validated for the flow around a blunt fore-body cavitator. The numerical results agree very well both qualitatively and quantitatively with the experiments. As a result, we include that the present cavitational model can capture the major dynamics of attached cavitating flows.

As the authors proceed with this research, we are focusing on several areas including:

1) improved physical models for mass transfer and turbulence,
2) extended application and validation for steady two-dimensional flows.

CAVITATION PHENOMENA IN HYDRAULIC VALVES

Cavitation is not nearly as well documented in hydraulic power systems as it is in such water hydraulic systems as pumps, propellers, hydraulic turbines, and hydrofoils. In hydraulic power systems, cavitation most frequently occurs in system valves, pumps, and actuators. Significant differences in pressure is a frequent cause of small-scale cavitation in chambers of four-way spool valves, while the high-frequency motion of a valve-controlled actuator can lead to large-scale cavitation in the cylinder. Another source of cavitation in hydraulic power systems is the improper filling of the pistons on an axial-piston pump. Either during transient loading or under steady-state operation, cavitation can occur in the return chamber of directional control valves because of the significant pressure drop across the orifice. It is of interest to know the potential cavitation damage, as well as any effect of cavitation on system performance under both steady and unsteady flow conditions. Criteria should be established for the onset of cavitation, and damage mechanisms need be identified once cavitation is extensive.

In many engineering applications, cavitation has been the subject of extensive theoretical and experimental research since it has predominantly been perceived as an undesirable phenomenon. This is mainly due to the detrimental effects of cavitation such as erosion, noise, and vibrations, caused by the growth and collapse of vapor bubbles.

The flow inside the poppet valve is a complex process which is strongly dependent on the details of the valve geometry, the fluid properties, and the operating conditions. Separation and

reattachment of jets can have a profound effect on the flow pressure and force characteristics as well as influence the susceptibility to cavitations.

Hydraulic valves differ from process control valves in application and design. Hydraulic valves are typically used for controlling pressures and therefore, are of the quick opening type of characteristics. Quick opening valves utilize plugs shaped in the form of a truncated cone with relatively large clearances between the plug and the seat. Alternatively, sometimes these valves use a disc for a poppet plug. Process control valves, on the other hand, are used for precise control of the fluid flow rate and are the linear or equal percentage characteristic. These type valves usually have small clearances between the plug and the seat. Despite these differences, many of the flow phenomena in the hydraulic valve such as recirculation and jet separation and reattachment also occur in the process control valve.

A poppet valve seating-type valve in which the moving element or poppet, usually spherical or conical shape, moves in a direction perpendicular to its seat. Because of the several advantages that are associated with poppet valves such as ease of manufacture, minimum leakage, and insensibility to clogging by dirt particles, poppet's have been used for as pressure regulators and relief valves. The operation of this type of valve is quite simple. The fluid pressure counterbalances the spring force and allows fluid escape through the annular passage way between the poppet and the seat.

Separating interior flows are of the utmost importance for the performance of a wide variety of technical applications [26 - 30]. Many industrial designs today have to be compromises between the hydrodynamical function and other competing functions e.g. size or mechanical function. In such compromised designs undesired separation is more likely to occur, this drastically decreases the performance of conception. In such cases, active or passive devices which increase there near wall momentum can be used to remove or reduce the separation [27], [28], [31].

The presence of flow separation in the valve passage and the occurrence of different flow patterns has previously been identified in some investigations of various valve geometries. In the extensive work carried out by Tanaka in 1929 [32], it was observed that discontinuities in the flow occurred when investigating the flow quantity across the valve for different valve lifts.

The experimental work of hydraulic valves extends back over many years. Johnston and Edge [33] studied forces on the valve plug as well as the pressure-flow characteristics for several different plug and seat arrangements. Schrenk [34] published work on the pressure-flow characteristics of poppet and disk valves. Stone [35] studied the characteristics of poppet valves with sharp-edged seats, small openings, and low Reynolds number. McCloy and McGuigan [36] studied the effects of the downstream chamber size in a two-dimensional model of a poppet. Some researchers have attempted to analytically predict flow through poppet valves. Von Mises [30] predicted the contraction coefficient for flow through an orifice using potential flow. Fluid forces on the plug are often estimated using simple concepts of fluid momentum change through the valve [28], [35]. Recently CFD has been combined with experimental work to analyze hydraulic valves. Vaughan, Johnston, and Edge [37] modeled the valve reported experimentally by Johnston and Edge [33].

Weclas et al. [38] presented a comprehensive investigation into flow separation in the inlet valve passage using measurement techniques such as discharge coefficient measurements, surface flow visualization using an oil streak technique and detailed flow measurements using LDA. The detailed flow measurements at the valve exit plane and the surface flow visualization showed the flow separation in the valve passage and identified its distribution around the valve periphery for generic inlet port geometries.

A successful design of poppet valves requires a thorough analysis of both velocity and pressure fields, with the aim of improving the poppet/seat geometry. Technological considerations lead to sharp corners, which in conjunction with very narrow passages produce regions of extremely high gradients in the flow field. As pointed in [39 - 41], the poppet flow is not easily suited to classical mathematical analysis.

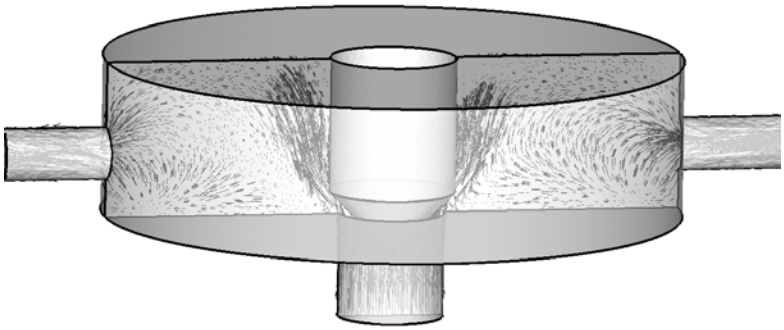

Figure 2.11. Velocity vector field and streamlines in meridional section plane, (Bernad, [45]).

The relative simple geometry, Figure 2.11, produces a very complicated viscous flow field (Figure 2.12), which can be realistically investigated only by using Computational Fluid Mechanics. Powerful numerical tools, such as FLUENT software [17], are now available for investigating flows through arbitrary geometries.

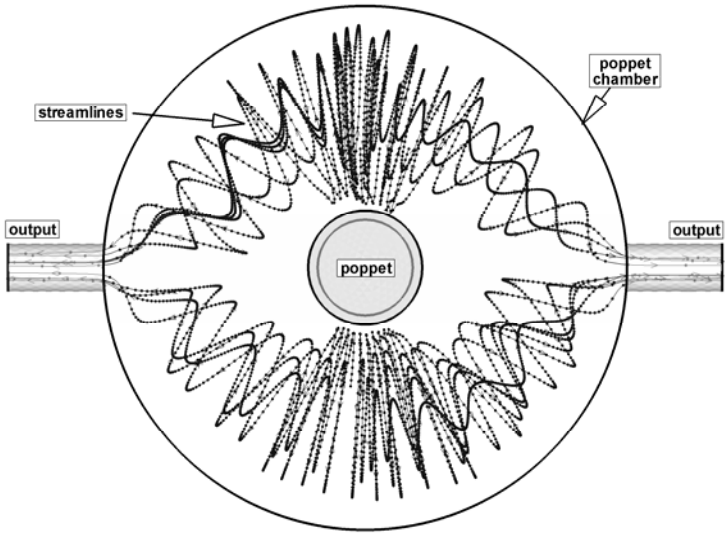

Figure 2.12. Flow field representation using selected streamlines inside the poppet valve, (Bernad, [45]).

Figure 2.11 show velocity vector field in meridional section plane overlaid with selected streamlines in the 3D computational domain. Velocity vector field in section plane shows the large recirculation region confirming the adamant nature of the helical vortex flow in this poppet valve geometry (Figure 2.12). The vortex evolution is clearly influenced by the position of the valve outlet section position. Time markers are shown on each streamline, with a unit time step. This representation offers a quick quantitative assessment of the velocity magnitude variation along the streamlines. For example, for the streamline originating near the inlet center, the velocity increases in the valve passage, remains accelerated in the helical vortex region and decreases in the outlet section.

As shown in our previous work [42], the cavitation region is relatively large in a poppet valve chamber. Thus we expect a significant change of the flowfield compared with the single phase flow. In the previous section presents a simple cavitating flow model employed by the commercial code FLUENT, and results obtained by using this model are shown in the next section. The main question addressed in this paper is whether or not the single phase flow simulation correctly predicts the vapor cavity radius and location. Also, we also examine the differences between single-phase and two-phase models regarding the flow rate and streamline pattern.

Single phase flow simulation and analysis

A typical streamline pattern for the liquid flow through the poppet valve is presented in Figure 2.14. Three main vortices are developed in the poppet valve chamber. The first two vortices, V1 and V2, are rotating counterclockwise and clockwise, respectively, and are generated on the left-hand side and right-hand side, respectively, of the liquid jet issued from the poppet-seat opening. The third vortex, V3, is produced beyond the valve chamber, in the outflow channel. Such a qualitative analysis of the flow field has also been performed by Dietze [40], who used flow visualization to validate the numerical results, i.e. the streamline pattern. However, Dietze does not provide a quantitative description of the velocity and pressure fields details.

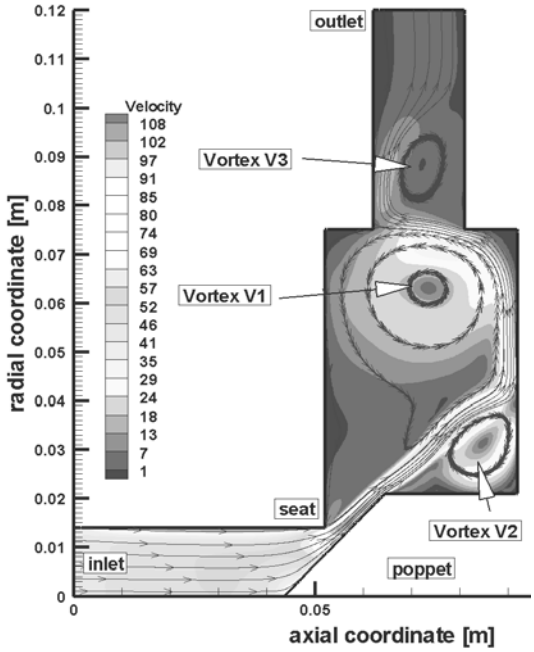

Figure 2.13. Streamline pattern and pressure field in the meridian half-plane of the poppet valve, (Bernad, [45]).

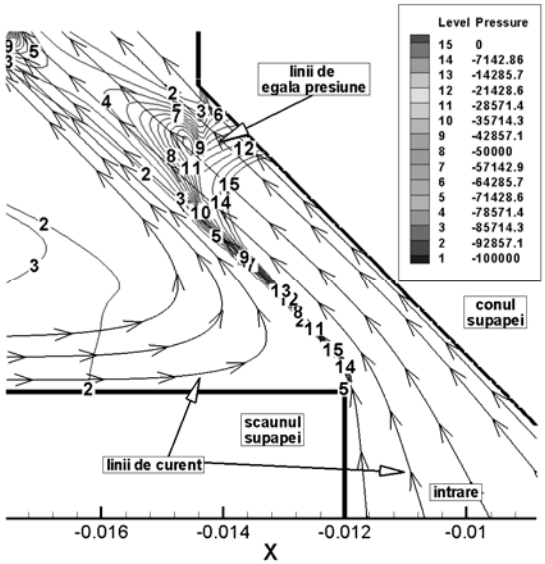

Figure 2.14. Streamline pattern and pressure field in throttle point vicinity, (Bernad, [45]).

The presence of flow separation in the valve passage and the occurrence of different flow patterns has previously been identified in some investigations of various valve geometries. In a previous work than authors investigated the flow pattern inside the hydraulic poppet valve chamber for a typical 2D computational domain [42]. In this paper, Bernad et al. proposed an original theoretical vortex model thus allowing a parametric study of the poppet valve flow evolution in a whole range of poppet displacement. Bulloungh [26] perform the static pressure measurements along the valve cone and seat wall for different poppet displacement. Visualization of the valve passage flow in a transparent model was investigated for various poppet valve configuration by the Johnston et al. [33]. Dietze [40] in his Ph.D. thesis presented a comprehensive investigation into flow separation in the valve passage using measurement techniques and flow visualization to validate the numerical results, i.e. the streamline pattern.

Cavitating Flow Simulation and Analysis

As mentioned in earlyer, after obtaining a steady single phase (liquid) flow solution, the FLUENT code allows turning on the cavitation model. As a result, vapor formation is enabled where the absolute pressure is smaller than the vaporization pressure. In order to obtain correct results the so-called operating pressure p_{op} must be set to zero (it is set to the atmospheric pressure by default), therefore the gauge pressure p_{gauge} will equals the absolute pressure p_{abs},

$$p_{abs} = p_{op} + p_{gauge}. \tag{10}$$

This is particularly important for obtaining only positive absolute pressure values.

As shown in Figure 2.15, when the cavitating flow model is used the pressure inside the cavity becomes constant and equals the vaporization pressure, in concordance with cavitation physics. On the other hand, Figure 2.14 reveals that the pressure exceeds the vaporization pressure at the same radius of approximately 9 mm for both single-phase and two phase models. However, one cannot say that the cavity radius is 9 mm since a continuous transition from vapor to liquid takes place.

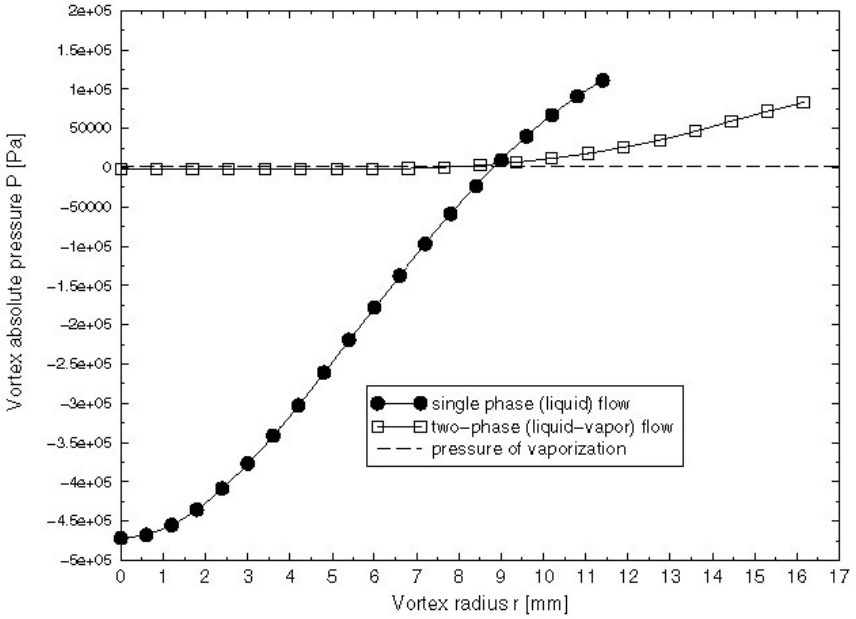

Figure 2.15. Radial pressure distribution inside the main vortex V1, computed for liquid flow (filled circles, see Figure 2.13) and liquid-vapour flow (squares), (Bernad, [39]).

Figure 2.16 shows the liquid-vapor mixture density, starting with the vapor region inside the cavity and ending with pure liquid. One can see that there is a large region containing a mixture of liquid and vapor, as it actually happens for industrial cavitation.

A control valve creates a pressure drop in the fluid as it controls the flow rate. The profile of the fluid pressure, as it flows through the valve, is shown in the following graph. The fluid accelerates as it takes a pressure drop through the valve's trim, It reaches its highest velocity just past the throttle point, at a point called the vena contracta. The fluid is at its lowest pressure and highest velocity at the vena contracta. Past the vena contracta the fluid decelerates and some of the pressure drop is recovered as the pressure increases. The pressure in the vena contracta is not of importance until it is lower than the fluid's vapor pressure. Then the fluid will quickly form vapor bubbles and, if the pressure increases above the vapor pressure, the vapor bubbles instantly collapse back to liquid (Figure 2.16).

The liquid flow rate will increase as the pressure drop increases. However, when cavitation vapor bubbles form in the vena contracta, the vapor bubbles will increasingly restrict the flow of liquid until the flow is fully choked with vapor. This condition is known as "choked flow" or "critical flow". When the flow is fully choked, the flow rate does not increase when the pressure drop is increased.

Cavitation will begin at the point of "Incipient Cavitation" and increase in intensity to the point of choked flow. Cavitation at point of "Incipient Cavitation" is not damaging and is almost undetectable. At some point between incipient and choked, the cavitation may damage most trim styles. The location of the "Damage" point varies with trim style and material.

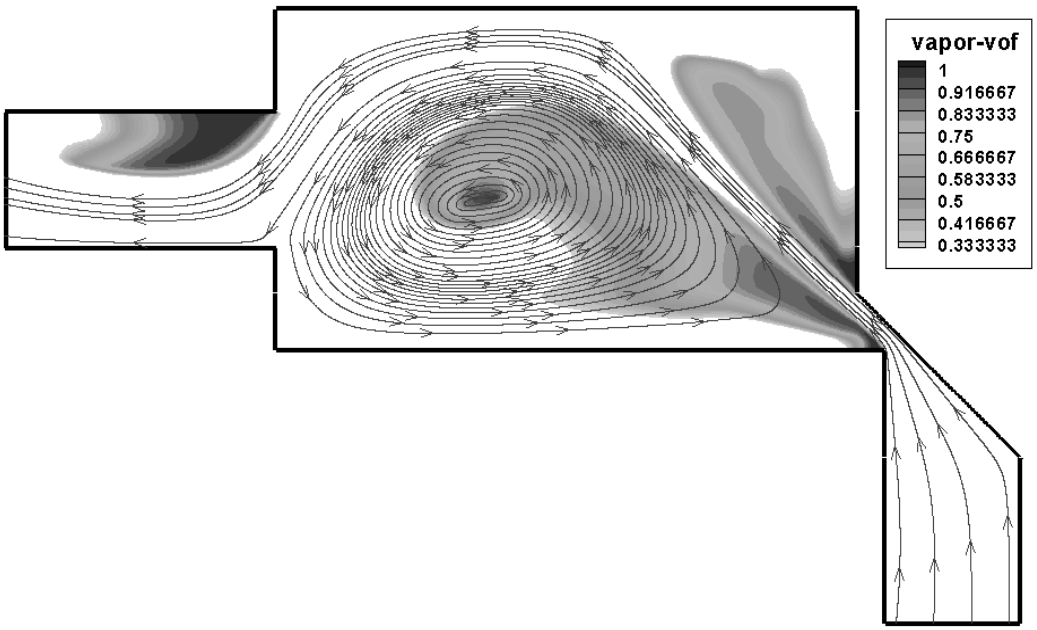

Figure 2.16. Radial distribution for the liquid-vapor mixture density inside the main vortex (cavity), (Bernad, [45]).

The radial distribution of the density inside the main vortex is presented in Figure 2.17. One can say that the vapor filled cavity has a radius of 5 mm, but since we have a smooth transition from the vapor region to the liquid region other conventional cavity radii might be defined.

The cavitating flow streamline pattern is not significantly altered in comparison with the one presented in Figure 2.11. However, one can notice that the main vortex is slightly shifted toward the axis of symmetry and the secondary vortex V2 becomes smaller.

As far as the flow rate is concerned, the liquid flow value is practically the same for cavitating flows. Further investigations are needed to elucidate this issue.

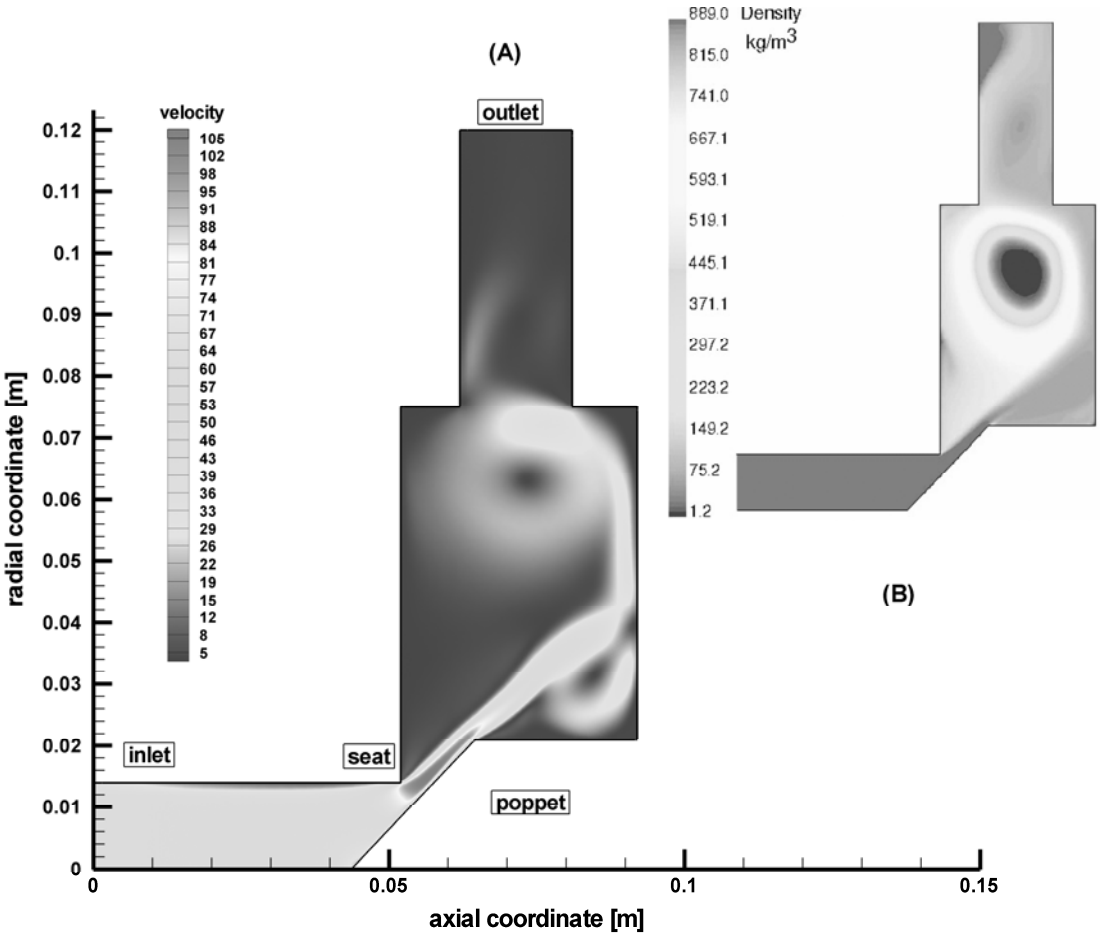

Figure 2.17. Velocity filed and corresponding liquid-vapour mixture distribution for cavitating flow, (Bernad, [45]).

Three-dimensional cavitating flow in Francis turbine runner

The cavitating flow model described and validated in the above sections is further used to investigated a complex three-dimensional flow in the GAMM Francis turbine runner (Avellan *et al*., 1990 [6]; Avellan *et al*., 1993 [7]). The liquid steady turbulent relative flow in a runner interblade channel is first computed using a mixing interface approach (Muntean et al., 2004, [43]). The operating conditions are set to achieve a cavitation number σ = 0.1:

$$\sigma = \frac{p_{atm} - p_v - \rho_l h H_S}{\rho_l E} = 0.1$$

Where: p_{atm} = 17000 *Pa*, p_v = 2300 P*a*, H_s = 0.9 *m*, and E = 60.33 *J* / *kg*. Note that the atmospheric pressure above is practically achieved for the turbine model by adjusting the overall pressure level in the hydraulic test rig. The pressure coefficient is defined for GAMM Francis turbine as:

$$c_p = \frac{p - p_{ref}}{p_l E_{ref}}$$

where, p_{ref} is the pressure measured at the wall in a reference section downstream the runner, corresponding to the draft tube inlet.

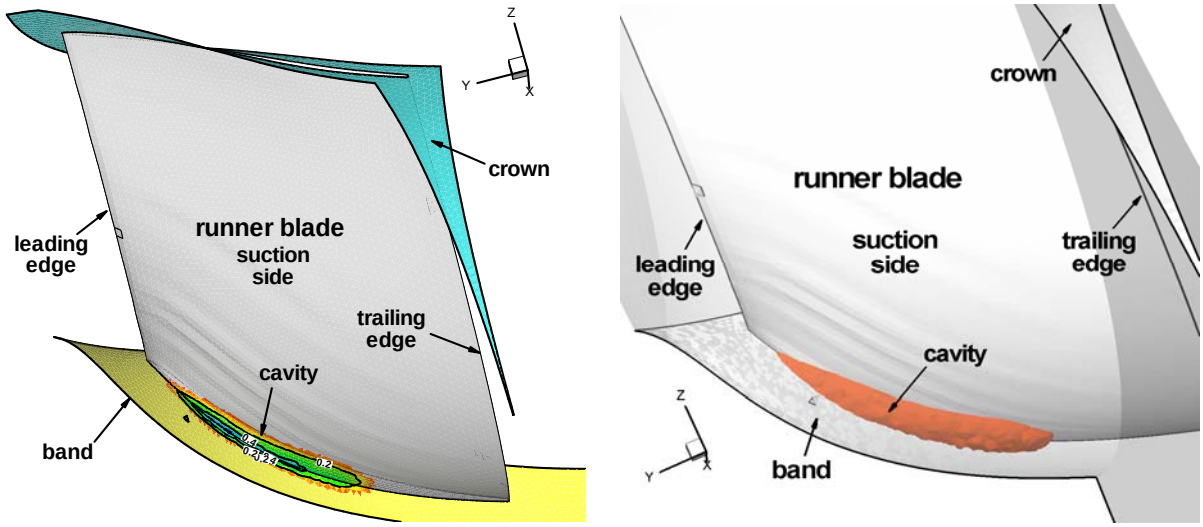

Figure 2.18. a) Vapour volume fraction distribution on the GAMM Francis turbine runner; b) Cavity shape at $\sigma = 0.1$, presented as an iso-surface of $\alpha = 0.5$, (Resiga et al., [19]).

Figure 2.18a shows the region on the runner blade suction side corresponding to "α > 0. It can be seen that cavitation occurs on the runner blade at the junction with the runner band, where pressure drops below the vaporization pressure.

In order to evaluate the 3D shape and extend of the cavity, we are presenting in Figure 2.18b the iso-surface of vapor fraction α = 0.5. Of course, this is only a qualitative assessment of the cavity boundary, as one may choose another iso-surface as the cavity boundary. Nevertheless, the position, shape and size of the cavity to be in good agreement with the cavitating flow visualisation in GAMM Francis turbine runner presented in [6].

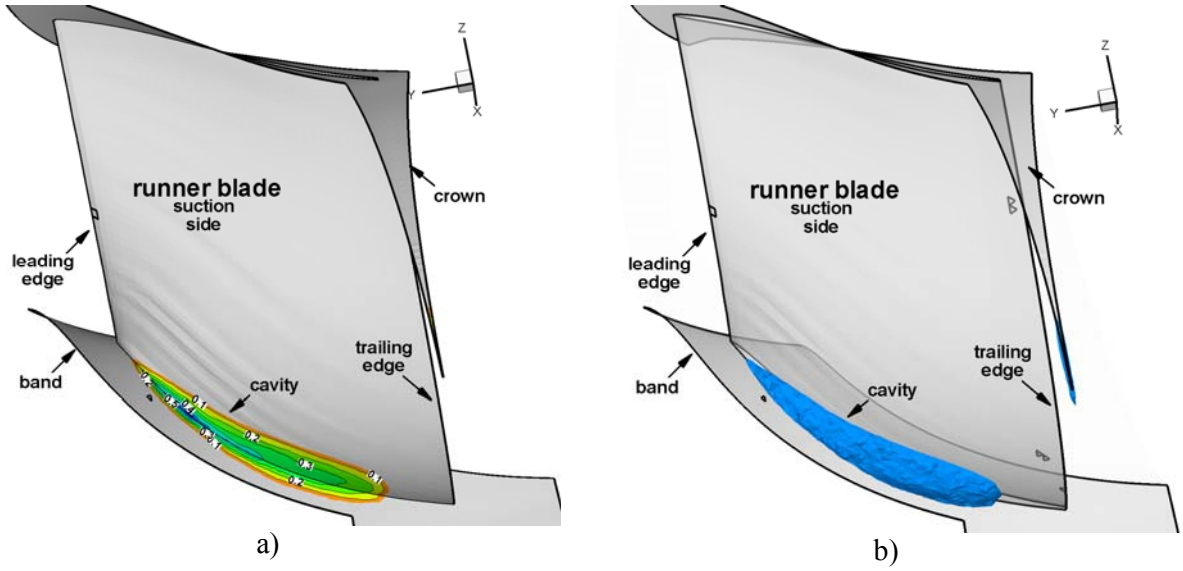

Figure 2.19. a) Vapour volume fraction distribution on the GAMM Francis turbine runner. b) Cavity shape at $\sigma = 0.075$; presented as an iso-surface of $\alpha = 0.5$ (Resiga et al., [19]).

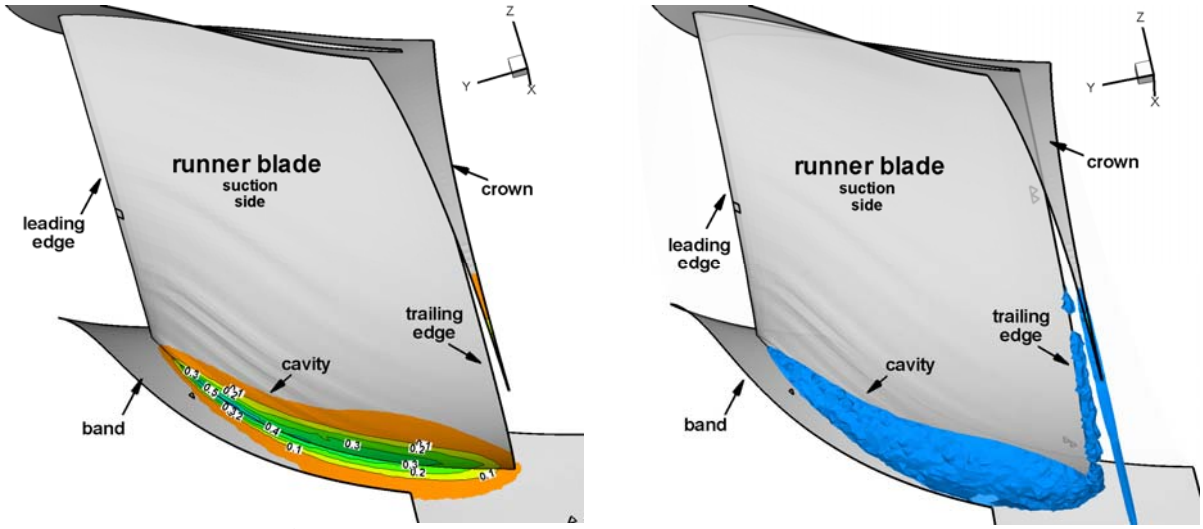

a) b)

Figure 20. a) Vapour volume fraction distribution on the GAMM Francis turbine runner; b) Cavity shape at $\sigma = 0.05$, presented as an iso-surface of $\alpha = 0.5$ (Resiga et al., [19]).

Note that the flow visualisation shows a traveling cloud cavitation, where distinct bubbles can still be observed, Although the mixture model used here does not account for individual bubbles, the fact that α does not exceed 0.6 inside the cavity shows that there are no parts of the cavity completely filled with vapor. For σ = 0.1 the computed runner torque slightly increases from 374.3 N.m (liquid flow) to 375.6 N.m (cavitating flow). This is in good agreement with the turbine efficiency behaviour in the initial stage of the tolerated industrial cavitation regimes. When the cavitation coefficient σ is further decreased, the cavity size (estimated as an iso-surface of vapor volume fraction α = 0.5) increases.

Figure 2.19 shows the cavity at σ = 0.075 and Figure 2.20 at σ = 0.05. The main advantage of directly computing the cavitating flows is that one can evaluate the influence of the cavity on the pressure distribution on the blade and further on the runner torque and turbine efficiency.

(b-i)_2 The research activity and achievements in the thematic direction of:

Flow hydrodynamics in biomedical applications: Cardiovascular flow hydrodynamics

Scientific activity related to the topic of the "Cardiovascular flow hydrodynamics"

❖ **Journal articles** (selection)**:**

1. **Sandor I. Bernad**, Alin F. Totorean, Ladislau Vekas, Particles deposition induced by the magnetic field in the coronary bypass graft model, Journal of Magnetism and Magnetic Materials, 2016, vol 401, pp: 269-286, doi:10.1016/j.jmmm.2015.10.020, **(WOS: 000366585200041, IF=2.357)**.
2. Alin F.Totorean, **Sandor I. Bernad**, Romeo F. Susan-Resiga, Fluid dynamics in helical geometries with applications for by-pass grafts, Applied Mathematics and Computation, 2016, vol 272 part 3, pp: 604-613, http://dx.doi.org/10.1016/j.amc.2015.05.030, **(WOS:000364991600004, IF=1.345)**.
3. Elena S. Bernad, **Sandor I. Bernad**, Izabella Sargan, Marius L. Craina, Saphenous vein graft patency after geometry remodeling, Journal of Mechanics in Medicine and Biology, 2015, vol. 16, no. 2, 1540051, http://dx.doi.org/10.1142/S0219519415400515, **(WOS:000367257400013, IF=0.797)**.
4. **Sandor I. Bernad**, Alin I. Bosioc, Elena S. Bernad, Marius L. Craina, Helical type coronary bypass graft performance: Experimental investigations, Bio-Medical Materials and Engineering, vol. 26, no. s1, pp. 477-486, 2015, http://dx.doi.org/10.3233/BME-151337, **(WOS:000361671800055, IF=0.988)**.
5. Alin F. Totorean, Alin I. Bosioc, **Sandor I. Bernad**, Romeo Susan-Resiga, Critical Flow Regions in the coronary by-pass graft anastomosis, Proceedings of the Romanian academy, Series A, 16(2):201–208, 2015, **(WOS: 000357362300011, IF=1.735)**.
6. Alin F. Totorean, Alin I. BOSIOC, **Sandor I. BERNAD**, Romeo SUSAN-RESIGA, Identification an visualization of the vortices in by-pass graft flow Proceedings of the Romanian academy, Series A, 15(1):52–59, 2014, **(WOS: 000357362300011, IF=1.735)**.
7. E.S. Bernad, **S.I. Bernad**, M.L. Craina, Hemodynamic parameters measurements to assess severity of serial lesions in patient specific right coronary artery, Bio-Medical Materials and Engineering, Volume 24(1), 2014, pp: 323-334, DOI 10.3233/BME-130814, **(WOS: 000327312600039, IF=0.988)**.
8. **S.I. Bernad**, A. Bosioc, E.S. Bernad, M.L. Craina, Comparison between experimentally measured flow patterns for straigth and helical type graft, Bio-Medical Materials and Engineering, Volume 24/1, 2014, pp: 853-860, DOI 10.3233/BME-130877, **(WOS: 000327312600098, IF=0.988)**.
9. **S.I. Bernad**, E.S. Bernad, A.F. Totorean, M.L. Craina, I. Sargan, Clinical important hemodynamic characteristics for serial stenosed coronary artery, International Journal of Design & Nature and Ecodynamics, 2015, 10(2):97-113, 2015, **(SCOPUS)**.
10. **BERNAD Sandor**, BERNAD Elena, CRAINA Marius, Sargan Izabella, TOTOREAN Alin, BRISAN Cosmin, Particle Depositions and Related Hemodynamic Parameters in the Multiple Stenosed Right Coronary Artery, Journal of Clinical Medicine Research, vol 4, no 3, pp: 177-189, doi:10.4021/jocmr843w, 2012, (**SCOPUS)**.
11. **S.I. Bernad**, E.S. Bernad, T. Barbat, V. Albulescu, R. Susan-Resiga, (2010), Effects of different types of input waveforms in patient-specific right coronary atherosclerosis hemodynamics analysis, International Journal of Design and Nature & Ecodynamics, vol 5, no. 2, pp: 142-159, **(SCOPUS)**.

12. **S.I. Bernad**, T. Barbat, E.S. Bernad, R. Susan-Resiga, (2009), Numerical blood flow simulations in narrowed coronary venous bypass graft, Journal of Chinese Clinical Medicine, vol. 4, no. 1, pp: 1- 10, **(SCOPUS)**.
13. **S.I. Bernad**, E.S. Bernad, T. Barbat, R. Susan-Resiga, V. Albulescu, (2009), Effects of asymmetry in patient-specific wall shear stress analyses of abdominal aortic aneurysm, Journal of Chinese Clinical Medicine, vol. 4, no. 8, pp: 421-429, **(SCOPUS)**.

❖ **Articles in international and national conference proceedings** (selection):

1. **S. I. Bernad**, A. Totorean, A. Bosioc, N. Crainic, C. Hudrea, E. S. Bernad, Fluid mechanics in stented arterial model, AIP Conf. Proc., vol 1702, 080008-1–080008-4, (2015), http://dx.doi.org/10.1063/1.4938803, ISBN: 978-0-7354-1349-8, **(ISI, WOS:000371804300034)**.
2. A.F. Totorean, **S.I. Bernad**, R. Susan-Resiga, A helical pipe investigation from cardiovascular perspective, 2014, 12th International Conference of Numerical Analysis and Applied Mathematics 2014, 9th Symposium on Numerical Analysis of Fluid Flow and Heat Transfer, 22-28 September, 2014, Rhodos, Greece, AIP Conference Proceedings 1648, 030033 (2015); doi: 10.1063/1.4912350, **(ISI, WOS:000355339700045)**.
3. **Bernad, S.I.**, Bosioc, A., Totorean, A., Stanciu, R., Bernad, E.S., Vortices in by-pass graft flow, (2013) AIP Conference Proceedings, 1558, pp. 160-163, 11th International Conference of Numerical Analysis and Applied Mathematics 2013, ICNAAM 2013, 21 - 27 September 2013, Rhodes, Greece, ISSN: 0094243X, ISBN: 9780735411845, DOI: 10.1063/1.4825445 **(ISI, WOS:000331472800038)**.
4. **Bernad, S.I.**, Totorean, A., Bernad, E.S., Susan-Resiga, R., Particle motion in coronary serial stenoses, (2013) WIT Transactions on Biomedicine and Health, 17, pp. 169-180, Conference name: 10th International Conference on Modelling in Medicine and Biology, BIOMED 2013, 24 - 26 April 2013, Budapest, Hungary, ISSN: 1743-3525, ISBN: 9781845647063, DOI: 10.2495/BIO130151, **(SCOPUS)**.
5. **Bernad Sandor**, Bernad Elena, Coronary venous bypass graft failure, hemodynamic parameters investigation; International Conference Biomedical Engineering (BioMed 2012), February 15-17, 2012 Innsbruck, Austria, pp. 509-515, ISBN: 978-0-88986-909-7, DOI: 10.2316/P.2012.764-161, 2012, http://dx.doi.org/10.2316/P.2012.764-161, **(SCOPUS)**.
6. **S.I. Bernad**, A.F. Totorean, V.F. Vinatu, R.F. Susan-Resiga, (2010), Particle hemodynamics analysis after coronary angioplasty, Proceedings of the Word Congress on Engineering 2010, Vol 1, June 30 – July 2, 2010, London, UK, pp: 538-588, ISSN: 2078-0958. in Lecture Notes in Engineering and Computer Science, http://www.iaeng.org/WCE2010/, **(SCOPUS)**.

❖ **Books and book chapters:**

1. **S.I. Bernad**, Elena S. Bernad, T. Barbat, V. Albulescu, R. Susan-Resiga, Capter: Effects of different types of input waveforms in patient-specific right coronary atherosclerosis hemodynamics analysis, pp: 55-73 (18 pagini), in Modelling in Medicine and Biology edited by C. A. Brebbia, WIT Press, 2011, Southampton, UK, 220 pages, ISBN: 978-1-84564-4, eISBN: 978-1-84564-573-1, http://www.witpress.com/978-1-84564-572-4.html. (Personal contribution: 18 pages).
2. **S.I. Bernad**, E.S. Bernad, T. Barbat, C. Brisan, V. Albulescu, Capter 11: An analysis of blood flow dynamics in AAA, pp: 191-206, in Etiology, Pathogenesis and Pathophysiology of Aortic Aneurysms and Aneurysm Rupture, editor: Reinhart Grudmann, InTech Open Access Publisher, (2011), Croatia, hard cover, 222 pages, ISBN: 978-953-307-523-5. (http://www.intechopen.com/books/show/title/etiology-pathogenesis-and-pathophysiology-of-aortic-aneurysms-and-aneurysm-rupture). (personal contribution: 16 pages).

3. Balan C., Broboana D., Kadar R., Giurgea C., Rafiroiu D., **Bernad S.I.**, Chapter 9. BioMedical Vortex Flows, pp. 429-492, pages 63. In Susan-Resiga R., Bernad S., Muntean S. (Editors) Vortex Hydrodynamics and Applications, Eurostampa Publishing House, 2007, Timisoara (personal contribution: 12 pages).

❖ Conference committees:

1. Member of the Scientific Committee of the 11th International Symposium on Numerical Analysis of Fluid Flows, Heat and Mass Transfer - Numerical Fluids, 19-25 September 2016, Rhodes, Greece.
2. Member of the Scientific Committee of the 10th International Symposium on Numerical Analysis of Fluid Flows, Heat and Mass Transfer - Numerical Fluids, 23-29 September 2015, Rhodes, Greece.
3. Member of the Scientific Committee of the 9th International Symposium on Numerical Analysis of Fluid Flows, Heat and Mass Transfer - Numerical Fluids, 22-28 September 2014, Rhodes, Greece.
4. Chairman, Workshop on Simulation based Diagnosis, Treatment and Prognosis of Cardiovascular Diseases – CARDIOCOMP, September 14-15, 2006, Timişoara.

❖ Research projects:

1. **Bernad S.**, Bernad E., Barbat T., Albulescu V., Brisan C., Fundamental Research on the particular aspects associated with complex blood flows in the circulatory system pathology with quantification of the implications for placental circulation, Exploratory Research Project PCE 798, Project ID: PN-II-ID-2008-2, Contract no. 658/2009, period 2009-2011. Total value: 410.736 RON. **(Project director)**.
2. **Bernad S.**, Muntean S., Vekas L., Bica D., Sofonea V., Bernad E., Resiga D., Collaborative Research Project CEEX-M1-C2-1180, contract VIASAN no: 81/2006, Computational Optimization Process of the Diagnostic and Prognostic Intervention Therapy for Cardiovascular Diseases – CARDIOCOMP, 2006-2008. (five partners: Romanian Academy - Timişoara Branch - CO, University Politehnica Timişora – P1, University Politehnica Bucharest – P2, University of Medicine and Pharmacy Timişora – P4, Insitutte of Cardiovasculare Medicine Timişoara – P5). Total value 1.395.000 RON (320.000 RON for CO). **(Project director)**.

❖ Member in PhD Juries related to the “Cardiovascular flow hydrodynamics” topic

- Member in the PhD Jury of Alin F. Totorean, Thesis title: Helical flow tubes. Medical applications in coronary bypass surgery. Politehnica University Timisoara, Faculty of Mechanical Engineering, March 2016.

(b-i)_2.1

A). Hemodynamics of the stenosed coronary artery

Introduction

The flow phenomena in the stenotic arteries include asymmetric flow, instabilities, and laminar-to-turbulent transition. The unsteady flow in a stenotic artery also is characterized by high pressure and wall shear stress (WSS) in the throat and distal to the stenosis [1, 2].

Significant stenosis produces loss of perfusion pressure and flows to the distal (post-stenotic) vascular bed [3]. Energy losses along the stenosis produce a pressure gradient between proximal and distal artery regions [4, 5].

Multiple stenoses in diseased vascular bed may occur because of the formation of the primary stenosis that can result in downstream circulation flow. This circulation zone that forms at downstream creates the secondary stenosis. Talukder et al. [6], and Van Dreumel and Kuiken [7] carried out experimental studies of flow dynamics in double constricted vessels. They suggested that the flow energy loss due to the presence of the stenosis directly related to the pressure drops across them increases with the number of stenoses, and is not strongly dependent on the spacing between them.

Kilpatrick et al. [8] presented an assessment of the serial stenosis by summing the value of the resistance for each stenosis. Gould and Lipscomb [9], and Sabbah and Stein [10] concluded that multiple stenoses produce more resistance to flow than a single stenosis of similar length. Johnston and Kilpatrick [11], Bernad et al. [12] simulated the arterial blood flow in triple smooth stenoses. They concluded that the more severe stenosis dominates the pair and the recirculation between stenoses is stronger with a severe proximal stenosis than a severe distal stenosis.

Bertolotti et al. [13] studied the effects of multiple stenoses numerically and experimentally. To evaluate the consequences of the serial stenosis, Bertolotti et al. presented the evolution of the peak systolic velocity ratio and pressure drop during the cardiac cycle.

One method of overcoming the limitations of coronary angiography is the use of invasive physiologic testing by the fractional flow reserve (FFR) technique to assess the functional significance of a coronary stenosis. The FFR is defined as the ratio of maximal blood flow achievable in a stenotic coronary artery about the maximal flow in the same vessel if it were normal [14, 15]. FFR is independent of changes in heart rate, blood pressure, or prior infarction, and takes into account the contribution of collateral blood flow [16, 14].

FFR advances the traditional concept of determining the pressure gradient, the change of pressure between proximal and distal portions within the vessel, by identifying a greater degree of pressure loss for any stenosis more severe than another. The FFR is lesion-specific and can be performed in patients with either single or multi-vessel coronary artery disease (CAD) [17]. Once a percutaneous coronary intervention (PCI) is performed, adequacy of the PCI result can be assessed by FFR with established criteria for a successful balloon angioplasty (FFR ≥ 0.90) and stent placement (FFR ≥ 0.94) [18].

Fractional flow reserve provides important physiologic information about the hemodynamic severity of a coronary lesion and is helpful in the cardiac catheterization laboratory to determine whether PCI can be performed without stopping the procedure and sending the patient for a noninvasive stress test. Patients with CAD often have multiple stenoses within a single coronary artery, one or more of which might be an intermediate coronary lesion. Both computational fluid dynamics (CFD) and FFR can assist in the determination of the clinical significance of each lesion as well as the optimal treatment strategy.

Angioplasty alters the pathophysiology. Although the anatomic result may be acceptable, the physiologic result, at least one based on an FFR of 0.75, is unacceptable.

Study Methods

Hemodynamic flow assessment in coronary arteries is usually performed with intravascular Doppler ultrasound by measuring local velocities (Pilj [19]). What an alternative means for invasive flow measurements is presented by the calculation of models in which blood flow can be virtually simulated, a method that is called computational fluid dynamics (CFD). In fact, several in vitro studies (Talukder [6], Johnston [20], Bernad [21], Dodds [22], Liu [23]) have shown that CFD allows reliable physiologic blood flow simulation and measurements of WSS, wall pressure, and mass flow. A detailed hemodynamic evaluation of disturbed flow in the post stenosis region may give additional insight to understanding the progression of atherosclerosis and may have useful clinical value, such as early detection of a highly stenosed artery segment, prediction of future disease progression, and treatment planning.

Coronary artery reconstruction

A Somatom Sensation 64 Scanner (Siemens Medical Systems, Erlangen, Germany) was used in non-enhanced spiral scan technique with a slice thickness of 2 mm, a table feed of 3 mm/s, and an increment of 2 mm (Figure 2.1 and Table 2.1). The coronary angiography (CA) and the spiral computed tomography (CT) investigation detected multiple severe right coronary arteries (RCA) stenoses (Figure 2.1). According to the NASCET (North American Symptomatic Carotid Endarterectomy Trial) [24] and ECST (European Carotid Surgery Trial) [25] method of stenosis classification, the severity of the stenosis illustrated in Tables 2.2 and 2.3. The percentage diameter reduction for a circular stenosis is 1-d/D, where d is the diameter of the lumen and D the diameter of the unoccluded artery.

Figure 2.1: Physiologically realistic geometry measurements using CT image techniques. Area measurements of the different stenosed section. For position of section D6 see Figure 3.2.

Table 2.1. Patient characteristics

Variables	Value
Age	44
Gender	Male
History of myocardial infarction (MI)	NO
Previous percutaneous transluminal coronary angioplasty (PTCA)	NO
Renal insufficiency	NO
Cardiovascular risk factor	
Hypertension	Yes
Diabetes	NO
Smoke	Yes
Obesity	Moderate

Table 2.2. Angiographic and computed tomography (CT) scan investigation data

	Angiographically	CT scan
Main findings		
Studied coronary artery		
Right coronary artery (RCA)	Serial stenosis (3 stenoses with area reduction percentage of: 83%, 52% and, 83% respectively)	Serial stenosis (3 stenoses with area reduction percentage of: 79%, 48% and 78%, respectively)
Left anterior descending (LDA)	Single severe stenosis (93 % area reduction)	Single severe stenosis (90 % area reduction)
Reference artery diameter [mm]		
RCA	3.9	3.8, 3.6 and 3.6
LDA	3.6	3.5
Obstruction diameter [mm]		
RCA	1.6, 2.7 and 1.6	1.76, 2.6 and 1.68
LDA	1	1.11
Collateral circulation	NO	NO

Figure 2.2 shows the reconstructed lumen geometry of the RCA viewed from the epicardial and pericardial sides. The lumen inlet diameter (at the ostium, section D0 in Figure 2.2B) of the RCA was 3.8 mm. Modeled RCA was 52 mm in length with variable diameters, depending on the stenosis severity. Table 3 shows data corresponding to the reconstructed RCA.

Table 2.3. RCA stenosis severity

Stenosis	Reference diameter [mm]	Stenosis minimal diameter [mm]	Stenosis length [mm]	Diameter reduction percentage [%]	Area reduction percentage [%]	Stenoses severity
ST1	3.8	1.76	12	54	79	Severe (70-99%)
ST2	3.6	2.6	7	28	48	Moderate (30-69%)
ST3	3.6	1.68	7	53	78	Severe (70-99%)

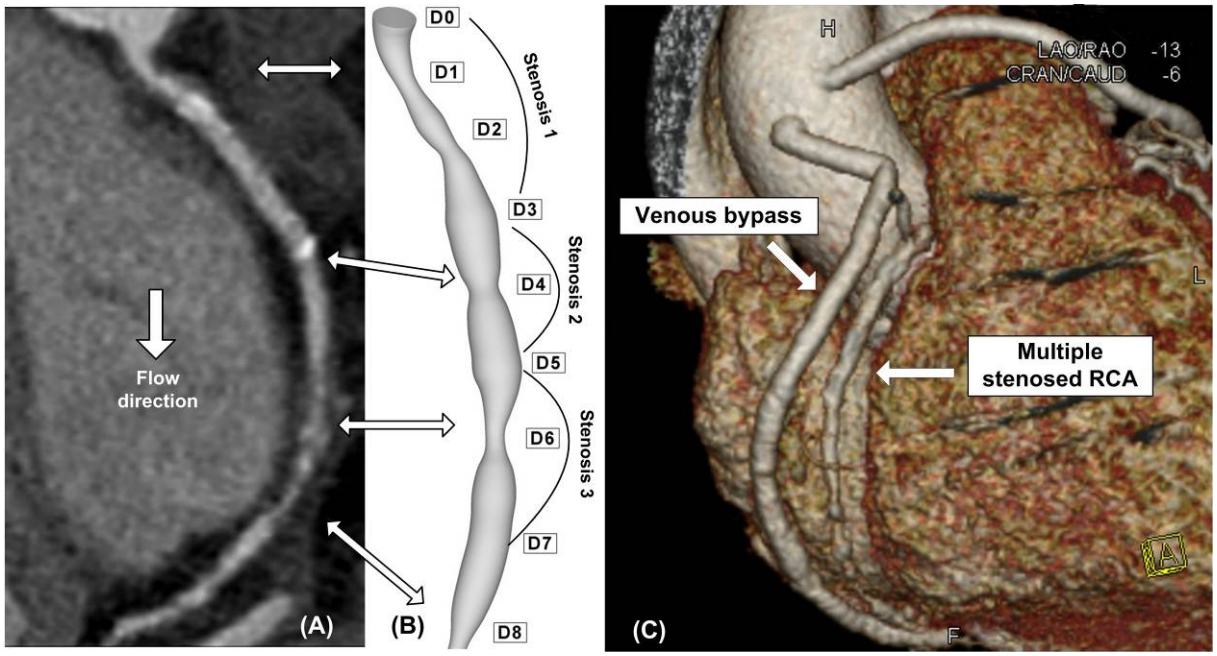

Fig. 2.2 Patient-specific right coronary artery (RCA); (a) ortogonal-curved multiplanar reconstructions image which indicate a multiple coronary stenosis at the right coronary artery; (b) geometry reconstruction; (c) volume-rendered image shown narrowed venous by-pass graft and serial stenosis in RCA (Bernad et al [21]).

Coronary pressure and flow measurements

Relevant physiological data required an accurate signal acquisition. Pressure and flow velocity signals were acquired with nearly identical methods. After diagnostic angiography, a sensor guidewire was passed through an angioplasty Y-connector attached to a guiding catheter. Phasic and mean aortic pressures were measured by the guiding catheter and phasic and mean coronary pressures by the pressure wire.

The pressure wire was positioned distal to stenosis ST3 and pulled back slowly to the RCA ostium during sustained hyperemia. A significant pressure drop, DP(ST3), was observed when the sensor crossed stenosis ST3 but a much smaller pressure drop, DP(ST2), was present across stenosis ST2. This finding suggests that stenosis ST2 was not very severe from a functional point of view. Finally, crossing stenosis ST1, the sensor measured again a significant pressure drop, DP(ST1), comparable with pressure drop in stenosis ST3.

Computational fluid dynamics

For meshing procedure the commercial grid generation software, GAMBIT 2.4.6 (ANSYS FLUENT, ANSYS, Inc.), was used [26].

To carry out the mesh sensitivity analysis, numerical simulations were carried out by varying the number of mesh elements in the computational domain. The accuracy of the simulation results was improved by employing a finer mesh that contained 1,598,752 elements.

The blood was assumed to be incompressible behavior having a dynamic viscosity (μ) of 0.00408 Pa.s and density (ρ) of 1050 kg/m3.

In healthy vessels, there is a laminar flow, but narrowed vessels can lead to relatively high-Reynolds numbers and disturbed flow, resulting in transition or turbulence [13].

A large number of experimental studies [27], [28], [29] and computational [30], [31], [32]) studies of the hemodynamics in diseased arteries exhibit disordered and turbulent flows in such vessels. Turbulence can significantly affect the pressure and shear stress downstream of the stenosis [33].

Simulations were carried out over a range of Reynolds numbers from 250 to 1200. The maximal Reynolds number during the cycle was about 1118. The k-ε turbulent model used in the present simulation was capable of predicting low Reynolds number transitional flows inside the stenosed coronary artery. The blood flow was simulated with the commercial CFD FLUENT 6.3 package [26], parallelized across eight 3.2 GHz Intel processors of a TYANPSC T-650 Rx (Tyan Computer Corporation, Taiwan, parallel computing machine). For the visualization and quantification of the flow patterns, the TECPLOT (Tecplot, Inc., Bellevue, WA) software (Version 10.0) was used.

The boundary conditions required to solve the governing equations are as follows:

- The walls were taken as robust and stiff, and a zero-velocity boundary condition was assumed for the walls, corresponding to a no-slip condition.
- The inlet was identical to the real coronary ostium and every point at the inlet had same flow parameters, including direction and velocity.
- The flow velocity profile at the inlet was based on data reflecting the physiologically pulsatile, biphasic blood flow from the ascending aorta into the coronary arteries, and the pressure profile reflecting the value measured in distal part of the artery (Figure 2.4).

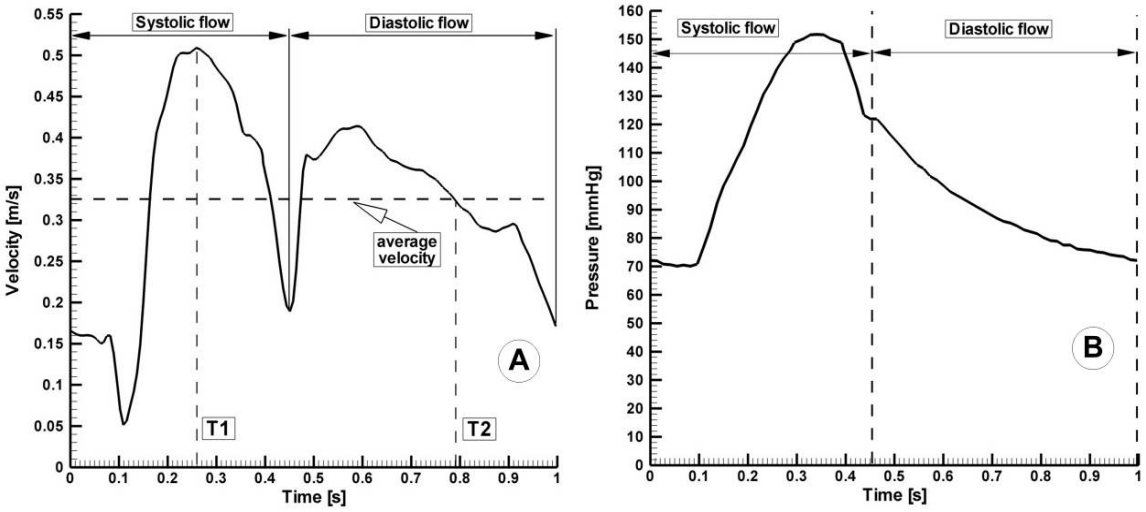

Fig. 2.4. Pulsatile inlet flow condition. Physiologically realistic velocity waveform based on flow and pressure waveforms was acquired with an intravascular ultrasound Doppler probe in the RCA(predominant systolic pattern).(A) Velocity input waveform. (B) Pressure output waveform.

Pressure distribution in multiple stenosed coronary artery

Figure 2.5 shows the pressure distributions along the axial direction with time for the investigated stenosed RCA. The pressure drop increased with the increase of percentage stenosis. In stenoses ST1 and ST3, the pressure dropswere significant during the systolic phase (Time T1=0.26 s): 32.84 mmHg and 36.78 mmHg, respectively, while during the diastolic phase at the time T2=0.79 s the pressure drops across tenoses ST1 and ST3 were lower (4.62 mmHg and 4.81 mmHg). For stenosis ST2, the pressure drop across the stenosis was lower during the peak systolic phase (1.46 mmHg) and was practically negligible during the diastolic phase (0.03mmHg) (Table 2.4).

Table 2.4. Artery flow parameters in the investigated stenosis.

Stenosis	Time	Q [l/min]	ΔP [mmHg]	Re_{throat} [-]	$Vmax_{throat}$ [m/s]
ST1	T1	0.351	32.84	1141	2.27
	T2	0.113	4.62	369	0.734
ST2	T1	0.37	1.46	865	1.165
	T2	0.118	0.03	275	0.371
ST3	T1	0.35	36.78	1118	2.33
	T2	0.112	4.81	361	0.752

Overall pressure drop increased appreciably with flow rate (at the peak systole, Figure 2.5). Values of the overall pressure drop increased from 1700 Pa (12.75 mmHg) at time T2 to 11000 Pa (82.5 mmHg) at time T1 (Figure 2.5). At time T1, pressure drop to the minimal throat value (stenosis ST3) increased from 4.81 mmHg at 112ml/min to 36.78 mmHg at 351 ml/min (Table 3.4). The increased pressure drop in stenoses reflected the high energy needed to drive the flow through these regions.

To understand the pressure–flow relationship, the pressure drop across each constriction was evaluated in Figures 2.6 and 2.7 at time T1. Pressure drop variation depended on whether the flow was accelerating or decelerating and also on the exact state of these two phases (Table 2.4).

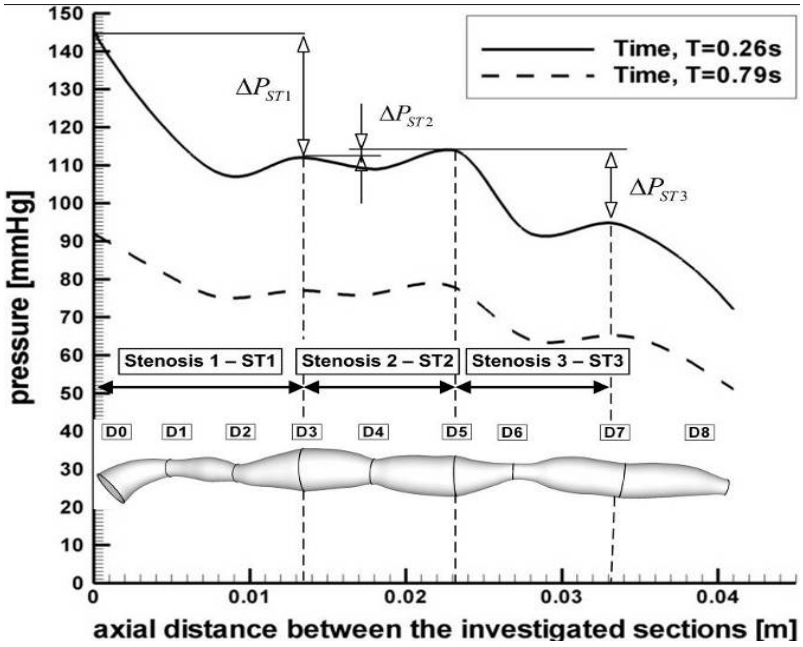

Figure. 2.5 Pressure drop across the investigated serial stenosed RCA.

Energy loss associated with such flow expansion after each constriction was large (E Bernad et al [37]), and consequently, the pressure drop would be higher (Figure 2.5). The pressure drop associated with spacing between sections D2 and D3, and D6 and D7 during the peak flow (time T1) may be attributed to the greater energy loss related to intense re-circulation zones and related vortex shedding downstream to stenosis ST1 and ST3 (Figure 2.6).

In hydraulic terms, the pressure drop over the stenosis may arise from pressure losses due to the higher residual stenosis, or to flow turbulence distal to the stenosis. As shown in Figure 2.5 with different degrees of stenoses, a severe stenosis caused a considerable pressure drop across the throat.

Coronary stenosis physiology is based on the curvilinear relation between flow increases and different degrees of pressure loss (Figure 2.7). The combination of pressure gradient and flow velocity is suited to assess changes in stenosis hemodynamics.

The resistance to flow through the stenosis was caused by viscous friction, flow separation, turbulence, and eddies. This condition produced energy loss along the stenosis. Energy loss produced pressure loss distal to the stenosis and thus a pressure gradient across the narrowed segment (Figures 2.5 and 2.7). The pressure loss is increased with increasing coronary flow along a quadratic pressure drop–flow relationship ($\Delta P=k1\cdot Q+k2\cdot Q2$) of the specific coronary stenosis (Figure 2.7). In this equation k1 and k2 are constants of viscous and separation losses that are determined by the geometry of the stenosis and fluid properties of blood.

Figure 2.7 shows that when flow increased, the distal pressure decreased (pressure drop in stenosis ST3). However, when a stenosis was present, the maximal flow at any given arterial pressure was lower.

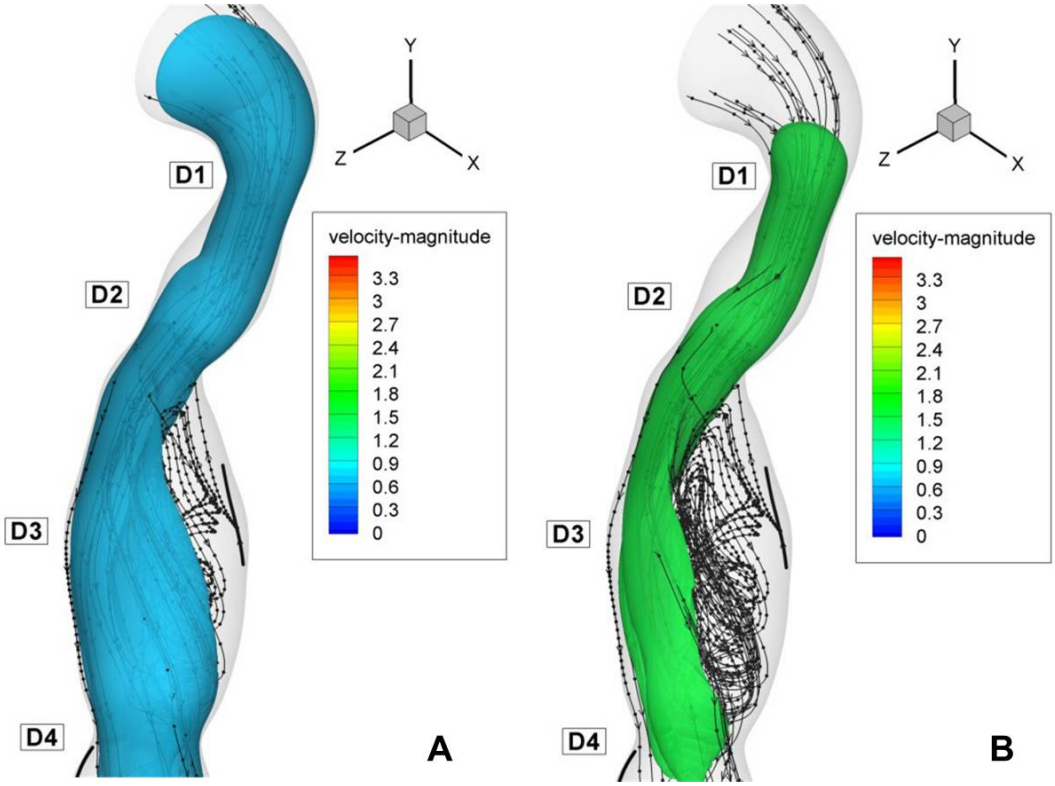

Figure 2.6. Disturbed flow indicators at the time T2=0.26 [s]. (a) velocity isocontour for blood velocity V = 0.3 [m/s]; (b) stream treace and velocity isocontour for blood velocity v=2 [m/s] downstream to the stenosis ST1.

Consequently, blood flow through that artery would further decrease and, therefore, the pressure gradient across the first stenosis would also decrease. When a stenosis was present, this progressively decreased the maximal flow because the resistance of the stenosis was added to the resistance of the microcirculation.

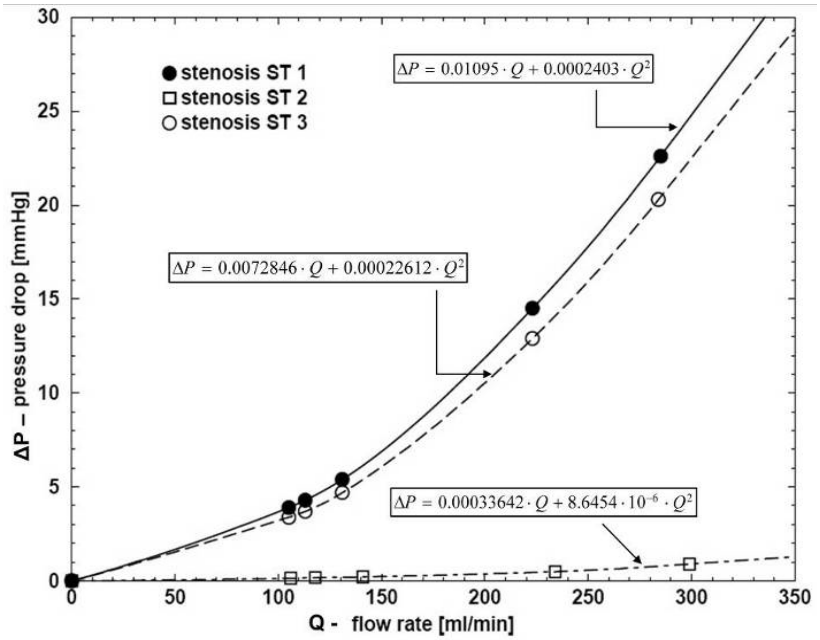

Figure 2.7. Flow velocity-pressure gradient relation in a patient with multiple stenoses. Line shows the regression line, according to the formula:$\Delta P=k1 \cdot Q+k2 \cdot Q^2$, at time T1. Time T1 correspond to the time step indicated in Figure 2.4.

Flow separation and secondary flow in stenosed coronary artery

Coronary flow velocity is measurable and can provide a graphic demonstration of the changes in coronary flow over time and in response to different stimuli (Figure 2.8).

The flow separation regions can be seen clearly from the instantaneous velocity field panels which are illustrated in Figures 2.6 and 2.9 for stenosis ST1 and ST3. One can observe the pattern of velocity vector distinctively showing the recirculation zones with the formation of the eddy at the downstream couple of stenoses.

From this figures, it can be observed that the recirculation eddies are formed downstream of the each stenosis. There exists a separation streamline that divides the flow into two regimes one of which is the recirculating region distal to each stenosis, and the other is the main flow field carrying the bulk of the movement near the center of the tube.

Development of the recirculation zone downstream to the each constriction is restricted by the presence of the next stenosis.

The peak velocities value from the current simulations are compared with in vivo measured data by Di Mario et al. [35].

The results of our simulation show that the peak velocity at the throat of the stenosis ST2 is about 1.165 m/s (in 28% diameter reduction stenosis), at the throat of the stenosis ST1 is 2.27 m/s (in 53% diameter reduction stenosis) against a value of 0.78 m/s in healthy arteries (Table 2.5). We mentioned that our result is in good correlation with both the experimentally measured data by Li et al. [36] and in vivo measured data by Di Mario et al. [35], and Siebes et al. [37].

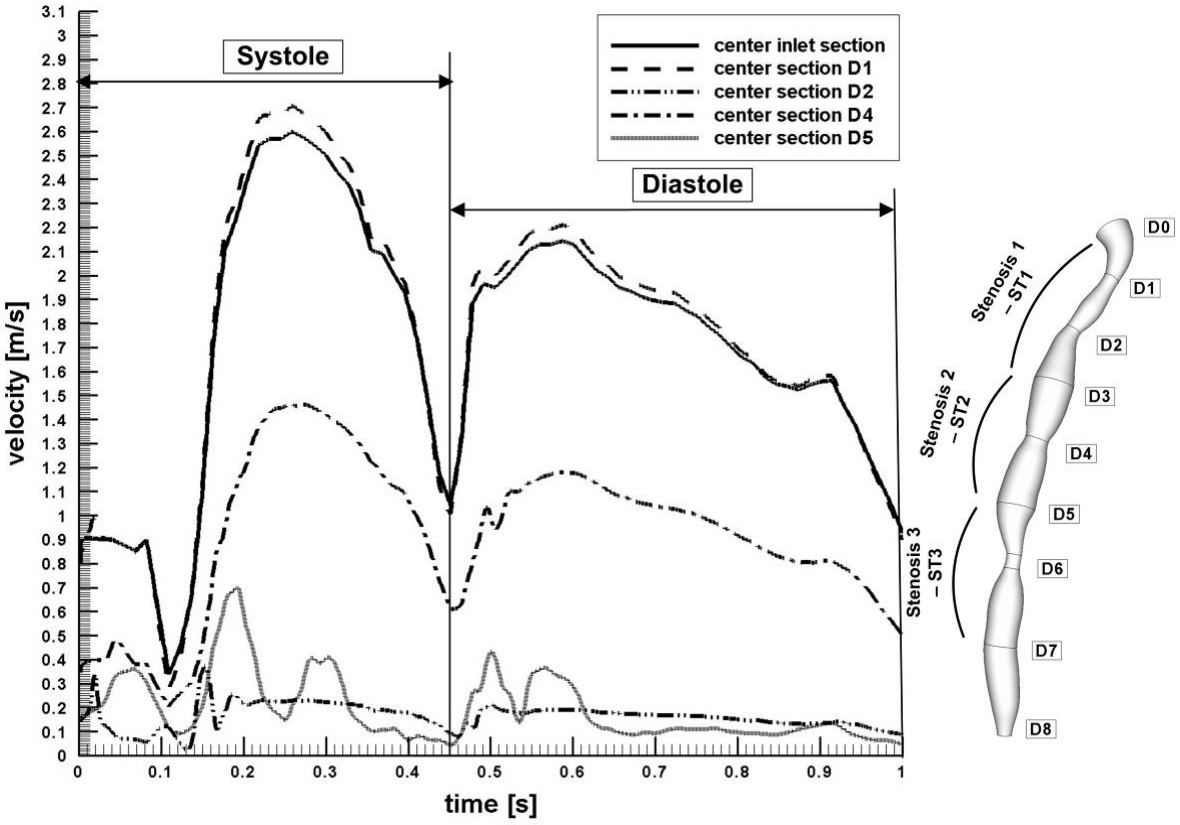

Figure 2.8. Velocity evolution for different investigated sections during to the cardiac cycle.

At the peak flow rate, the Reynolds numbers at the narrowest points in 28%, 53%, and 54% stenoses (stenosis ST2, ST1 and ST3) are about 865, 1141, and 1118, respectively. In the stenosis ST3, the maximum Reynolds number at the throat decreased because of the decrease of flow rate. Downstream of stenosis, flow might become transitional because of the sudden expansion and strong recirculation (sections D3 and D7, Figure 2.9).

Table 2.5: Comparison of the our results with experimental and vivo data from the literature.

Hemodynamic characteristics	**Present study**		**In vivo data**	
	%DS	Value	%DS	Value
Peak velocity [m/s]	28% - ST2 53% - ST1	1.165 2.27	- [1]69.1±4.8%	- 2.1±2.8
Reynolds number in the throat [-]	28% - ST2 53% - ST1	865 1141	- [1]74.3±3.7%	- 957
Peak WSS [Pa]	28% - ST2 53% - ST1	110 210	- [1]69.1±4.8%	- 184
Pressure drop [mmHg]	28% - ST2 53% - ST1	0.03 32.84	- [2]52.2±8.6%	- 36.9±17.3

%DS percent diameter stenosis; * pressure drop from the inlet to the throat; [1]Di Mario et al. [35]; [2]Siebes et al. [37].

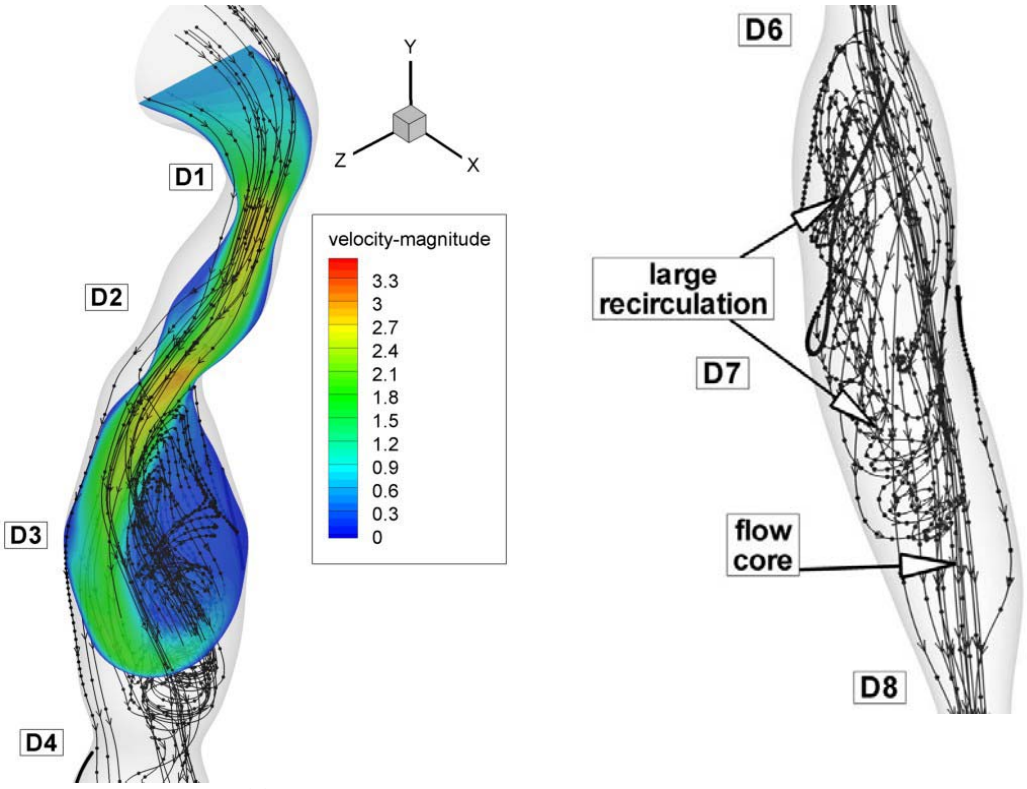

(a) (b)

Figure 2.9: Disturbed flow indicators at the peak systole T2 = 0.26 [s]. (a) stenosis ST1; (b) stenosis ST3.

Figures 2.6 and 2.9 shows that the post stenotic deceleration of blood flow induces flow separation and recirculation zones (Bernad E. et al [38]). Such regions of flow separation are favored sites for the development of thrombosis and atherosclerosis [39].

Intimal thickening and Wall Shear Stress in artery stenoses

In the case of post-stenotic regions, the areas of low wall shear stress are associated with flow separation (Figures 2.9 and 2.10). This may be substantial because it has been suggested that the fluctuation of the wall shear stress or disturbed flow leads to increased endothelial cell turnover and intimal thickening. Importantly, in vivo study has shown that the post-stenotic region of subcritical stenoses, for example, less than 60%, is associated with increased intimal thickening, and this intimal thickness also correlated inversely with shear stress [40]. If the blood flow is increased, that increased wall shear stress, an adaptive increase in arterial luminal size is observed. If the blood flow is decreased, usually by a proximal stenosis that decreases the wall shear stress, there is an adaptive decrease in arterial lumen size [41].

In figures 2.10 and 2.11, all shear stress distribution shows a close reflection of the outline of the stenoses. The point where the maximum shear stress occurs lies at the narrowest cross-section D4 for stenosis ST2 and section D6 for stenosis ST3. In Figure 2.10a, the separation region at the time T2 occurs at the downstream of the stenosis ST1 and ST2 in sections D3 and D5. There is a rapid increase in wall shear stress upstream of the first stenosis, then after the critical height of stenosis (section D2 and D4), the wall shear stress decreases until separation occurs (Bernad et al [42]).

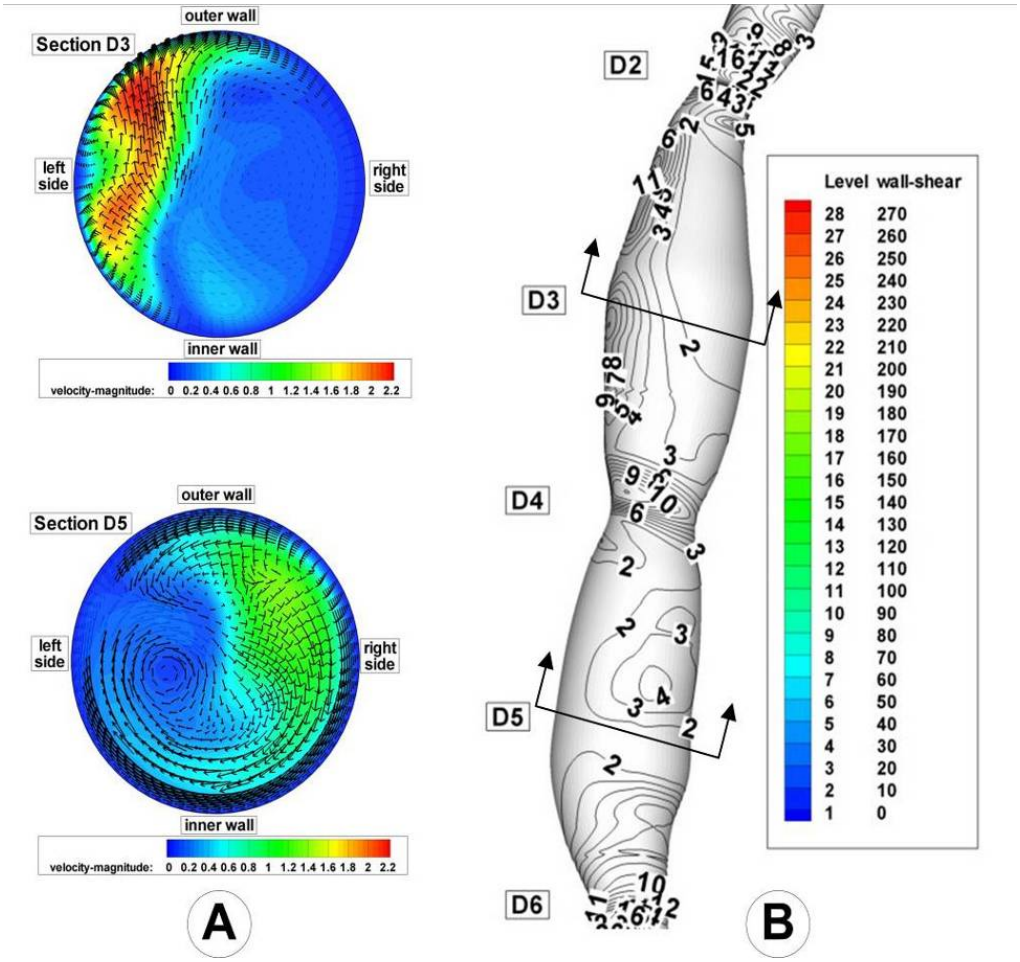

Figure 2.10: Disturbed flow indicators at the peak systole T2 = 0.26 [s]. (a) cross-sectional transient velocity vector fields; (b) temporal WSS magnitude contours in stenosis ST1 and ST2 (WSS value are in [Pa]).

Figures 2.10b shows wall shear stress (WSS) distributions at the time T2=0.26 s, the time where the flow is at a maximum (peak systole). The range of WSS in this figure varies from 5 to 234 Pa as opposed to 5 to 45 Pa at the time T4=1s (Figure 2.11b). Three intense regions of low WSS appear downstream at the each stenosis (Figures 2.10b and 2.11b). For the each this regions the WSS is approximately 5 Pa. One the opposite side of this region we have the regions of moderate and high WSS (WSS varies from 15 to 90 Pa at the time T2 and from 15 to 30 Pa at the time T4).

As the flow decelerates the regions a high WSS begin to dissipate and more regions of moderate and low WSS begin to appear (time T4, Figure 2.11b).

The location of the WSS peaks agrees well with clinical observations of elevated mass transfer in stenoses, i.e., mass transfer occurs on the fore and aft sides of the occlusion and not the throat [42].

Our study shows that the peak WSS reached 110 Pa at the throat of the stenosis ST2 (28% diameter reduction) which is high enough to damage the endothelial cells. Both, high wall shear and stagnant flow regions have been identified as favorable conditions for platelet aggregation through inherently different pathways [44].

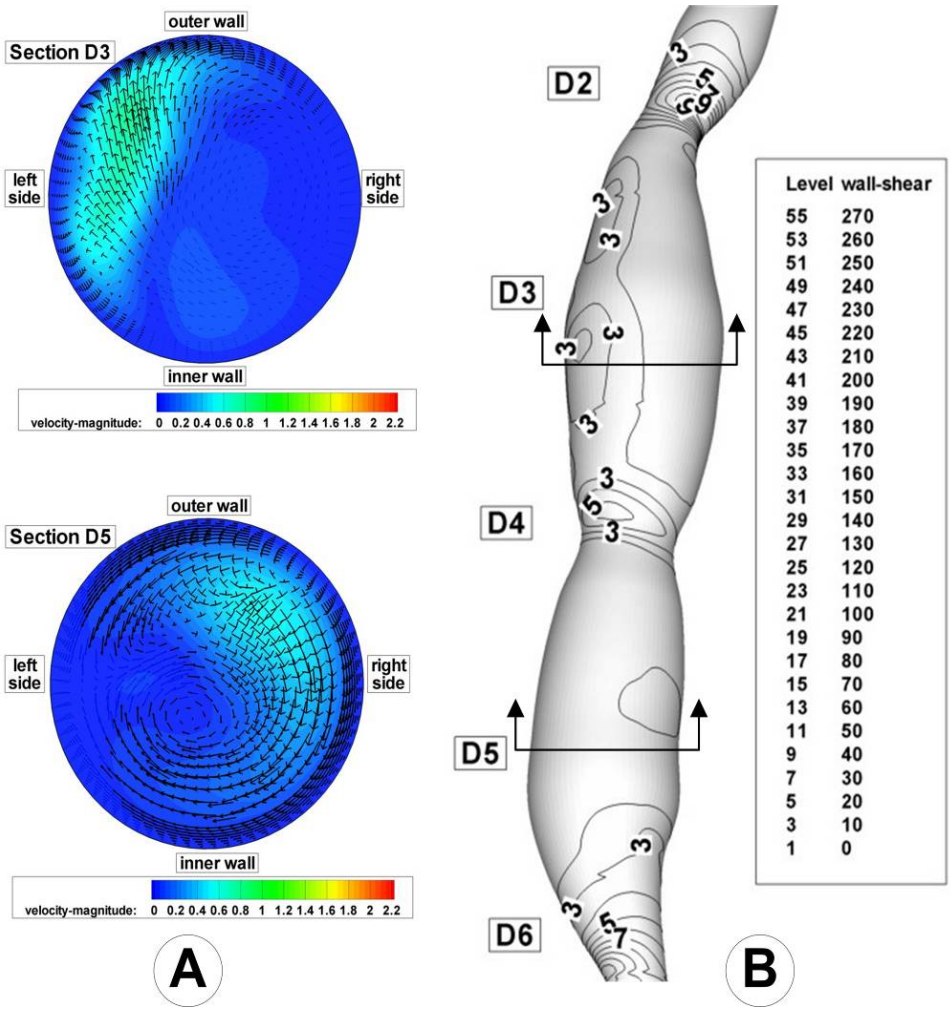

Figure 2.11: Disturbed flow indicators at the end of diastole T4 = 1 [s]. (a) cross-sectional transient velocity vector fields; (b) temporal WSS magnitude contours in stenosis ST1 and ST2 (WSS value are in [Pa]).

Conclusions regarding the blood hydrodynamics in stenosed coronary artery

The dynamics of the flow describing pressure drop, the formation of recirculation for the multi-constricted RCA flow and examination of numerically defined FFR were studied in the present investigation. The results of maximum blood velocities from this study were consistent with the published clinical measurement, indicating that the model used was physiologically realistic.

Results from different degrees of stenoses show that severe stenosis caused a considerable pressure drop across the throat.

We can conclude that:

- local hemodynamic factors are crucial to determining the evolution of coronary obstructions;
- the parameters that govern the unsteady flow dynamics in a vessel with multiple constrictions are Reynolds' number, the degree of stenosis and the spacing between the stenosis;
- the pressure drop across the stenosis decreases with Reynolds number;

The study also indicates that the presence of one stenosis in a coronary artery affects the hemodynamic appearance of the other. As shown in this study, it is possible to calculate this effect quantitatively by measuring pressures at the relevant sites within the artery. Taking into account the complexity of the fluid dynamics in the multiple sequential stenoses, the severity of stenoses cannot be adequately assessed only by visual interpretation of the coronary angiogram.

This analysis indicates the usefulness of coronary pressure measurement, especially that of the non-invasive technique of numerical simulations, for evaluating the individual hemodynamic effects of each of several sequential stenoses within the same coronary artery. Therefore, we believe that our observations can serve as guidance for future implementation decisions.

To achieve a more accurate range of errors, a further array of different serial stenosed arterial segments (left anterior descending artery (LAD) and the circumflex artery) could be analyzed. Also, a different number of serial stenosed models should be studied and compared.

B). Flow characteristics in narrowed aorto-coronary bypass graft

Problem description

Conduits considered acceptable to revascularization the right coronary artery (RCA) system include the right gastroepiploic artery (RGEA) [45], the right internal thoracic artery (RITA) in situ or used in a Y graft configuration [46], the free radial artery (RA) implanted into the aorta or into the left internal thoracic artery [47], and the saphenous vein graft (SVG) [48].

Vein bypass grafting is one of the primary options for the treatment of arterial occlusive disease. Aorto-coronary saphenous vein graft disease is comprised of three distinct but interrelated pathological processes: thrombosis, intimal hyperplasia and atherosclerosis.

Vein graft occlusion may occur early or late and is due to three distinct, well described disease processes. Acute graft failure and thrombosis may occur in the first 30 days postoperatively, and affects up to 12% of vein grafts [49]. Neointimal hyperplasia occurs between one month and a year, and is the result of accumulation of smooth muscle in the intimal layer [50].

The pathogenic effects of the saphenous vein graft disease risk factors are amplified by loss of the anatomic and functional integrity of the endothelium during and after grafting and by transposition of the vein into the high-pressure arterial circulation.

Transposition of a vein segment from a low flow and pressure environment into the high flow and pressure arterial system leads to significant structural changes within the wall. These changes are characterized by an increase in both intimal and medial thicknesses. These early events in vein graft adaptation frequently continue in an uncontrolled manner, leading to severe lumen narrowing and subsequent graft failure [51]. Shear stress has been recognized as one of the major hemodynamic factors which modulate vein graft remodelling.

Flow rate as an important determinant of early aorto-coronary vein graft failure, a range of studies have confirmed the correlation between low wall shear, accelerated lumen loss, and reduced vein graft patency [52 – 54].

The scope of this paper, is to cover the fundamental aspects of the blood flow in the failed aorto-coronary saphenous bypass graft, and used this information's in clinical practice for vascular surgery.

Patient Characteristics and Angiographic Data

The clinical characteristics of the patient are presented in Table 2.1. Hypertension was defined as a recorded preoperative blood pressure >140/90 mmHg or pharmacological treatment for hypertension.

Quantitative Coronary Angiography (QCA) and Computed tomography (CT) angiography

Quantitative angiographic analysis of pre-operative angiograms provides information likely to influence the choice of the most adequate graft conduit in patients who are candidates for coronary bypass grafting of the RCA (Figures 2.1 and 2.2). Reference diameter (RD), minimal luminal diameter (MLD), and stenotic diameter (SD) were calculated as the mean of both views using the guiding catheter as a scaling device (Table 2.3).

The coronary angiography (CA) and the spiral CT investigation detected a multiple sever right coronary artery (RCA) stenosis (Figures 2.1 and 2.2). The clinical solutions for this patient are the venous bypass graft for the RCA (Figures 2.12 and 2.14). Table 2.6 shows the characteristics of these bypass grafts.

The long-term success of coronary artery bypass graft surgery (CABG) is dependent on graft patency after the operation. It is established that aspirin (325 mg daily) improves saphenous vein graft patency early (7 to 10 days) and at 1 year [55 - 57].

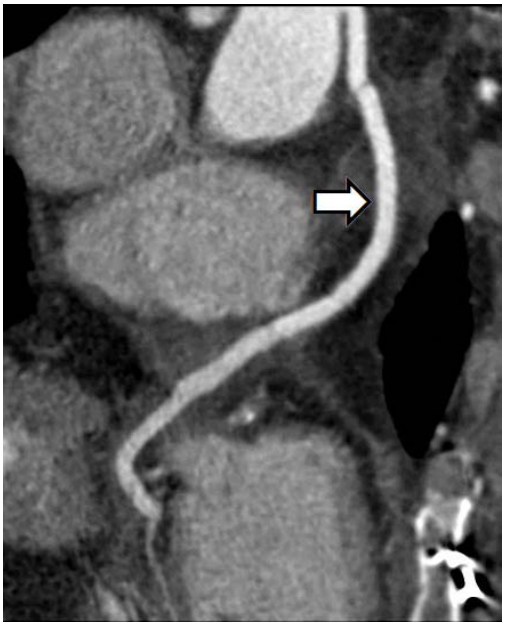

Figure 2.12. Venous bypass graft of right coronary artery (*arrow*). MDCT two-dimensional curved multiplanar reconstruction.

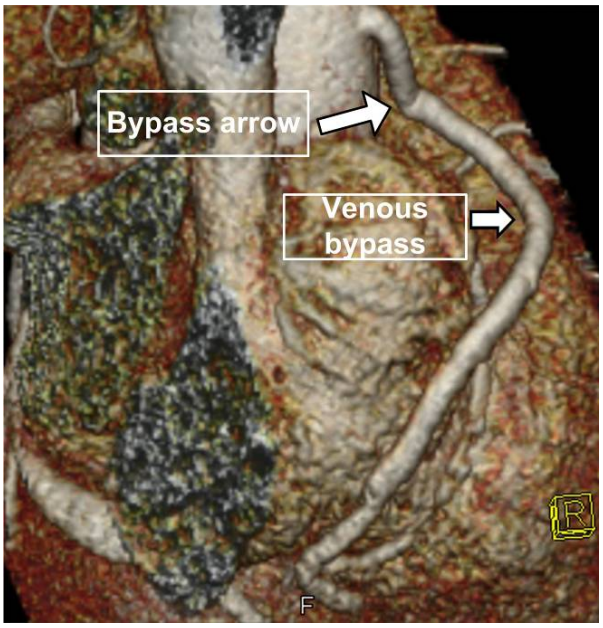

Figure 2.13. Multidetector computed tomographic (MDCT) angiography in a 44 year old male CABG patient with venous grafts (arrow). Three-dimensional reconstruction of the heart and vessels with volume rendering techniques.

Table 2.6. Bypass graft characteristics

Variables	Value
Vein grafts	
Single vein graft	Yes
Vascular territory perfused by graft	
RCA	Yes

RCA = right coronary artery.

The assessment of graft patency in a non-invasive manner would have major benefits for the management and treatment of patients with prior CABG. Multidetector computed tomography (MDCT) technology is used for non-invasive bypass graft assessment [58 - 60].

Computed tomography has many advantages over invasive coronary angiography, including a lower complication rate, better ostial imaging and easy visualisation of vessels with anomalous origin and those where catheterisation has failed. Bypass graft known to be patent at 7 to 10 days after the operation. Computed tomography method is used in order to assessing aorto-coronary saphenous vein bypass graft patency (Figures 2.12 and 2.13).

Venous bypass geometry

The bypass geometry is result from spiral CT (computed tomography) images performed 7 days following to the revascularization procedure. Geometry reconstruction was based on axial images, multiplanar reconstruction images, and 3-dimensional volume-rendering images.

Investigated bypass model are presented in Figure 2.14 ((a) bypass position during the surgery and (b) bypass position find during the assessing of the graft patency using computed tomography). The bypass graft is modelled to be of length 118 mm with diameter 4.2 mm (average size was 3.9 ± 0.4 mm [61]). In Figure 5b, the venous grafts have a uniform circular cross-section, which are larger than the investigated RCA (3.2 mm).

CT investigation shown severe changes in the shape of saphenous vein graft 7 days after surgery. Figures 4 and 5 present two regions with severe shape remodelling first is an elbow type contortion and second is a severe curvature with tortuous area reduction (Figure 2.14c).

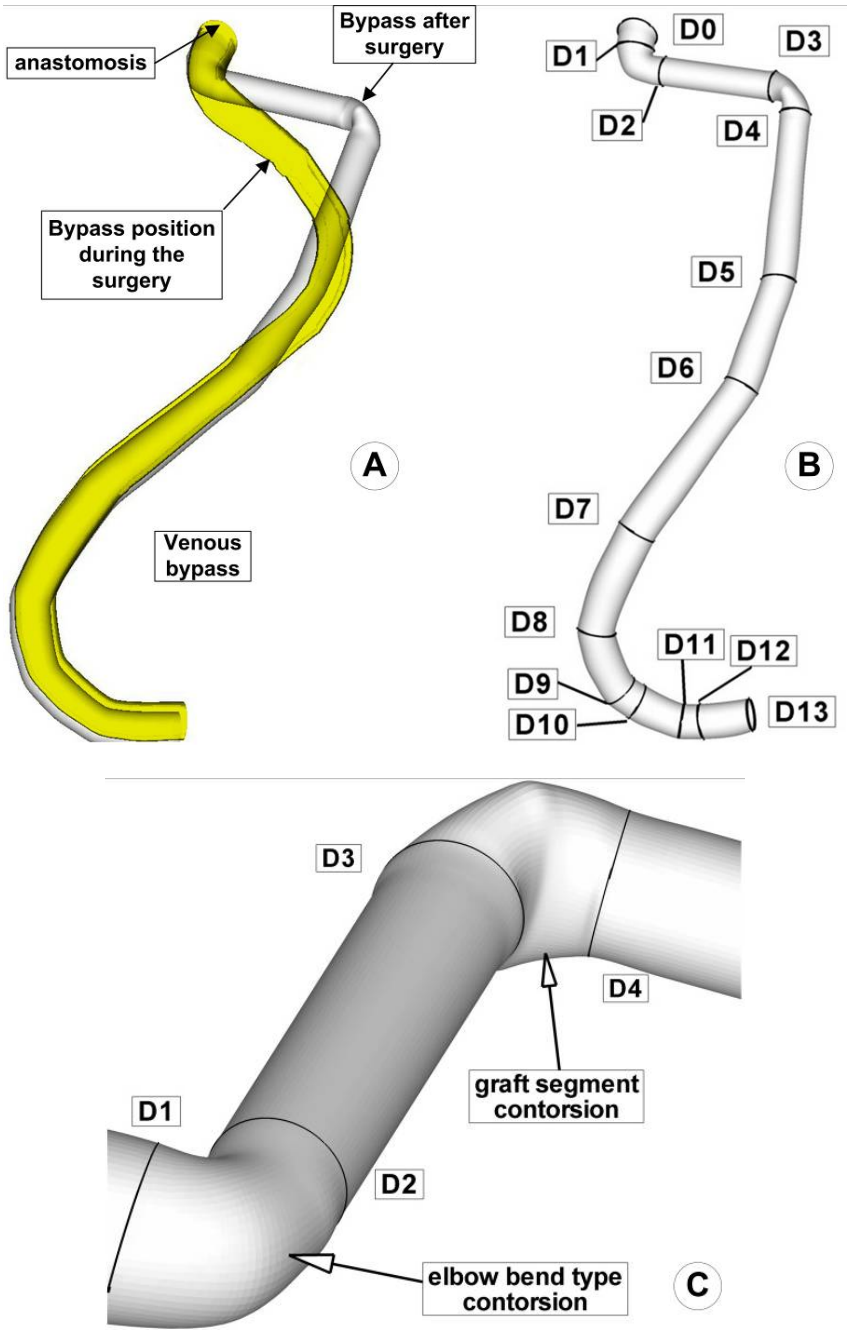

Figure 2.14. Patient-specific aorto-right coronary artery venous bypass graft. (a) Graft position during the surgery and 7 days after the surgery. (b) Venous graft geometry after surgery: dimension and different investigated sections (D0 = anastomosis section at the ascending aorta–inlet section, D13 = outlet section). (c) Detail regarding vein graft shape remodelling after surgery.

Computational fluid dynamics

Computational mesh

An effective meshing procedure in this study is one that can mesh the CT scan image surface geometry without compromising the geometric features. To achieve this task the commercial grid generation software, GAMBIT 2.4.6 (ANSYS FLUENT, ANSYS, Inc.) was used [26].

Four different meshes with boundary layer mesh were investigated. The number of cells varied between 860,000 and 1,200,000 (mesh 1 = 860,000 cells, mesh 2 = 954,876, mesh 3 = 1,040,668 and mesh 4 = 1,210,360 cells). A high mesh resolution near the walls was needed for accurate values of pressure drop and WSS. Thus the mesh was refined in the near-wall region. A boundary layer consisting of ten rows with a growth factor of 1.15 (ratio between two consecutive layers near the wall) was generated. To model the flow close to the wall, standard wall-function approach are used, the enhanced wall functions approach has been used to model the near-wall region.

This mesh was chosen based on the results of a mesh-independence study. The relative error in the velocity field in centre of section D9 (Figure 2.16) was calculated and used as a quantitative measure of the effect of grid density. The relative errors in the velocity field for mesh 1 and mesh 2 compared with velocity field for mesh 4 are 13.5% and 5.8% respectively. We determined that this grid was too coarse. The relative errors in the velocity field for mesh 3 are 3% compared to the current mesh (mesh 4) (Figure 2.15), and we determined that this grid was fine.

Note that recent simulation study of arterial flows presented in the literature [62], [63], it shown that about 600,000 grid nodes are required to achieve grid independence in the WSS field. Since our objective is to qualitatively study the unstable flow, the grid containing 1,200,000 cells (mesh 4) (Figure 3.15) can be considered as a good compromise between accuracy and computational cost.

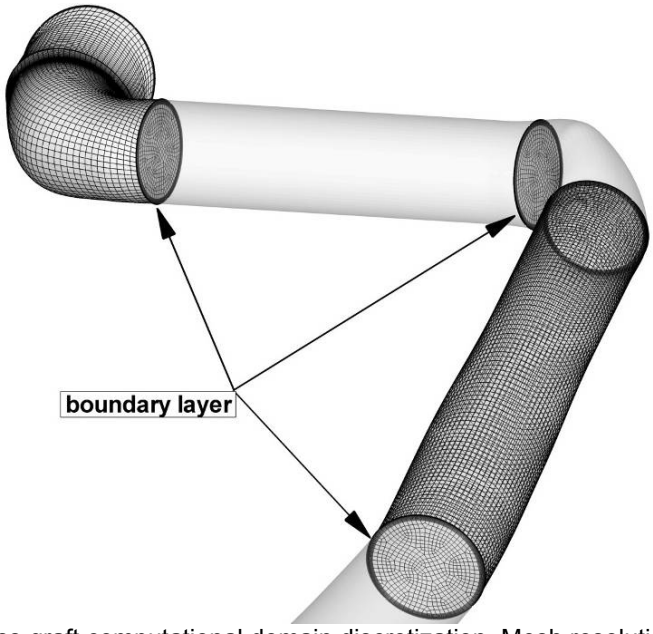

Figure 3.15. Bypass graft computational domain discretization. Mesh resolution in the narrowed region. A boundary layer consisting ten rows with a growth factor of 1.15 (ratio between two consecutive layers near the wall) was generated.

Boundary conditions

Computational assumptions and boundary conditions are the following: the blood is assumed incompressible having dynamic viscosity (μ) of 0.00408 Pa and a density (ρ) of 1050 kg/m^3. The venous bypass walls are considered rigid and impermeable. As usually adopted by most previous investigations, the distensibility of the blood vessel wall is neglected. Torii et al. [62]

used the coupled FSI analysis of the human RCA in conjunction with physiological velocity and pressure waveforms to investigate the effects of wall compliance on coronary hemodynamics. Comparison of the computational results between the FSI and rigid-wall models showed insignificant difference in TAWSS and OSI. Zeng et al. [63] investigate a disease-free RCA with in vivo flow waveform, physiological realistic compliance data and artery motions. Conclusion is that coronary compliance has little influence on hemodynamic parameter WSS (wall shear stress).

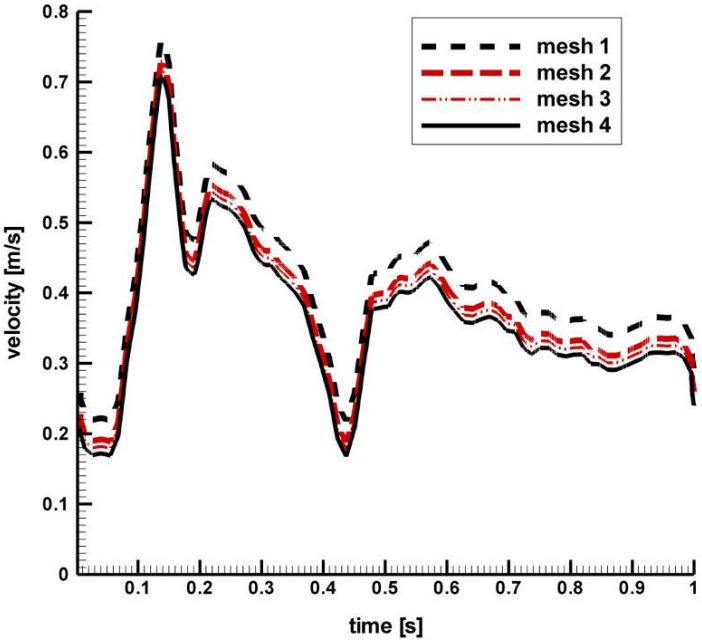

Figure 2.16. Mesh-independence study. Velocity evolution in centre of the section D9 (Figure 2.14b). Four different meshes with boundary layer mesh were investigated (mesh 1 = 860,000 cells, mesh 2 = 954,876 cells, mesh 3 = 1,040,668 cells, mesh 4 = 1,210,360 cells).

Houslay et al. [64] used computed tomography to assess coronary bypass grafts patency. Conclusion is that bypass grafts are less susceptible to cardiac motion artefacts than native vessels.

Johnston et al. [11] compared the effects of different blood viscosity models on the velocity and WSS distributions in the RCA during the cardiac cycle. Conclusion is that the Newtonian blood model is a reasonably good approximation for transient blood flow simulation.

Numerical method

The present study, are motivated by the quest to understand the dynamics of flow downstream of narrowed bypass section. In healthy vessels in generally we have a laminar flow, but in the narrowed vessel can lead to relatively high-Reynolds numbers and disturbed flow, leading to transition or turbulence. A large number of experimental studies [27 - 29] and computational studies of the hemodynamics in diseased arteries [30, 31, 65] exhibit disordered and turbulent flows in such vessels. Turbulence can significantly affect the pressure and shear stress downstream of the stenosis [33].

Simulations have been carried out over a range of Reynolds numbers (based on the centreline temporally averaged stream wise velocity and the bypass radius) from 215 to 620. The maximum Reynolds number during the cycle was about 600, which is a characteristic of patient in a resting condition. The k-ε turbulent model used in present simulation are capable to predict low Reynolds number transitional flows inside tot the narrowed bypass graft.

The k–ε model is used to solve the time dependent Navier-Stokes equations for an incompressible blood flow. The numerical simulation is perform using the commercial CFD

FLUENT 6.3 package [26], parallelized across eight 3.2 GHz Intel processors of a TYANPSC T-650 Rx (Tyan Computer Corporation, Taiwan, parallel computing machine with sixteen 3.2 GHz processors). The velocity profile at the inlet section is identical to the real coronary ostium velocity profile [33] (Figure 2.17). The governing equations are solved iteratively until convergence of all flow variables is achieved. The convergence criterion was set to $1x10^{-5}$ for the residuals of the continuity equation and of *X, Y* and *Z* momentum equations.

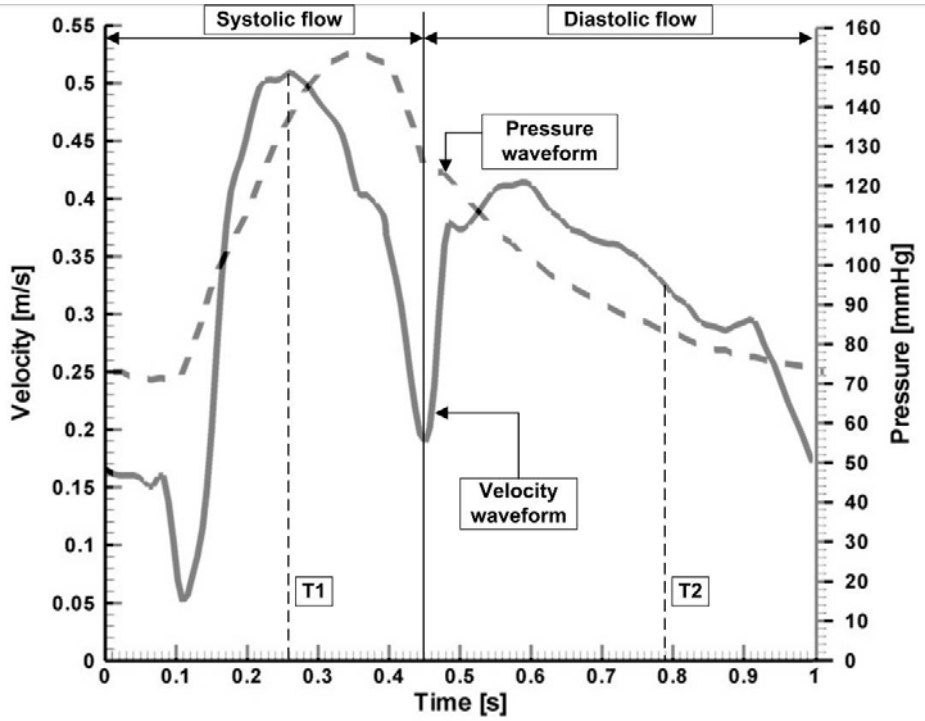

Figure 2.17. Pulsatile inlet flow, which is the physiologically realistic case, based on flow and pressure waveforms acquired with an intravascular ultrasound Doppler probe in the RCA [33]. Velocity input waveform and pressure output waveform. T1 and T2 different investigation times (T1=0.26 s peak systole, T2=0.79 s diastole).

TECPLOT (Tecplot, Inc, Bellevue, WA) software (Version 10.0) was used for the visualization of flow patterns, and for quantification of velocity field, WSS and wall pressure, in different sites of the bypass graft.

Pressure distribution

The pressure distributions along the axial direction in the investigated saphenous vein graft are shown in Figures 2.18 and 2.19.

Overall pressure drop increase with flow rate (at the peak systole, Figure 2.18). Values of the overall pressure drop increased from 2.6 mmHg at the time T6 to 4.4 mmHg at the time T2 (Figure 2.20).

In order to investigate de pressure drop along the vein graft we define several graft segment: Bs1 = bypass vessel segment between section D0 – D3, Bs2 = bypass vessel segment between section D3 – D6, Bs3 = bypass vessel segment between section D6 – D13.

At the time T2, pressure drop in the segment Bs1 (corresponding to the first tortuous graft segment) increase from 1.25 mmHg to 2.81 mmHg (Figure 2.20).

In this study, the wall pressure decreased towards the periphery of the saphenous vein graft with elevated pressure drops in the first tortuous segment. The increased pressure drop in this part of the graft reflects the elevated energy needed to drive the flow through these regions.

The wall pressure dropped inside the vein graft as blood flow velocity increased (Law of Bernoulli). In the post-tortuous segments, the wall pressure continued to gradually drop towards the most distal segments.

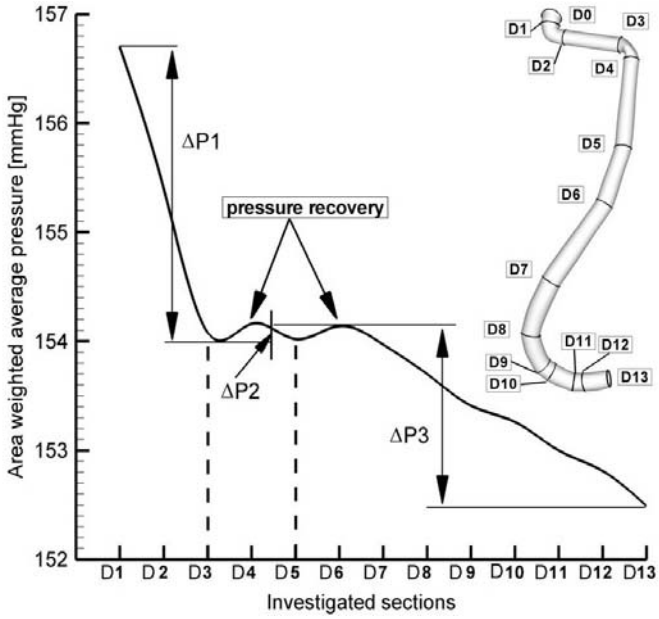

Figure 2.18. Pressure drop in narrowed venous bypass graft at the time T1 (peak systole, corresponding to the Figure 8). D0 = inlet section, D13 = outlet section.

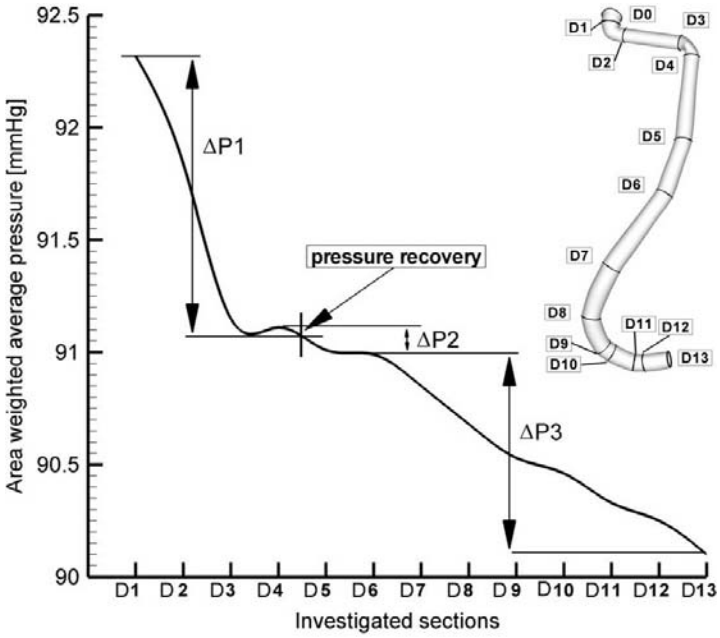

Figure 2.19. Pressure drop in narrowed venous bypass graft at the time T2 (diastole, corresponding to the Figure 8). D0 = inlet section (proximal anastomosis), D13 = outlet section (distal end-to-side anastomosis).

Energy loss associated with such flow expansion after each constriction will be large and consequently the pressure drop will be higher [Figures 2.21 and 2.22].

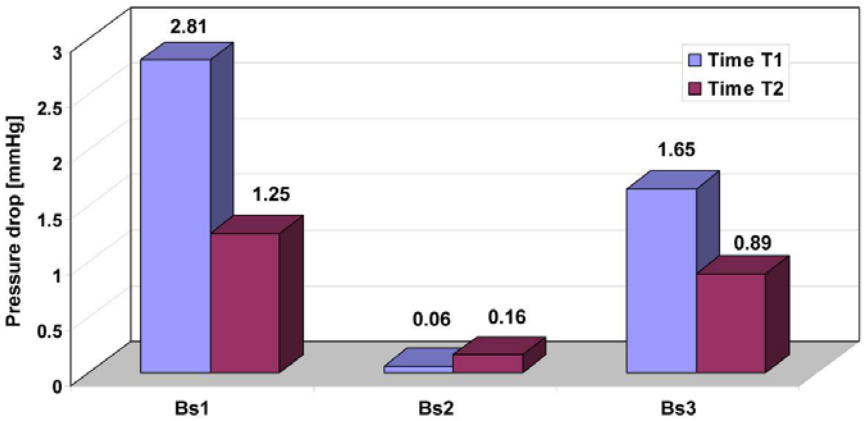

Figure 2.20. Pressure drop for different time step in the investigated bypass graft. Time T1 and T2 correspond to the time steps indicated in Figure 2.17. Bs1 = bypass vessel segment between section D0 – D3, Bs2 = bypass vessel segment between section D3 – D6, Bs3 = bypass vessel segment between section D6 – D13.

Flow separation and secondary flow

Disturbed flow patterns are initiated by a change in the geometry of the graft through which the blood flows. The velocity profiles over the systolic period are presented in Figures 2.21 and 2.22 in terms of flow pattern, direction, distribution magnitude, and location of the recirculation zone.

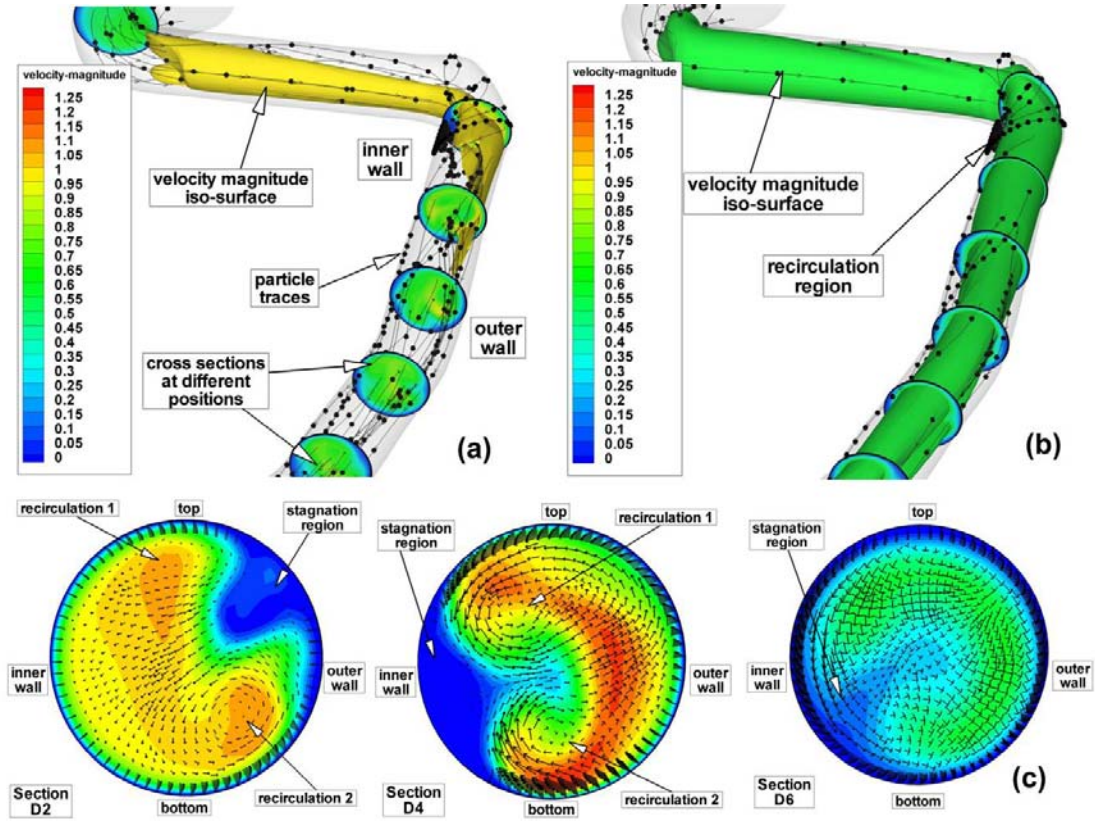

Figure 2.21. Disturbed flow indicators and streamlines inside of the narrowed venous bypass graft at the peak systole T1=0.26 s. (a) iso-velocity contours for velocity magnitude of 1m/s; (b) iso-velocity contours for velocity magnitude of 0.6 m/s; (c) cross-sectional transient velocity contour and vector fields corresponding to the section D2 , D4 and D6.

The flow regime is presented by the velocity vectors, velocity contours, and streamlines on the different cross sections and along the bypass graft (Figures 2.21 and 2.22).

The flow separation regions can be seen clearly from the instantaneous velocity vector panels (which are illustrated in Figures 2.21 and 2.22) and streamlines at the different time steps. One can observe the pattern of velocity vector distinctively showing the recirculation zones with the formation of the eddy at the downstream of each constriction.

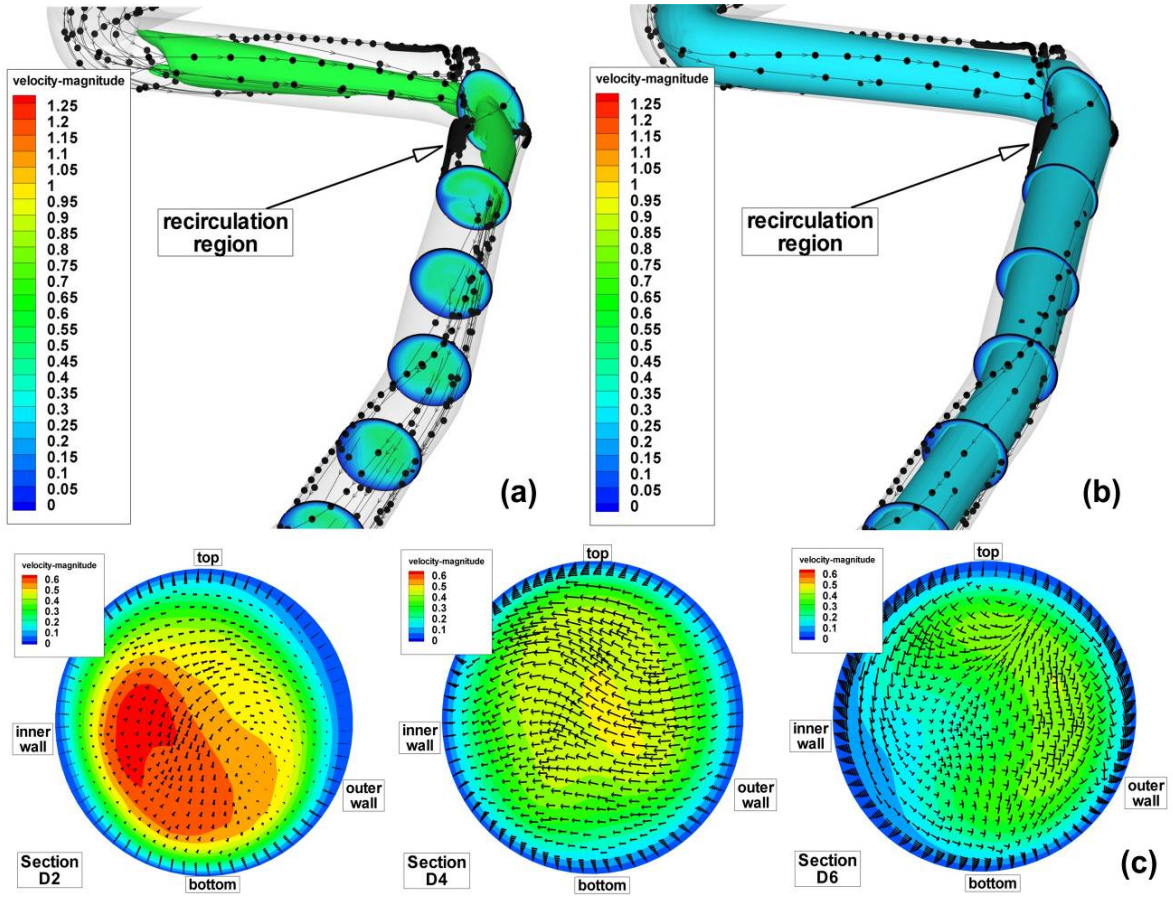

Figure 2.22. Disturbed flow indicators and streamlines inside of the narrowed venous bypass graft at the time T2=0.7 s. (a) iso-velocity contours for velocity magnitude of 0.6 m/s; (b) iso-velocity contours for velocity magnitude of 0.3 m/s; (c) cross-sectional transient velocity contour and vector fields corresponding to the section D2, D4 and D6. No recirculation regions found in the investigated cross sections. Recirculation regions are present distal to the Bs2 vessel segment, near the inner wall where low velocity flow is developed (Figures a and b).

From Figures 2.21 and 2.22 can be observed that the exists a separation in flow field namely the flow divides into two regimes one of which is the recirculation region distal to each constriction, and the other is the main flow field carrying the bulk of the flow near the centre of the graft.

During the acceleration phase of the flow a particularly interesting flow field characteristic develops at the peak systole, namely two co-rotating vortices appear (clearly see in Figure 2.21c).

As the flow begins to decelerate, the vortex attached to the inner side of the graft wall, distal of the segment Bs2, and increase in size (the length of the recirculation zone).

Secondary flows subtract energy from the forward axial flow motion. Thus their location and extent can affect severely the fluid dynamic performances of the saphenous vein graft.

The instantaneous velocity field are shown in Figure 2.21 at time T1 (peak systole) and Figure 2.22 at the time T2. The recirculation region is non-symmetric and the maximum velocity in the Bs2 segment is around 1.1 m/s at the time T2.

The correct prediction of the vortex dynamics are important in order to estimate the near-wall residence times for blood particles. It is particularly relevant because it is now widely accepted that biological processes initiating atherosclerosis are strongly influenced by a combination of fluid and mechanical factors [69, 70].

Particle trajectories

At the time t = 0s, a large number of particles (1063 particles) are distributed inside the flow field (the particles is released from the centre of each cells of the inlet section mesh – the number of elements per inlet section is 1063).

Figure 2.23 represents the paths of fluid particles released in the inlet region at the specified point in space and time during the peak systole (T1=0.26 s).

Also, Figure 2.23 shows a decrease in particles count at the vessel segment Bs1 and Bs2 and increases in the distal regions of the vein graft (vessel segment Bs3), during both investigated time steps.

As expected, some released particle entrained in the vortex developed in vessel segment Bs2 distal to the severe narrowing and remain there (Figure 2.24).

For example, particles from the vessel segment Bs2 during the decelerating portion of the flow will tend to be washed downstream as the segment Bs2 pushes them out into the core of the flow. Particles leaving the constricted region (segment Bs2) during the accelerating phase will tend to become entrained in the vortices and remain there.

It has been shown that particles starting in the central part of the inlet section are transported to the core of the flow distal to the segment Bs1 and Bs2 from distal anastomosis (Figures 2.23, 2.24 and 2.25).

During the accelerating systolic phase, particles move downstream toward the segment Bs1 with a helical motion, driven by the horseshoe vertical motion of the fluid (Figure 2.24b). At this time, very high speed fluid flow moves toward in vein graft and some particles impact immediately the wall both in vessel segment Bs1 and Bs2 and distal in segment Bs3 (Figure 2.24 a, b and Figure 2.25 a and b).

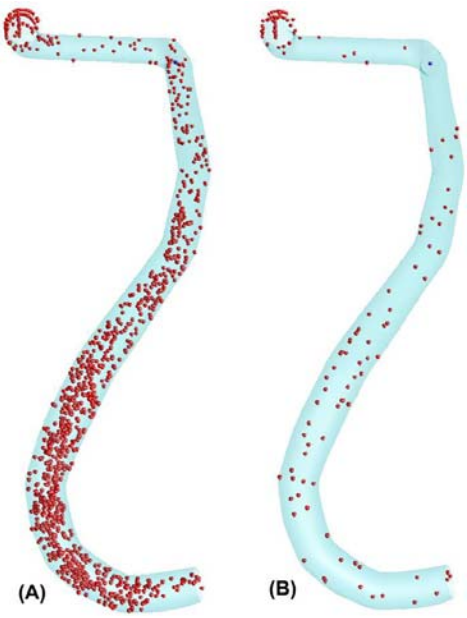

Figure 2.23. Time evolution of particle transport in the narrowed saphenous vein graft at the two critical time levels during to the cardiac cycle. a) Time T1=0.26s, b) time T2=0.79s.

It has been shown particles released in the inlet section following the fluid flow, move downstream in the vein graft, arrive at the first constriction (segment Bs1) and follow the spiral fluid motion in section Bs2 (Figures 2.24b and 2.25b).

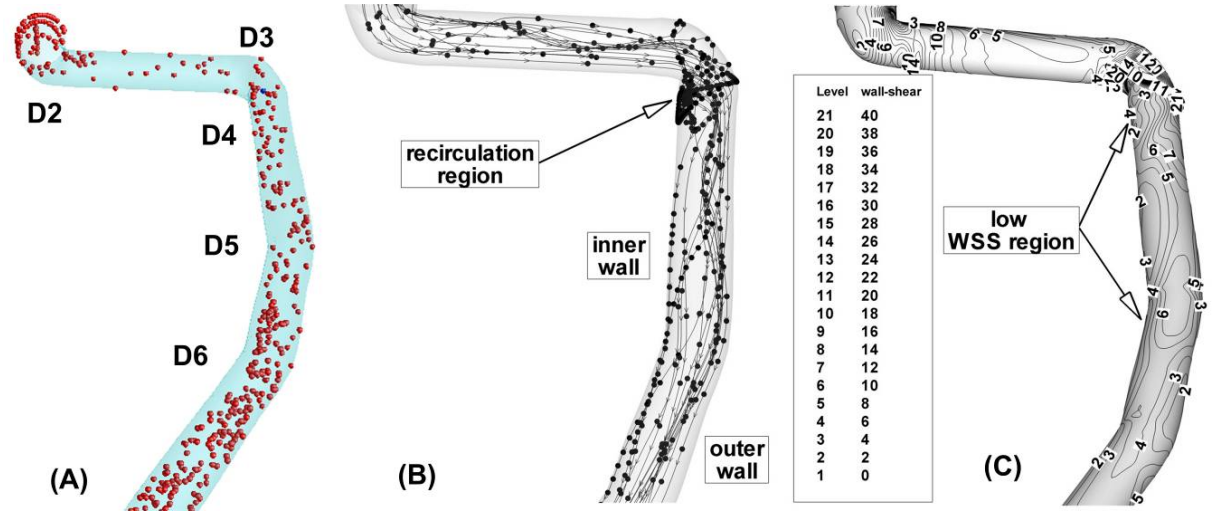

Figure 2.24. Particle distribution along the narrowed vein graft at the time T1=0.26s. a) Instantaneous plot of the particle distributions in the proximal part of the vein graft. b) streamlines of the entire flow field at the time T2. Particles follow the spiral fluid motion in vein segment Bs2. c) temporal WSS magnitude contours along the vein graft wall. In vessel segment Bs2 particles are exposed to the high shear environment in the tortuous region (WSS value is in [Pa]).

In Figures 2.24 and 2.25, wall shear stress plots display a snapshot of the entire flow field at an instant in time and particle trace (the history of a particular fluid element through a region). Plots in Figures 2.24 and 2.25 represents the paths of fluid particles released in the inlet region at the beginning of the cardiac cycle, and the particle depositions at the different time steps of the cardiac cycle.

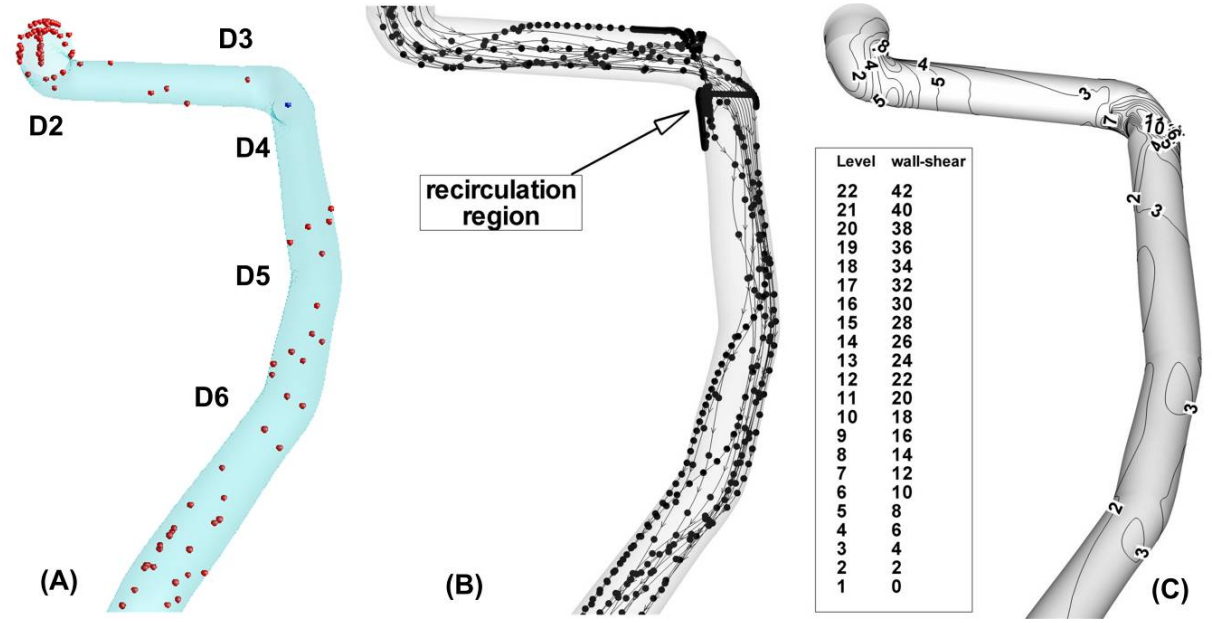

Figure 2.25. Particle distribution along the narrowed vein graft at the time T2=0.79s. a) Instantaneous plot of the particle distributions in the proximal part of the vein graft. b) streamlines of the entire flow field at the time T2. c) temporal WSS magnitude contours along the vein graft wall (WSS value are in [Pa]).

It would also appear that the particle residence time increase significantly due to the severe constriction (segment Bs2), (Figures 2.24 and 2.25).

Wall Shear Stress and Intimal Thickening

Distal to the vessel segment Bs2, the areas of low wall shear stress are associated with flow separation in the inner wall, and with flow disturbance and wall shear stress fluctuation on the outer wall (Figures 2.24 and 2.25). This may be important because it has been suggested that the fluctuation of the wall shear stress or disturbed flow leads to increased endothelial cell turnover and intimal thickening.

If the blood flow is increased, that increase wall shear stress, an adaptive increase in arterial luminal size is observed. If the blood flow is decreased, that decreases the wall shear stress, there is an adaptive decrease in arterial lumen size. This decrease in luminal size elevates the wall shear stress, and the decrease in lumen continues until the wall shear stress is returned to normal [41].

In Figure 2.26, the wall shear stress distribution shows a close reflection of the outline of the narrowed vein graft. The maximum shear stress occurs at the narrowest cross-section vessel segment Bs1 (between section D1 and D2) and vessel segment Bs2 (between section D3 and D4). There is a rapid increase in wall shear stress, then after the critical value of the narrowed sections the wall shear stress decreases. The maximum value of wall shear stress is located in the segment Bs2, along the outer wall.

Figures 2.24c and 2.26b shows wall shear stress (WSS) distributions at the time T1=0.26s, the time where the flow is at a maximum (peak systole). The range of WSS in this figure varies from 2 to 42 Pa. Two intense high WSS regions appear in both narrowed graft segment (Bs1 and Bs2). For the each this regions the WSS is approximately 40 Pa. One the opposite side of this regions we have the large regions of moderate (Figure 2.26a between segment Bs1 and Bs2) and low WSS (WSS varies from 14 to 18 Pa for the moderate zone at the time T2, and from 4 to 8 Pa at the time T6).

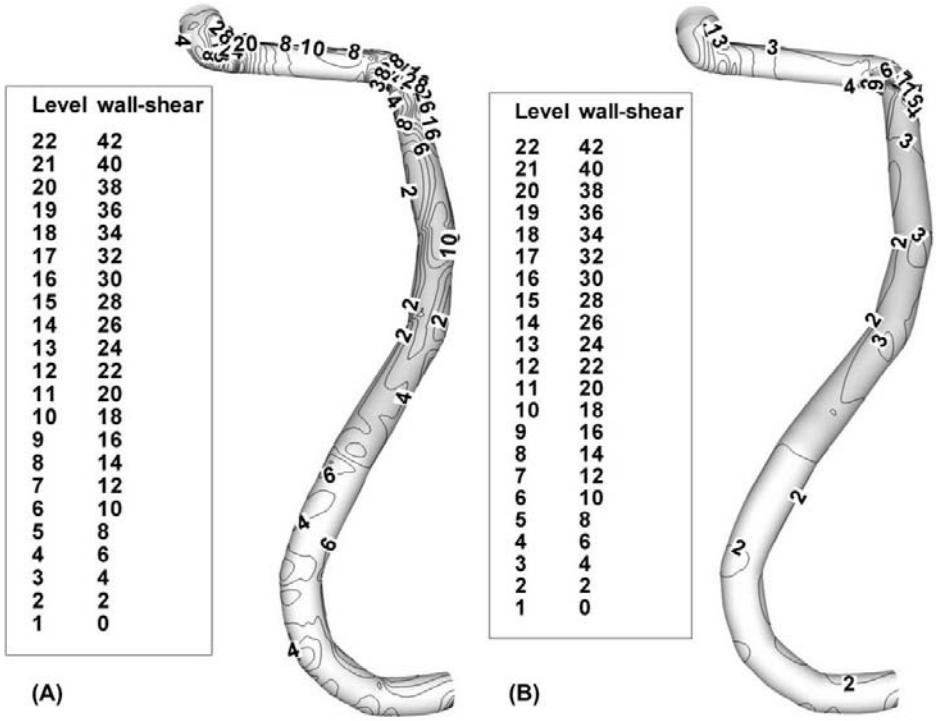

Figure 2.26. Wall shear stress distributions at the two critical time steps. a) time T1=0.26s peak systole, b) time T2=0.79s decelerating phase of the diastole (WSS in [Pa]).

At the peak velocity (T2) in the regions of the segment Bs2 the WSS reach the value of 42 Pa. At this section, the maximum WSS is increasing dramatically with the increase of area reduction. One diameter downstream the WSS is low because of formation of the recirculation zone.

As the flow decelerates the regions a high WSS begin to dissipate and more regions of moderate and low WSS begin to appear (time T2, figure 2.26b).

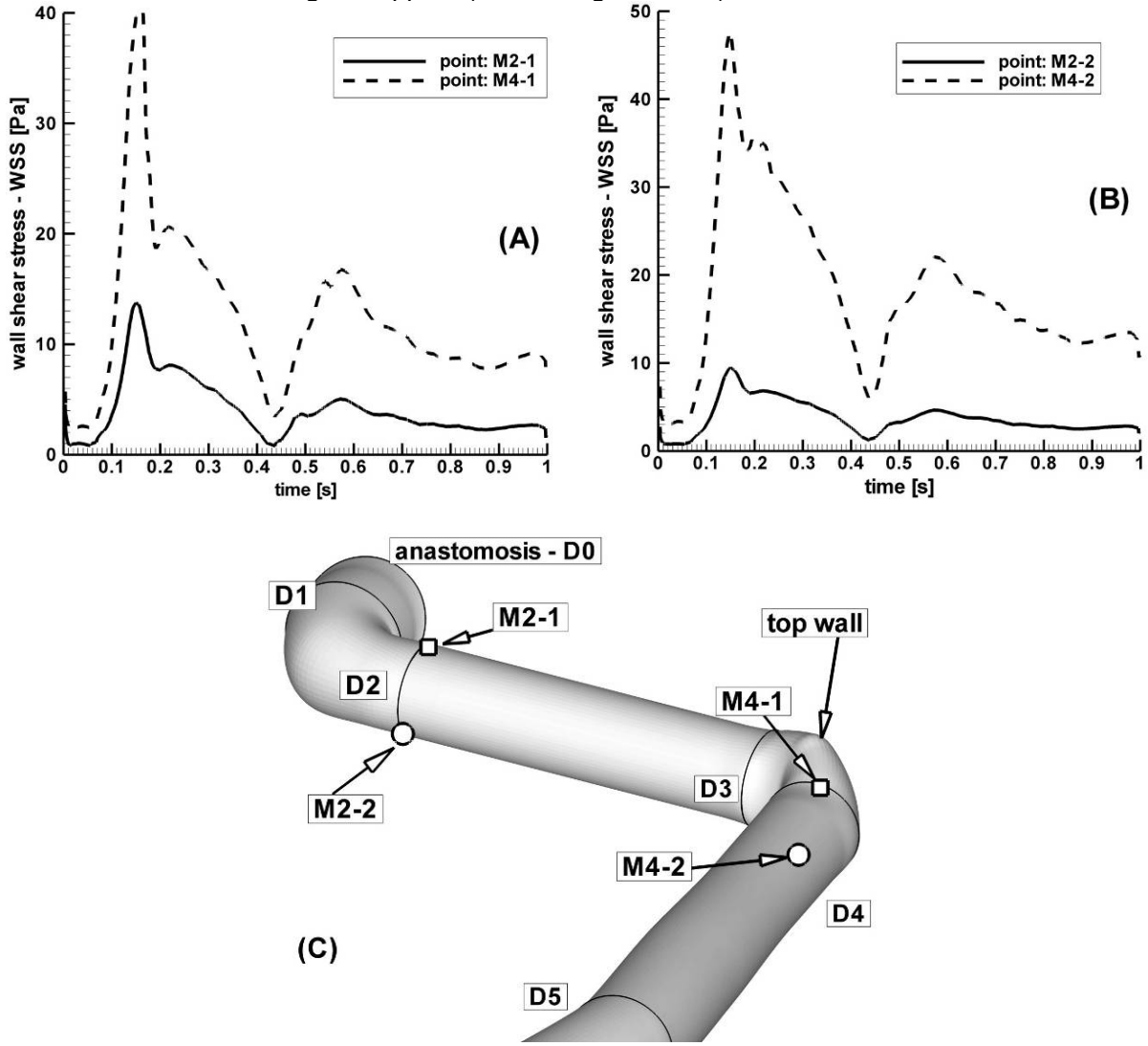

Figure 2.27. WSS time evolution during the cardiac cycle. (a) top wall marker: M2-1 and M4-1 top point in section D2 and D4 respectively; bottom wall marker: M2-2 and M4-2 point in section D2 and D4 respectively; (c) point position in the section D2 and D4.

From investigation by Fry [71], WSS was found to have immediate influence on the endothelial histology and a 40 Pa shear stress is able to damage endothelial cells. Our study shows that the peak WSS reached 42 Pa at the throat of the narrowed graft sections which is enough to damage the endothelial cells.

As shown in narrowed vein graft, regions of flow acceleration are associated with high WSS (Figure 2.27).

Comparing hemodynamic changes throughout a cardiac cycle between the narrowed sections and normal vessel segment we can conclude that the vein graft wall contains more regions with low WSS value.

Caro et al. [72], suggests that low WSS areas significantly change the endothelium biological response. Lieber and Giddens [73] investigated the post-stenotic core flow behaviour in pulsatile flow and found that the critical WSS for the development of intimal hyperplasia (IH) is less than

1.5Pa. The importance of low WSS area in graft failure in a saphenous vein and a varicose saphenous vein has been estimated computationally by Goubergrits et al. [74].

Evidently, low WSS values are associated with low local velocities and, thus, long residence times of fluid in the near-wall region.

Clinical implication

Between 3% and 12% of saphenous vein grafts occlude, with or without symptoms, within the first month after bypass surgery [75].

Evidently vein graft implantation is an injury that occurs simultaneous to the transposition of the conduit of the saphenous vein into an altered hemodynamic environment. In response to the damage, a series of repair events occur in a time framing ranging from hours to months.

Imposed hemodynamics modulates each process in a unique manner. Effect of the altered shear stress during the initial hours to days after graft placement is more different from the influence of the WSS evolution would have much later in the adaptation process. This temporal dependence between the local hemodynamic environment and the response of the vascular wall define basically that the vein graft failed or not.

A lot of work in cardiac and peripheral vascular flow has indicated that type of a spiral or helical flow pattern exists both in the heart and in the large and medium-sized arteries [76 - 78]. Stonebridge and Brophy [79], hypothesized that spiral laminar flow pattern could exert a beneficial effect on the mechanisms of endothelial damage or repair. Caro et al. [80] supported this hypothesis and demonstrated that spiral flow may lead to relative uniformity of wall shear and inhibition of flow stagnation, separation, and instability.

Spiral flow has also been shown to increase the blood velocity near the vessel wall and wall shear rate. Spiral flow pattern reduce acute thrombus formation and intimal hyperplasia, thereby potentially improving graft patency [81].

According to our flow simulation, velocity near the graft wall and the wall shear rate are greatly enhanced in narrowed sections. We believe that the enhanced blood velocity near the vessel wall and the wall shear rate can impede the staying and adherence of leucocytes to the surface of the graft, reducing the possibility of thrombosis formation due to the spiral flow developed in the proximal part of the vein graft, but promote the cells adherence in distal part of the graft.

Conclusions regarding to the flow in narrowed aorto-coronary bypass graft

The dynamics of the flow in narrowed saphenous bypass graft are studied through the velocity, streamline, pressure drop, wall shear stress and particle depositions in the present investigations.

Maximum wall shear stress reaches a level at which endothelial damage in tortuous portion of the narrowed graft, which is regarded as being clinically significant from the graft patency point of view.

The scientific literature indicates that the endothelium is easily penetrated by the leukocytes and proteins with the prolonged residence time due to vortex formation in the flow separation region.

For normal vascular functioning, maintenance of laminar shear stress within the physiologic range is essential [82, 83]. The magnitude and direction of wall shear stress influence inflammatory processes in the vessels.

After graft surgery some vein grafts will become stable and some unstable leading to vein graft failure. The reason why some vein grafts are stable and some are unstable is currently unknown.

The study provides awareness that the presence of the torsion along the graft shape influences the hemodynamic parameters (velocity, pressure, particle residence time).

We conclude that the helical flow induced by vessel torsion may stabilize the blood flow in the distal part of the SVG, reducing the flow disturbance and suppressing the flow separation. In

addition, the helical flow may also play a role in suppressing severe polarization of LDLs, therefore protecting them from thrombosis and atherogenesis.

In the other hand, distal to the tortuous vein segment, in the distal end part of the graft, the high particles concentration can promote the inflammatory processes in the vessel. More, in the distal anastomosis where end-to-side arrangement exist the disturbed flow pattern can affect the wall shear stress magnitude and create favourable conditions for developing the intimal hyperplasia. Intimal hyperplasia is the major disease process in venous grafts between 1 month and 1 year after implantation [84].

Pathology studies have described an increase in SVG intima area days to weeks after implantation [85]. In our investigation, is evident that the major cause of the saphenous vein graft (SVG) remodelling is due to the changes in hemodynamic conditions.

In conclusion hemodynamic changes together to the increase in SVG intima area can produce graft remodelling in the first 7 days after implantation.

C). Identification and visualization of the vortices in arterial bypass graft flow

Problem description

Curved channel flows and branching of fluid flow are used in many industrial applications to provide compactness and high heat and mass-transfer rates so as to enhance mixing in laminar flow regimes. Branchings of fluid flow are extremely common throughout the human body and involve various complex geometrical configurations and flow conditions associated with different ranges of Reynolds numbers, pulsatility and wall flexibility. Branching greatly affect the fluid dynamics and are common sites of disease in human cardiac circulation.

The flow in curved and branching channels is characterized by a secondary flow in the form of a pair of counter-rotating symmetrical vortices in the pipe cross section, these corner vortices are called end cells or Eckman vortices by Finlay and Nandakumar [86] and they are a consequence of the pipe wall curvature. Their existence was shown analytically for the first time by Dean [87] in tubes of circular cross section. The commonly used control parameter for a flow in a curved duct is the Dean number, De, defined as:

$$De = \frac{U_m D_h}{\nu}\sqrt{\frac{D_h}{R_C}}, \tag{2.1}$$

where, U_m is the axial mean velocity, v is the kinematic viscosity, D_h is the hydraulic diameter and R_c is the mean radius of curvature. The Dean number is therefore the product of the Reynolds number (based on axial mean velocity U_m through a pipe of hydraulic diameter D_h) and the square root of the curvature ratio. Note that the hydraulic diameter is defined a

$$D_h = \frac{4(cross\ \ section\ \ area)}{wetted\ \ perimeter}, \tag{2.2}$$

Dean vortices are the result of centrifugal forces. They are present in a variety of practical applications including technological and physical problems: internal turbine blades, cooling passages, biological systems, ducting in internal combustion engines and heat exchangers. The first mathematical analysis made by Dean [87] shows the onset of a pair of counter-rotating vortex cells in a Newtonian fluid flow in a curved channel resulting from the interaction between centrifugal and viscous forces. The Dean number represents a ratio of the centrifugal forces to the viscous forces, and measures the intensity of the secondary flows.

The effects of vortices or vortical structures are particularly evident when considering both flow stability, and the processes of mixing and transport by the flow [32, 88, 89].

This paper presents a series of numerical simulations intended to determine whether the use of commercially available computational fluid dynamics (CFD) software may provide a viable alternative to the use of physical models for predicting the occurrence of vortices and vortical structures in branching pipe.

The objective of this paper is to examine the dynamics both of vortex motion and of particle transport in application of the branching vessels, namely in the by-pass graft, and to relate these to parameters such as geometry, unsteadiness and the mixing processes by the flow.

Numerical approch

Graft geometry

The authors have used simplified geometry (Figure 2.27) for the by-pass graft model with graft angles of 30°, 45°, and 60° for the analysis of the flow and WSSs around the graft junction,

and across the bed of the host tube. The internal diameter for the graft was taken to be D=25.4 mm with a graft–tube diameter ratio of 1:1 (Figures 2.28 and 2.29).

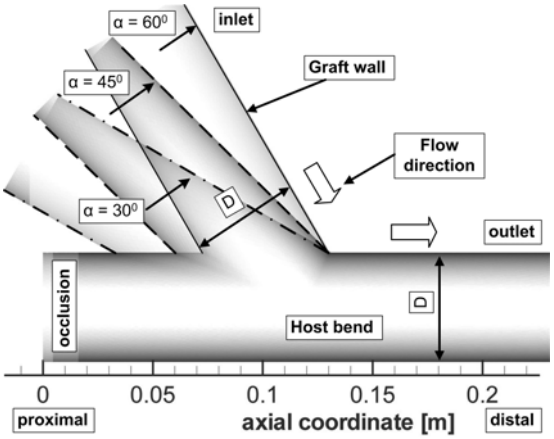

Figure 2.28. By-pass graft geometry along the longitudinale plane for three graft angles (30°, 45° and 60°).

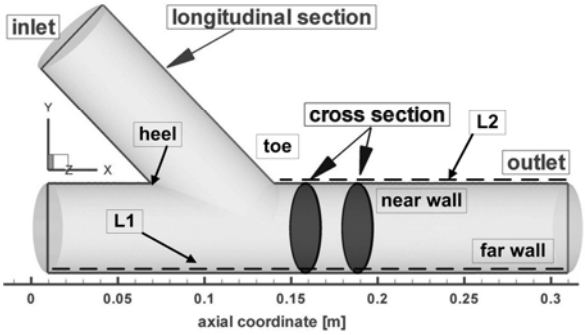

Figure 2.29. Different section used for hydrodynamic parameters investigation.

Assumptions

To simplify the analysis, fluid was assumed to be a homogeneous, incompressible and Newtonian. The simulations were carried out under steady flow condition, which is somewhat different from the pulsatile flow in vivo, but the results can still shed some light on the hydrodynamic performance of the grafts.

The steady, three-dimensional equations from the conservation of mass and momentum for an incompressible Newtonian fluid, form the basis of the numerical formulations for the flow analysis in a branching pipe.

The key assumptions for the numerical simulation of the flow are: steady state flow, flow is laminar, gravitational effects are negligible, and physical properties remain constant.

Governing equations

The flow can be described through the conservation laws, i.e. the conservation of mass, momentum and energy. As a reference the momentum equation in its general form (Eg. 2.3) is given in tensor notation and in Cartesian coordinates.

$$\underbrace{\underbrace{\underbrace{\frac{\partial}{\partial t}(\rho u_i)}_{\text{unstadeady acceleration}} + \underbrace{u_j \frac{\partial}{\partial x_j}(\rho u_i)}_{\text{convective acceleration}}}_{\text{Inertia}} = \underbrace{\frac{\partial \tau_{ij}}{\partial x_j} - \frac{\partial p}{\partial x_i}}_{\text{divergence stress}} + \underbrace{\rho f_i}_{\text{other force}}}, \tag{2.3}$$

where p is the pressure, τ_{ij} the viscous shear stress tensor which is definned as:

$$\tau_{ij} = \underbrace{\mu\left(\frac{\partial u_i}{\partial x_j} + \frac{\partial u_j}{\partial x_i}\right)}_{\text{viscous shear stress}} - \mu \frac{2}{3} \delta_{ij} \frac{\partial u_k}{\partial x_k}, \tag{2.4}$$

The ratio of the inertia forces and the viscous forces acting on the fluid can be expressed in terms of non-dimensional Reynolds number:

$$\mathrm{Re} = \frac{inertial \quad force}{viscous \quad force} = \frac{U \cdot D}{\nu}, \tag{2.5}$$

with ρ [kg/m^3] denoting the fluid density, U [m/s] the caracteristic velocity, D [m] diameter of the pipe, μ [Pa.s] the dynamic viscosity and v [m^2/s] the kinematic viscosity.

Results

Boundary layer separation is a well known phenomenon associated with sudden changes in surface geometry. The free shear layer resulting from a flow separation is likely to contain pressure, velocity and consequently local shear fluctuations which could be felt at the wall at the points of separation and of reattachment [90]. Also, the separation bubble itself, though, in general a vortex that is slower moving than the shear layer or the main flow, constitutes an area in which the wall could experience flow conditions different from those in other areas [91].

By-pass with 45^0 graft angle

In the occluded region of the 45 degrees by-pass model a vortical structure is evident when the recirculation is sufficiently strong to distinguish the particle motion from the rotational action of the boundary layers (Figure 2.30). When we increase the branch angle, however, the impact of the particles is sufficiently strong to generate a vortical structure not only in the occluded region but also at the sides of the junction leading to the looping structures.

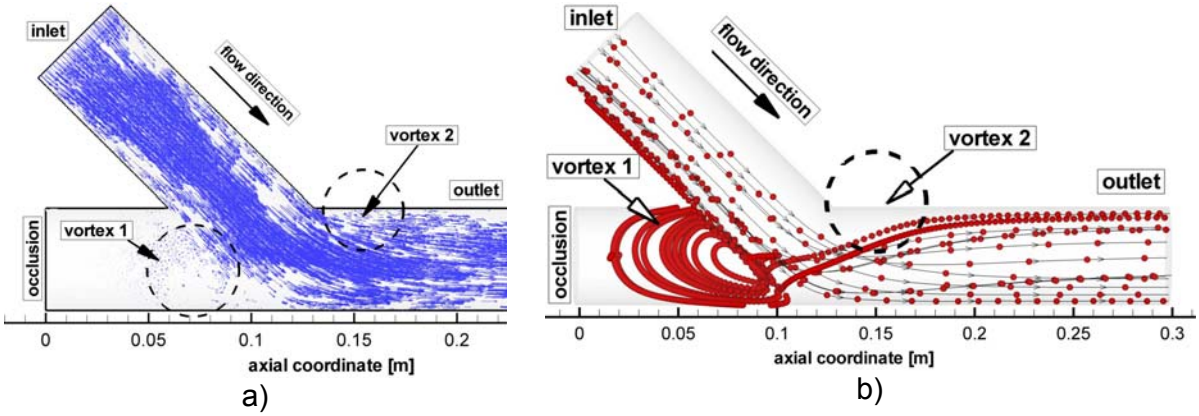

Figure 2.30. a) Velocity vectors along the longitudinale plane. Flowfields are shown for the 45° graft angle. b) Three-dimensional view of the pathline of the high inertia fluid under steady flow conditions at Re = 500 showing development of the double helix.

Particle pathlines and streamlines coincide exactly for the case of steady laminar flow however they may differ greatly in the case of transient flow. Most of this has to do with their respective nature; streamlines display a snapshot of the entire flow field at an instant in time, whereas particle pathlines trace the history of a particular fluid element through a region.

Just downstream of the toe, at X = 0.15 m, the axial velocity profile was skewed toward the far wall, and flow separation was observed along the near wall (Figure 2.30). The trace at X = 0.15 m, clearly displayed the presence of secondary flow, which consisted of low inertia fluid swirling circumferentially around the vessel towards the near wall and the high inertia fluid from the core region being forced toward the far wall. Once the high inertia fluid approaches the far wall, it too travels circumferentially in a spiraling manner because of the centrifugal force generated by the change in flow direction (Figure 2.30b).

Thus, at X = 0.18 m some of the high inertia fluid continued to move along the far wall while the remainder traveled around the vessel circumferentially in a double helical manner as shown in figures 2.30 and 2.31. For Re = 500, it appeared that the spiraling motion of the fluid created a high shear layer (a possible source of flow instability), (Figure 2.31) that resulted in the formation of a small vortex just downstream of the toe of the anastomosis (Figure 2.30). In other words, a small vortex was found to be embedded in the spiraling flow that consists of a main vortical motion superimposed on the axial flow.

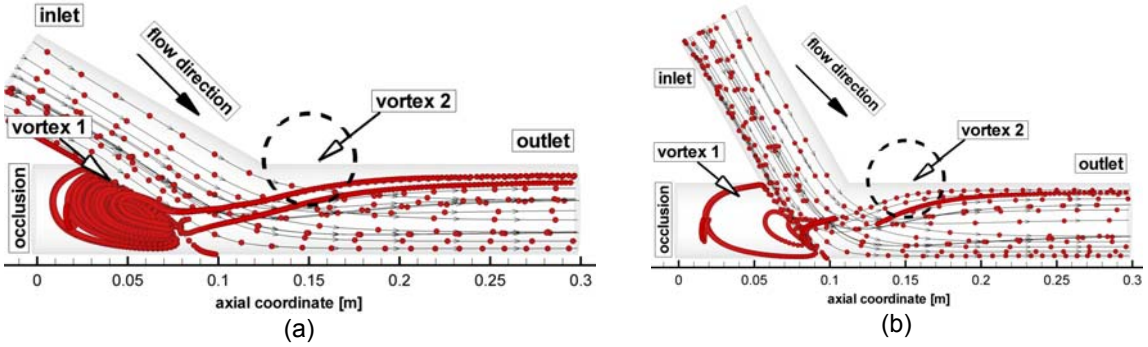

Figure 2.31. Three-dimensional view of the pathline under steady flow conditions at Re = 500 showing development of the secondary flow. a) Bypass with 30° graft angle. b). Bypass with 60° graft angle.

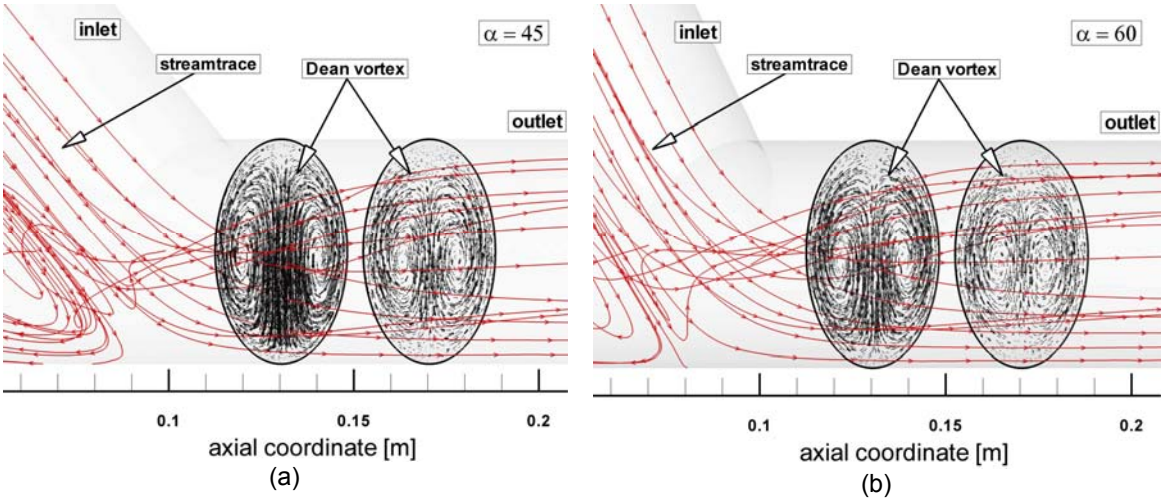

Figure 2.32. Dean vortices development in distal part of the host artery. a) Bypass with 45° graft angle. b). Bypass with 60° graft angle.

The vortices in the occluded arterial section became smaller and appeared to have a greater angular velocity for graft angle of 30° comparatively to the bypass with graft angle 45° and 60°. It was also observed that particles were shed periodically from the primary and secondary vortex into the graft. Many of the features shown here illustrate the significant three-dimensional flow structures that exist at physiological Reynolds numbers and, as such, may have important implications for analytical and numerical predictions of flow at the anastomosis.

In the anastomosis domain, a strong region of recirculation is observed near the occluded end of the artery, which forces the flow to move into the perfused right coronary (distal) artery as indicated in Figures 2.29, 2.30 and 2.31. The flow in the perfused distal artery exhibits significant skewing of the velocity profiles towards the inner wall of the perfused artery, as seen in Figure 2.32.

Helicity

Figure 2.33 shows the area-weighted average helicity of the flow at twelve cross-sections of the each investigated by-pass grafts (between X=0.15 m and X=0.3 m), which can be used to compare the efficiency of the grafts in creating swirling flow. Helicity *H* and the area-weighted average of helicity *H* (*average*) were defined by the following equation:

$$H = \left(\nabla \times \vec{u}\right) \cdot \vec{u}\,, \tag{2.6}$$

As evident from the figure, for all grafts, the helicity have a maximum degree at cross-setion 1 (at X=0.15 m), then starts to decrease gradually until cross-section 12 (at X=0.3 m).

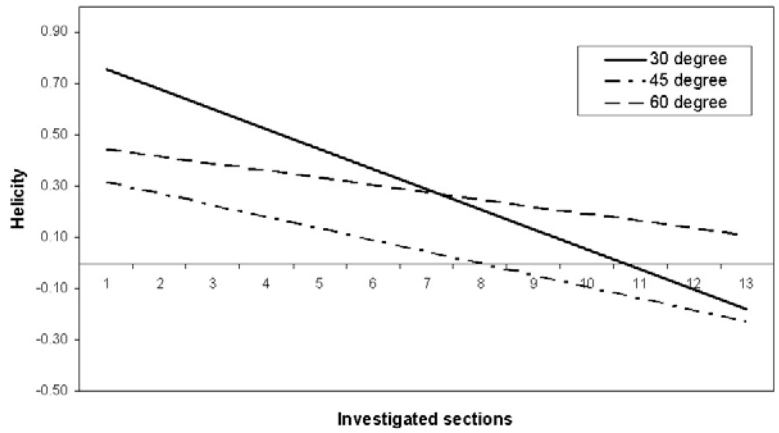

Figure 2.33. Helicity evolution at the twelve cross-sections (between x=0.15 m and x=0.3 m, Figure 2.28) of the by-pass graft for al investigate junction angles. Helicity are normalized by the mean helicity in the outlet section.

The vorticity generation is proportional to the angular velocity vector of rotation, is influenced by circulation and stirring effects on fluid [92, 93]. In principle, mixing of fluids is a complex physical process that ais governed by a convection–diffusion equation. However, in this study, mixing is simply regarded as stirring flow.

Fluid particles are mixed and make wide paths due to the combined effects of axial velocity and axial vorticity such as can be encountered when stirring coffee to melt sugar quickly.

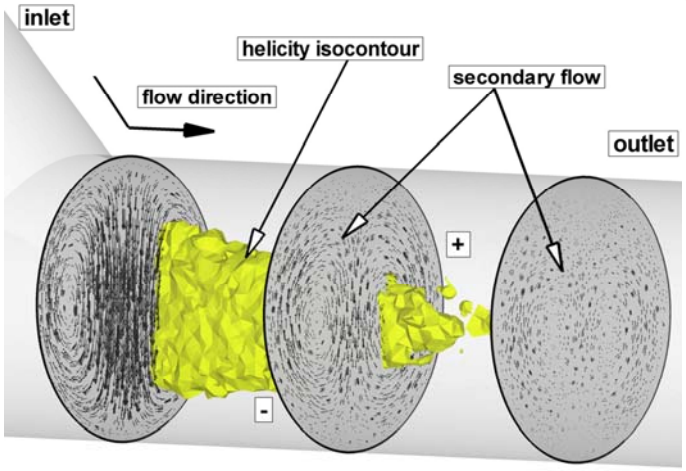

Figure 2.34. Secondary flow evolutions along the host bend distal to the toe in 45^0 by-pass geometry. Helicity iso-contour for helicity value of He = 2. Dean pair vortex: + clock wise direction, - anti-clock wise direction.

We carried out flow visualizations under the same conditions in the all investigated by-pass graft (with 30°, 45° and 60° by-pass angles) for Reynolds number (Re = 500). The results are shown in figure 2.35. The evolutions of the Dean cells are almost identical to those in the investigated cross-section at X= 0.18 m, but significat differ in each investigated graft angles.

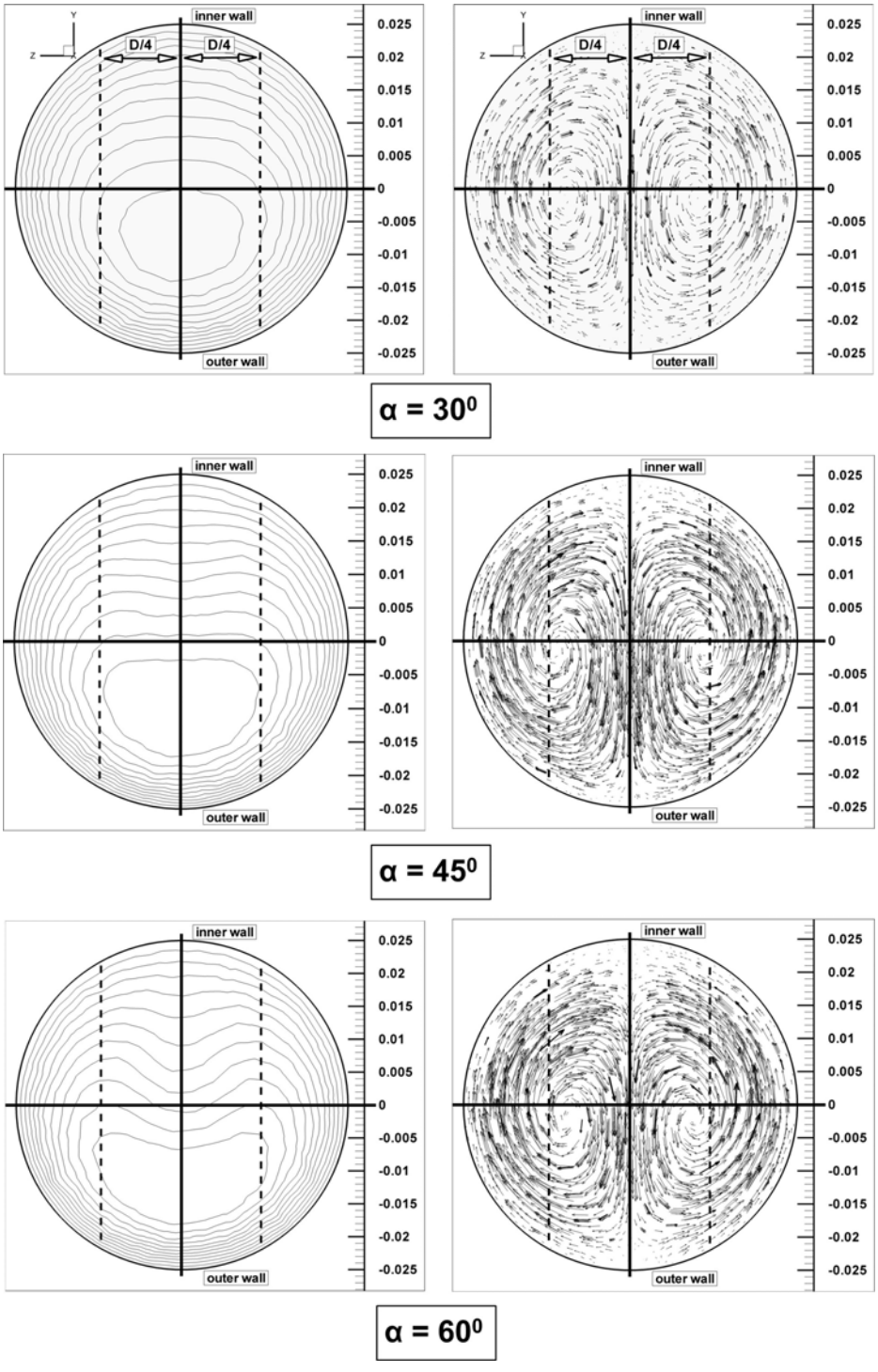

Figure 2.35. Flow visualization showing secondary flow for different by-pass angles for same corss-section x = 0.18 m (Figure 2.29); a) axial velocity left; (b) secondary velocity vector right. Dean vortex center evolution for different by-pass angles.

For the Reynolds number studied here (Re = 500), we observed a secondary flow structure consisting of two counter-rotating cells along the whole geometry (Figures 2.34 and 2.35).

The areas where low axial wall shear stress was observed included: (1) the near wall just beyond the toe of the junction, (2) the proximal region of the host vessel where an almost stagnant zone was seen, and (3) the stagnation point on the bed of the host vessel where the entry flow is split into the forward and retrograde flows (Figure 2.36). Since the secondary flow caused by the centrifugal force is expected to be strongly dependent on the angle of the graft, this geometric factor will influence the spatial and temporal variations of the velocity field.

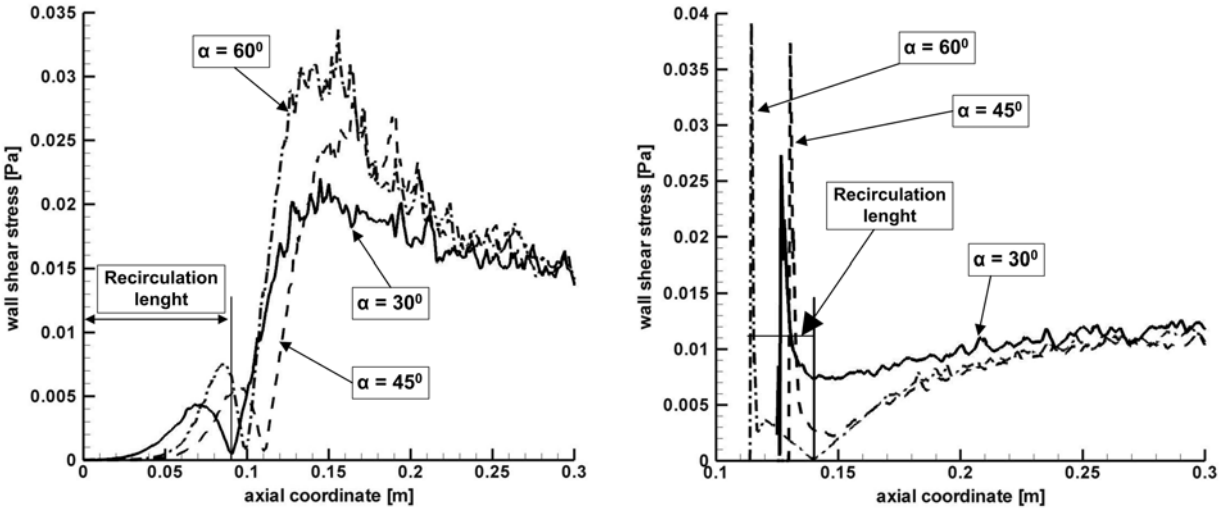

Figure 2.36. Wall shear stress – WSS and recirculation length evolution for different by-pass angles; (a) WSS evolution along line L1 (far wall, Fig. 2.28); (b) WSS evolution along line L2 (near wall, Fig. 2.28).

Conclusions regarding vortex visualisation in arterial bypass graft flow

The most significant secondary flow features comprise the generation of Dean vortices in the distal host, a flow recirculation within an occluded host vessel and Dean vortex generation in the proximal host for bilateral host flows. The study has indicated that the dominant geometric effects on secondary flow arise through the branch angle and flow split both of which can cause flow separation opposite to the floor.

The increased angles also caused a flow separation at the toe region of the graft just proximal to the junction which is a potential site of the high particles residence time.

D). Experimental investigation of the bypass graft flow

It is accepted that hemodynamics analysis is imperative in the design of coronary bypass grafts [93]. In the last years, graft design has been an objective of much research to find of correlations between hemodynamics and graft failure [94, 95]. Researchers have been trying various ways in order to improve the hemodynamic performance of the implanted grafts. Numerical studies and in vitro investigations have confirmed that the graft flow patterns are strongly dependent on the local geometry [96].

Compared with traditional planar grafts, the non-planar graft configurations improve hemodynamic environments including promoted flow mixing and reduced stagnation flow regions, but also increased host artery vessels injury [97-100]. Caro et al. [94] carried out animal research on small amplitude helical technology (SMAHT) conduits and numerically simulated the steady flow in a four-turn helical graft. Morbiducci et al. [101] investigated the existence of a relationship between helical structure and vascular wall indices of atherogenesis in aorto-coronary by-pass models. Zheng et al. [102] numerically simulated both the steady flows and unsteady flows in helical grafts [103]. Preliminary studies [104–106] suggested that the helical type flow appeared promising in preventing intimal hyperplasia (IH) and thrombosis but increased the pressure drop compared with a conventional graft [106].

Traditional flow parameters such as the stagnation point, recirculation length were calculated for the comparison. Pressure drops along both graft type (straight and helical), which is important to graft patency, were investigated in detail.

Methods

Encouraged by the findings of the previous research [34, 95, 100, 109] a steady and unsteady flow in an helical type by-pass graft was experimentally investigated namely, in straight and two-turns helical grafts.

In order to compare the disadvantages and the advantages of the suggested helical type by-pass graft model over a conventional by-pass graft configuration, three experimental models are designed and evaluated:

(i) the conventional straight graft configuration, shown in Figure 2.37,
(ii) two-turns helical-type graft (Figure 2.38),
(iii) four-turns helical-type graft (not presented in this paper).

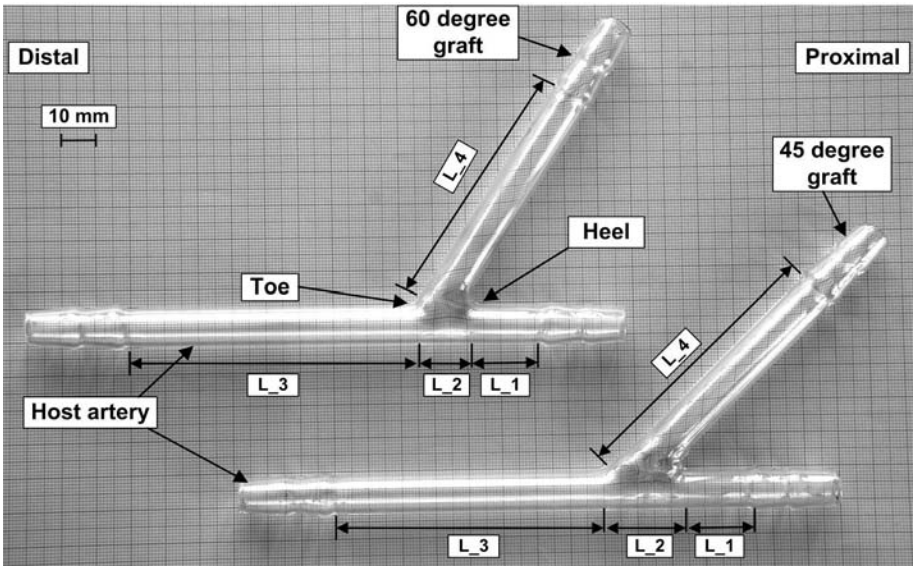

Figure 2.37. Experimental bypass models used for flow visualizations. Model was manufactured from glass tubing with a constant internal diameter of 8 mm (for both models).

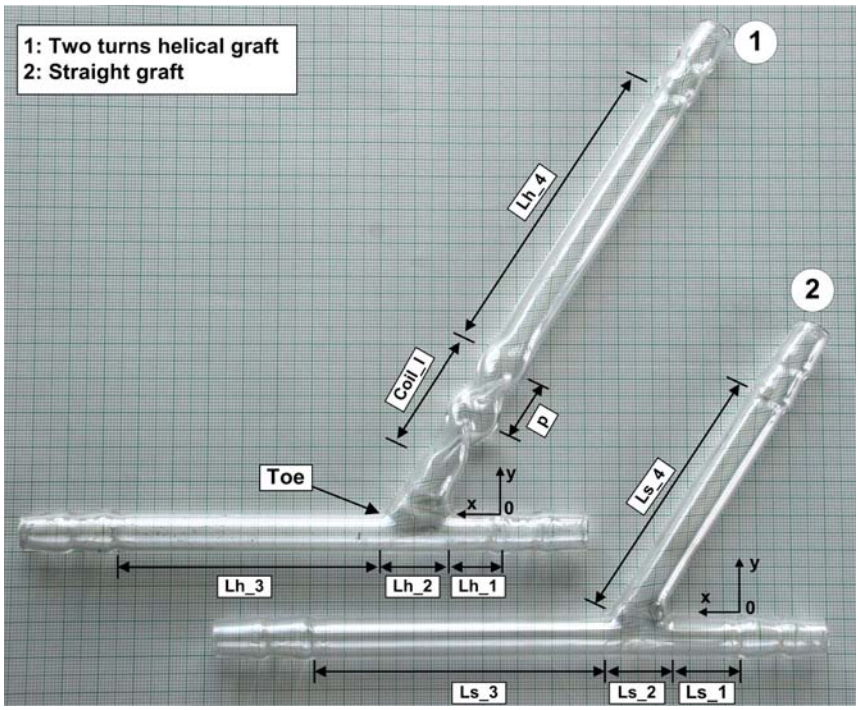

Figure 2.38 Experimental bypass models manufactured from glass tubing with constant internal diameter of 8 mm. Helical and straight type model.

Graft geometry

The experimental test sections were manufactured from glass tubing with constant internal diameter of 8mm, fashioned into a right shape with an approximately 80 mm in length segment, both in proximal and distal direction from the graft anastomosis (Figure 3). The models are considered to have an anastomotic angle of 45° and 60° with the proximal segment of the coronary artery fully occluded. The models are designed to be planar. The geometric dimensions of the bypass models are given in Table 2.7.

Table 2.7. Investigated bypass parameters (all parameters is given in mm).

Parameters	L_1 [mm]	L_2 [mm]	L_3 [mm]	L_4 [mm]
45-degree graft	20	25	80	80
60-degree graft	20	15	85	85

The geometric shape of the aorto-coronary bypass graft is shows in Figure 2.38, and the geometric dimensions of the aorto-coronary bypass models are given in Table 2.8. The artery model is assumed to be a tapered straight vessel with proximal total occlusion. The graft angle (θ) is selected as a parameter and is set to be 60^0. Characteristic parameters of a two-turns helical tube are internal diameter of D=8 mm, pitch of coil p=20mm (2,5xD), coil length Coil_l = (Figure 2.38), coil diameter of 9mm.

Table 2.8. Bypass parameters (all parameters is given in mm).

Parameters	Ls_1/Lh_1 [mm]	Ls_2/Lh_2 [mm]	Ls_3/Lh_3 [mm]	Ls_4/Lh_4 [mm]
Straight bypass	15	20	80	80
Two-turns helical bypass	15	20	80	80

Experimental setup

Assembled experimental system provide the model with the desired working conditions. A schematic of this system is presented in Figure 2.39. A glycerin–water mixture of 60% glycerine and 40% water by weight was selected of working fluid.

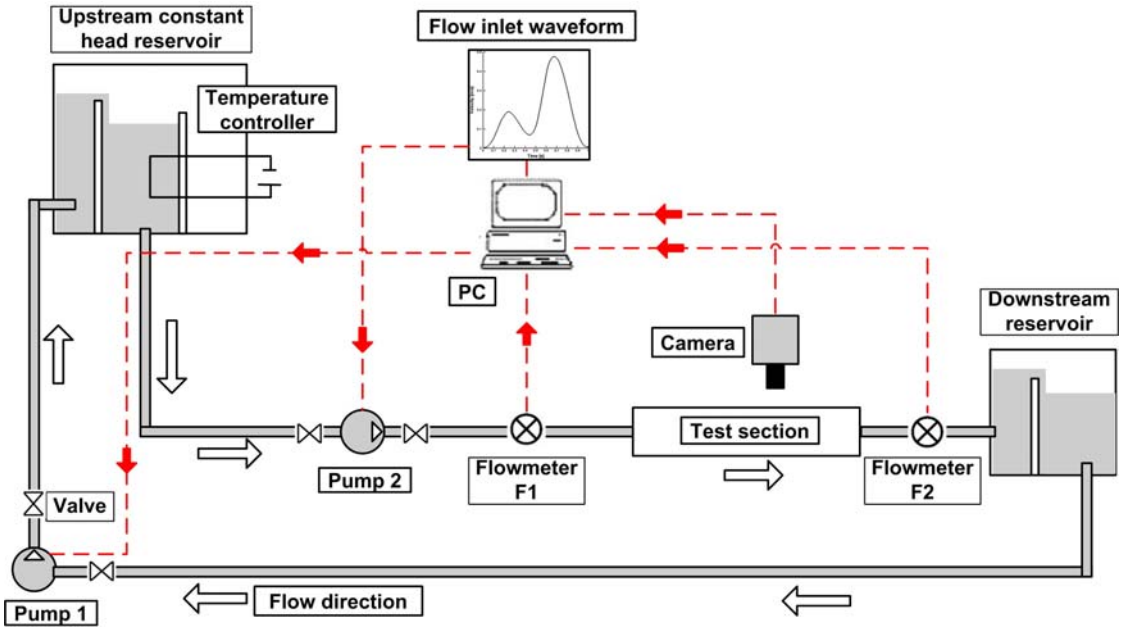

Figure 2.39. Experimental setup used for straight and helical type graft investigations. Steady and pulsatile waveform used in experimental investigation for velocity input signal.

Flow experiment performed under physiological conditions [100]. The mean flow velocity is 0.144 m/s. The mean Reynolds number, is Re=260 (based on graft diameter and blood viscosity). The maximum Reynolds number during the cycle is 612. Assuming a heart rate of 60 beats per minute, the period of each cycle is 1s.

The experimental graft models were manufactured from glass tubing with the internal diameter of D=8 mm, fashioned into a straight shape and helical configuration with an approximately 80 mm straight segment proximally and 80 mm distally (Figures 2.37 and 2.38).

The flow system consisted of a constant storage head tank; test section; floating ball flow meter; collecting tank; and variable speed centrifugal pump. A computer-controlled pump was used to generate the inlet flow waveform. The amplitude of flow fluctuation introduced by the pump was a function of the difference between the upstream and downstream flow resistances. The amplitude of flow fluctuation could be set (by changing the resistance) by adjusting the valves upstream and downstream of the test section (Figure 2.39). During the experimental measurements, the waveform at the flow meter F2 was identical to the generated waveform (flow meter F1) with no phase shift.

The mean flow rate (upstream of the test section) was measured by a metric size 10 rotameter with a stainless steel float (flow meter F1 in Figure 2.39). The rotameter leg served the extra purpose of prevent-ing air from travelling upstream from the flow outlet. A blood analog fluid was prepared having dynamic viscosity (μ) of 0.00408 Pa.s and a density (ρ) of 1050 kg/m3. The flow visualization study was performed using the injection of a bolus of ink into flowing fluid at a different Reynolds numbers.

In the first phase of the study, unsteady flow in the model was obtained using a computer-controlled pump at a variety of flow rates, leading to Reynolds numbers (based on mean inlet velocity and tube diameter) of 280 to 950 (Figure 2.40). Both in experimental setup and in numerical simulations the unsteady flow model was used.

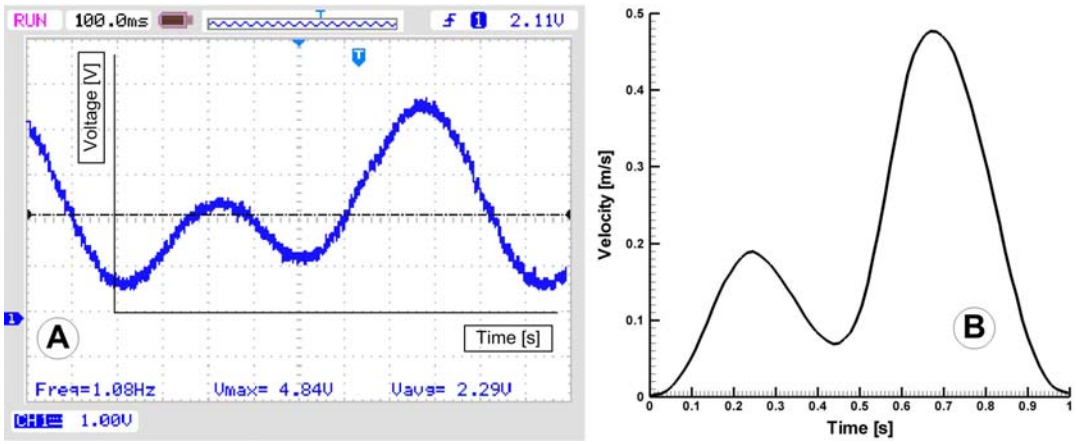

Fig. 2.40. Pulsatile inlet flow condition. A) Pulsatile wave used in experimental investigation. B) Pulsatile wave used for numerical simulations.

Results

Experimental flow visualization in straight graft

To quantify the effect of the bypass geometry, all experiments were carried out under the same flow condition for both investigated graft angle 45° and 60° respectively. The flow field for steady flow (Re = 298) condition in both models is shown in Figure 2.41.

Both investigated models are considered to have the proximal segment of the coronary artery fully occluded. The models are designed to be planar, based on the study presented in the literature [98, 111] who demonstrated that the course of the right coronary artery bypass graft can be assumed to be approximately planar.

Both geometries show the presence of the primary vortex (Vortex 1) in the proximal part of the host artery between stagnation point and heel (Figure 2.41). In the occluded arterial section, the primary vortex became unstable and split into two separate vortices. The primary vortex that is the larger vortex (Vortex 1 in both cases) closes to the anastomosis, rotated anti-clockwise as viewed in the photograph, whereas the second vortex close to the occluded part rotated clockwise (Vortex 2 in Figure 2.41 for both cases).

The character of complex vortex structures created in the area between the heel and occluded part depends on the flow parameters. These vortices shape is strongly dependent on the occlusion distance from the anastomosis.

In Figure 2.41 the proximal vortices (vortex 1 in both cases) illustrates the greater exchange of fluid that occurred between the occluded arterial section and the graft. These vortex structures increase due to the contact between the main flow and the graft surface.

The flow distal to the stagnation point moves in the form of a helically shaped vortex structure with variable spiral angle (Figure 2.41 A and B). These structures create secondary flow in the cross section [100, 112]. The secondary flow intensity decreases downstream, and gradually, the velocity profile have a laminar velocity profile. In this region, we have a strong velocity gradient etween the main flow and the vortex structure (Figure 2.41).

In Figure 2.41 for both cases, the presence of the recirculation regions increase the contact between fluid flow and the anastomosis surface and, therefore, increased the risk of development of the IH and thrombosis.

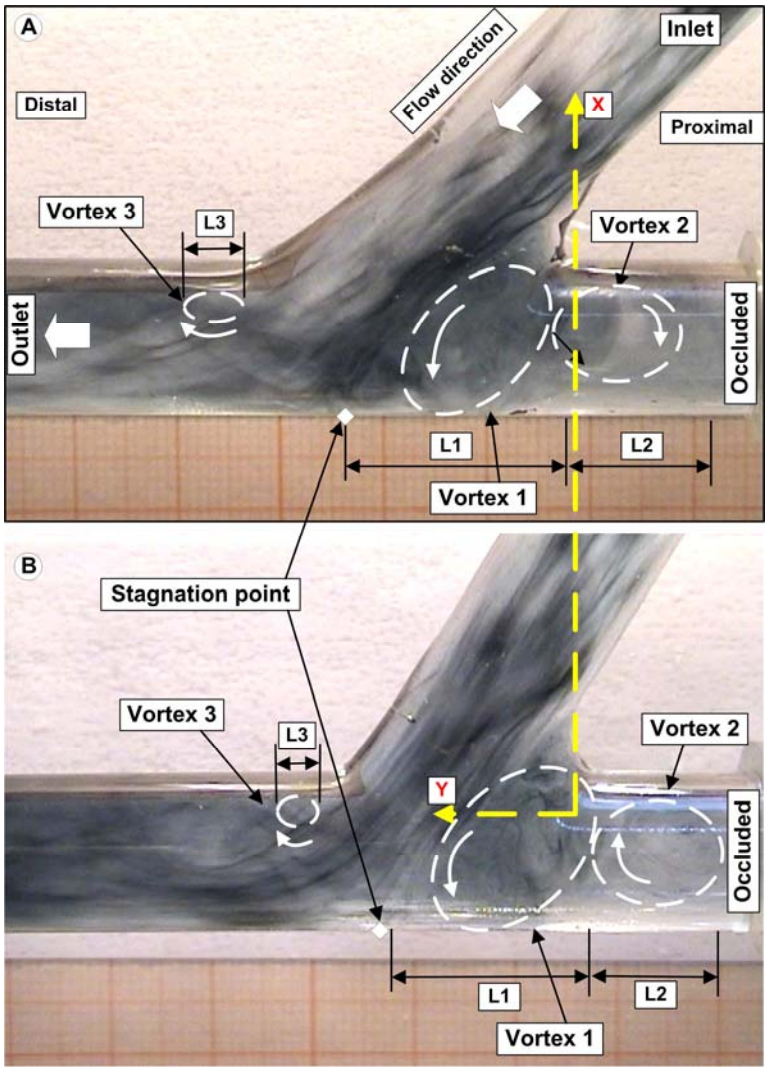

Figure 2.41. Experimental steady-state flow visualization: (A) Bypass angle of 45°; (B) Bypass angle of 60°. For the same working conditions both geometry present the same flow structure namely two significant recirculation regions and one vortex with a short length of the recirculation in the vicinity of the toe (Vortex3).

Comparison between numerical and experimental flow visualization

Figures 2.42 present a detailed comparison of experimentally measured velocity patterns for straight graft and numerically obtained flow field for the same geometry. Comparison between numerically computed and experimentally measured flow patterns shows a good agreement. The agreement on the symmetry plane is good, with the minor exception that the experimental measurements predict a slightly larger recirculation zone than was predicted by numerical simulation (Table 2.9).

Of interest are particles that stay in a recirculation zone (anastomosis region) or can be in contact with the bypass wall (Figure 2.41). As it can be seen in Figure 2.41 the interaction between the primary vortex (vortex 1) and the core flow induces particle transport from the elevated concentrations (inside to the vortex 1) into the core of the flow.

Table 2.9. Flow characteristics for the investigated bypass geometries

Nr.	D [mm]	Q [ml/min]	V [m/s]	Re [-]	L1 [mm] numeric	L1 [mm] expe	L2 [mm] numeric	L2 [mm] expe	L3 [mm] numeric	L3 [mm] expe	By-pass angle
1	8	407	0.144	298	14	19	13	13	3	3	60°
2	8	407	0.144	298	16	21	10	10	1	1.5	45°

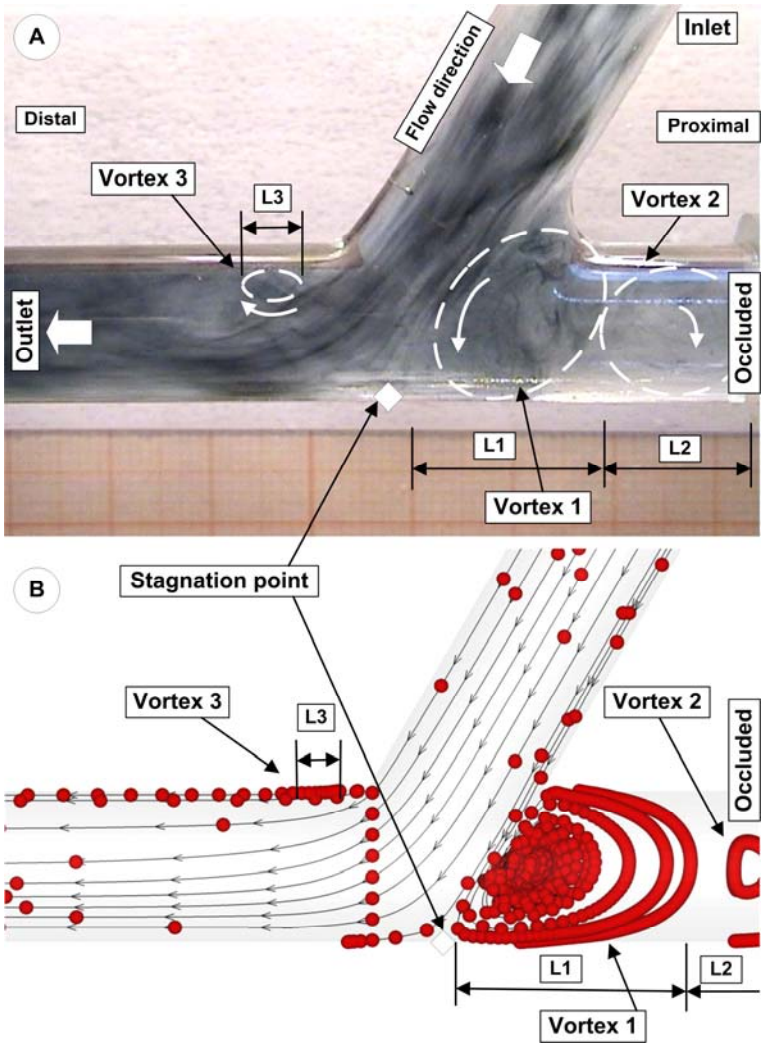

Figure 2.42. Comparison between flow patterns: (A) experimental measurements and (B) particle path-lines obtained using numerical simulation (path-lines are the trajectories that individual fluid particle follow). Both flow patterns demonstrated the presence of the secondary flow in the proximal part of the bypass graft in vicinity to the heel. Spontaneous disturbances near to the toe fade distally in the distal part of the bypass. Flow investigations correspond to the bypass angle of 60-degree and Reynolds number of 298.

Both type of analysis, experimental and numerical simulation indicated that bypass anastomosis is characterized by abnormal flow conditions. The abnormal flow field is characterized by flow separation at the toe, strong flow impact on the host artery floor and flow oscillation at the heel.

The presence of a slow recirculation flow (vortex 1) increases the near-wall residence time and also increase particle deposition. The presented findings are in agreement with literature data

where this zone are identified at the region prone to thrombus formation [113] and intimal hyperplasia (IH) development [114, 115].

Also, the flow impact on the host artery floor is known to be a contributing factor to the graft failure. Figure 9 clearly shows the evidence of change in the flow character once it impacts the anastomosis floor. In both investigated bypass geometries at the toe, we identify high wall shear stress (WSS) associated with a flow separation region proximal to the toe (Figures 2.41 and 2.42).

Based on experimental data and numerical results, the following general features of the velocity field can conclude:

- From the graft tube, a high-momentum fluid enters at the junction and travels towards a stagnation point on the bed of the host pipe. In the neighborhood of this stagnation point, the flow splits into forward and retrograde components having large near-wall velocities.
- The proximal portion of the host vessel shows counter-rotating vortices on the symmetry plane for both investigated bypass angle (Figure 2.41).
- In the downstream section of the host vessel, strong secondary flows are present. The magnitude of the secondary flows increases with increasing the bypass graft angle (Figure 2.42).

Experimental flow visualization in the helical and straight bypass graft

Investigated bypass graft configurations is supposed to benefit the flow field in different ways including uniform, smooth flow in the anastomotic region, less impact on the artery bed and less or even no vortex at the heel region of the anastomosis [34].

Coronary artery bypass graft (CABG), deal with several type of complications such as thrombosis and stenosis. Literature showed that, after vascular surgery, the flow field may play a modulating role. In this case intimal hyperplasia (IH) mainly located in regions of the low wall shear stress and high residence time [98, 107, 116]. For this situation helical flow tends to reduce these unfavorable hemodynamic conditions [101, 117, 118].

In order to focus on the effect of the by-pass geometry, all experiments were carried out under the same flow condition and graft angle.

Steady flow in the 60 deg straight and two-turns helical model is shown in Figure 2.41 for Re=298. Both geometries show the presence of the primary vortex in the proximal part of the host artery. The 60 degree model was particularly susceptible to particle deposition at the toe of the graft, and may therefore be more susceptible to thrombosis (vortex V3 zone for straight graft and vortex V1 for two-turns helical graft shown in Figures 2.41A and B).

Note the presence of the vortice in the distal artery (Figure 2.41A, vortex V2) and strong helical flow in the by-pass graft (Figure 2.41B). The primary vortex, that is the larger vortex (vortex V1 in both cases) closes to the anastomosis, rotated anti-clockwise as viewed in the photograph, whereas the more distal secondary vortex rotated clockwise (vortex V2 in Figure 2.41A).

The character of complex vortex structures created in the area between the heel and occluded section depends on the flow parameters. We can identify two vortices in the symmetry plane (vortex V1 and V3 in Figure 2.41A). The shape of these vortices is strongly dependent on the occlusion distance from the anastomosis.

The flow outside the symmetry plane moves in the form of a helical shaped vortex structure with variable spiral angle (Figure 2.41A). These structures create secondary flow in the cross section [100]. The secondary flow intensity decreases downstream and the velocity profile is gradually formed into developed laminar velocity profile [34]. There is an area with strong velocity gradient between the main flow and the vortex structure (Figure 2.41A).

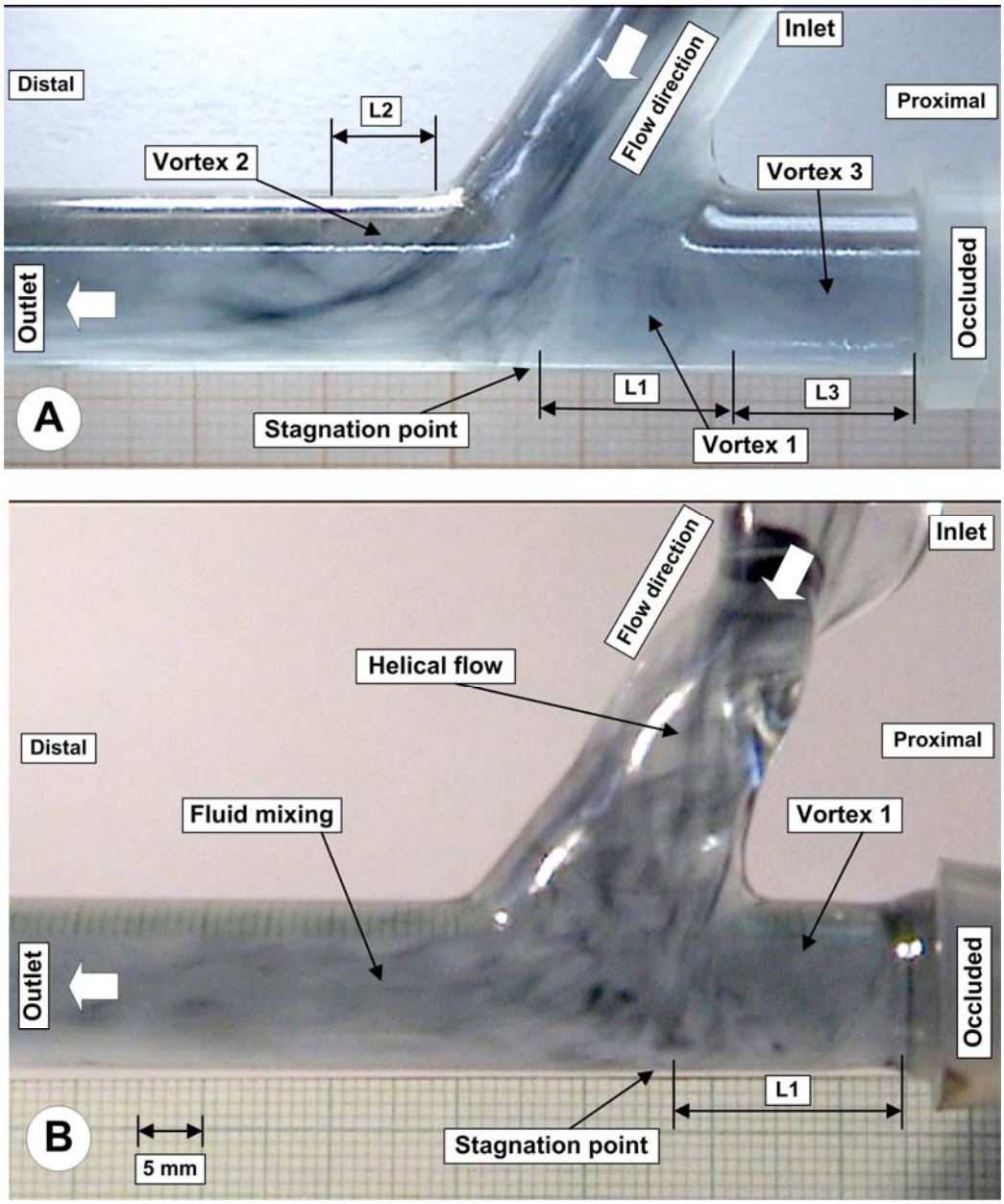

Figure 2.41. A) Flow pattern in straight bypass graft demonstrating secondary flow. Spontaneous periodic disturbances in the distal part of the host artery; B) Flow pattern in two-turns helical type bypass graft. Note that in this case only one vortex is generated.

The size and position of this area is time-dependent for the unsteady inlet conditions. In this area the magnitude of WSS is maximal due to the large velocity gradients. Maximum WSS is time-dependent and shifts along the x axis (Figure 2.38) downstream and upstream that causes wall shear stress oscillation.

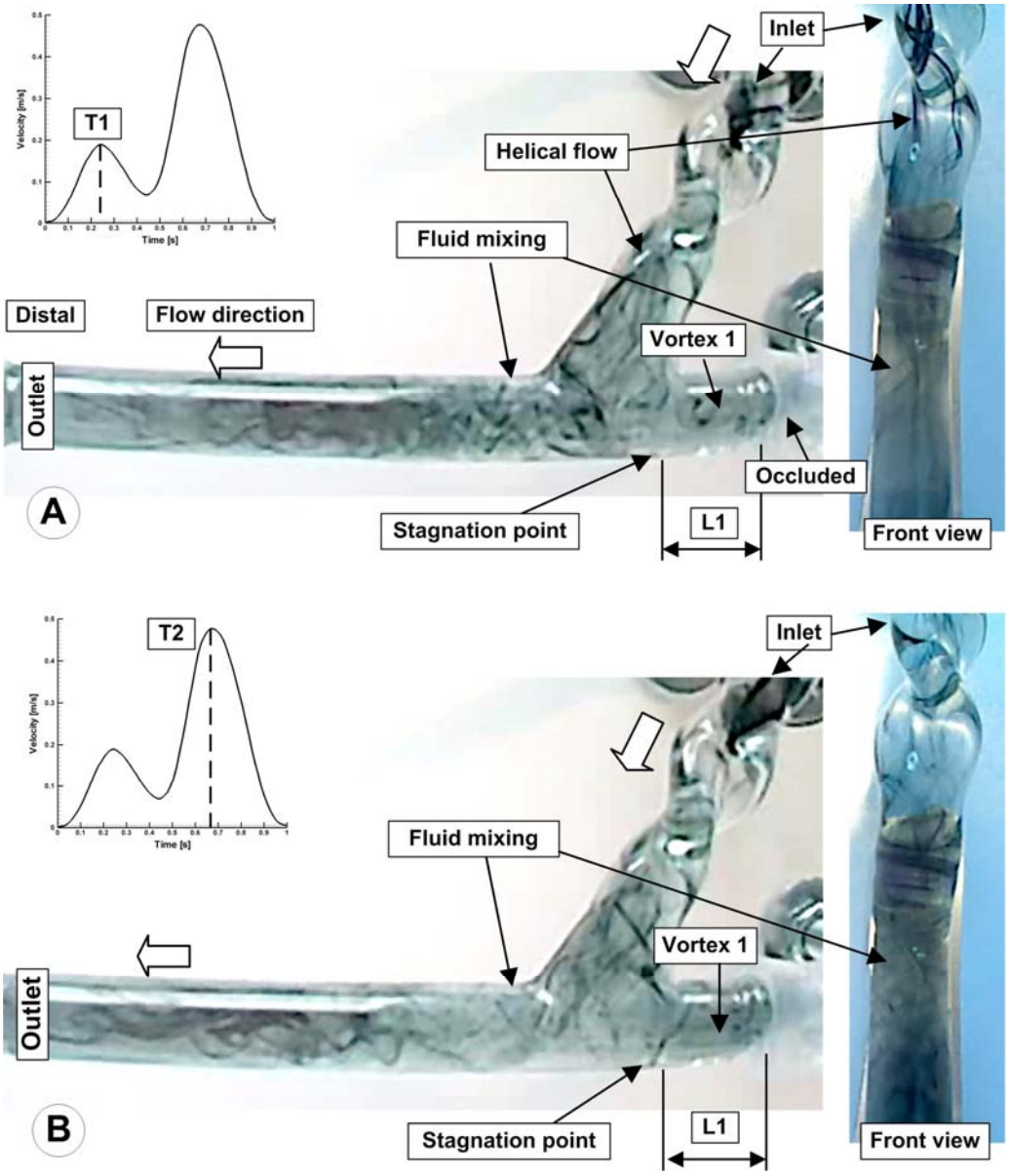

Figure 2.42. Comparison between flow pattern in the helical type bypass graft corresponding to the different time steps.

In Figure 2.41B the absence of a recirculation region may be advantageous since this reduces the contact between blood and the artificial graft surface and therefore minimizes the risk of thrombosis.

When flow in the artery reaches the anastomosis, it lifts up the stream coming from the graft and helps to direct the graft flow into the coronary artery, as shown in Figures 3B. The point of flow separation is more clearly shown in Figure 2.41 (for both investigated configurations).

The impact on the floor to be a contributing factor to the graft failure. Since Morbiducci et al. [9] have shown evidence of a change in the flow character once it has impacted against the junction floor. Hence, having a smoothened flow and a less impact on the floor of the coronary artery is a positive feature of the new CABG design.

Figures 2.42A and B shows the flow structure in the 60 degree anastomosis corresponding to the two-turns helical type graft, under pulsatile flow conditions corresponding to the first peak and second peak of the velocity waveform. During the experimental measurements input velocity waveform generated (correspond to the diastolic dominant flow regime Figure 2.42). In Figure 2.42

time T1 correspond to the peak systole and T2 to the diastolic peak respectively. Note the presence of one vortex in the occluded part of the bypass graft, and strong helical flow in the graft artery is observed in both time steps. The secondary vortex (V1), rotated anti-clockwise (as viewed in the Figures 2.42A and B). In the anastomosis domain, a recirculation is found near the occluded end of the artery. This recirculation forces the flow to move into the perfused host coronary (distal) artery as indicated in Figures 2.42A and B.

In the new design (two turns helical graft), the stagnation point is vanished from the anastomoses at different time intervals compared to the conventional bypass model (straight). Stagnation point is always associated with a low wall shear stress (WSS) and high spatial wall shear stress gradient (WSSG) region, contributing to IH and atherosclerosis development. Hence, the absence of stagnation point is another positive feature of the helical type design.

Using the four-turns helical graft increase significantly the fluid mixing both in graft and native artery. Also, flow hemodynamic characteristics was influenced by the geometry parameter of the helical part (pitch, coil diameter and numbers of coil).

In the new design, there is no vortex formed at the toe of the anastomosis within the coronary artery, resulting in a relatively higher WSS along the artery walls and bed. The presence of a vortex increases the local particle residence time which is associated with sites of IH development and may result in platelet activation and fibrin thrombus formation. The absence of vortex formation is also a positive feature of the helical type graft model.

On the whole, the geometry of the helical-type CABG is out of the plane in contrast to the in plane geometry of the traditional type CABG. The three-dimensional flow and the swirling flow represent basic flow regime in the helical type CABG.

Swirling flow induced in-plane mixing decreasing the platelets concentration near the floor and suppressed the interaction of platelets with the bypass wall.

Literature shows that the helical type flow protects the graft wall from damage by reducing the laterally directed forces. Also swirling flow provides smooth and even washing of the blood inside the artery. Additionally, helical type flow would prevent the transition from laminar flow to turbulence that help to keep flow stability and eliminate stagnation flow regions [107, 119].

The flow analysis revealed strong secondary flow in helical graft which helped the flow mixing between low-momentum fluid (near to the surface) and high-momentum fluid (at the center zone).

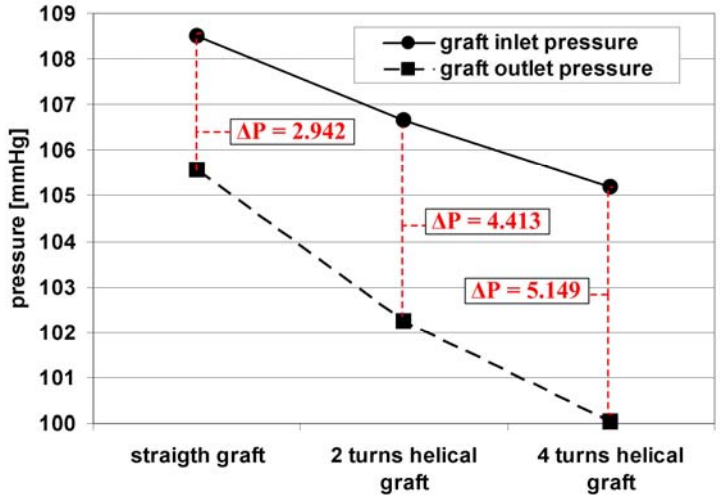

Figure 2.43. Comparison of the pressure drop for investigated by-pass geometries at the first peak of the cardiac cycle – peak systole (corresponding to Figure 4A).

Benefits aside, increased pressure drop was predicted which revealed more flow resistance at a fixed flow rate that leads to an increase in blood pressure, which might facilitates the development and progression of IH and thrombosis [120].

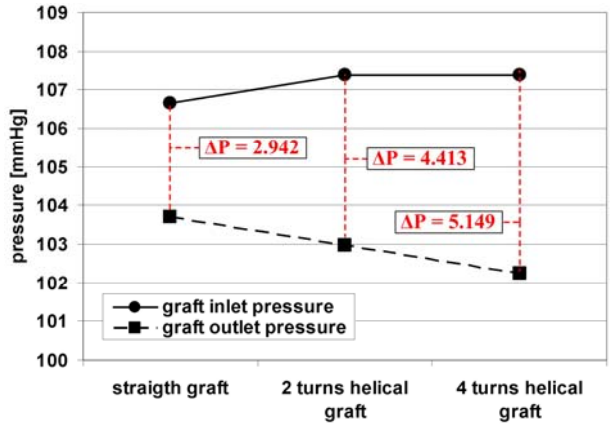

Figure 2.44. Comparison of the pressure drop for investigated by-pass geometries at the maximum velocity – second peak of the cardiac cycle (corresponding to Figure 2.41B).

In order to have a better view of the effect of helical bypass on pressure drop, three by-pass graft models were chosen for the calculation of the area-averaged pressures at two moments: a) first peak – systolic peak (Figure 2.41A); b) maximum velocity (second peak – diastolic peak) of the cardiac cycle (Figure 2.41B). The pressure drop varied with time and reached maximum at maximum velocity. Generally, the helical bypass did increase the pressure drop compared with the traditional type CABG, and the percentage increase varied with cycle. The maximum percentage increase of 75% happened at moment of maximum velocity, and the pressure drop along helical by-pass was 5.149 mm Hg (in case of four-turns helical-type graft). In case of two-turns helical graft the pressure drop increase with 50% comparatively to the straight graft (Figures 2.43, 2.44 and 2.45).

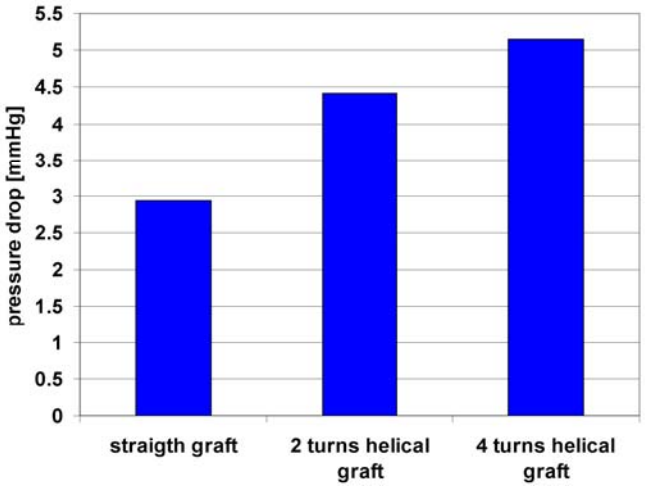

Figure 2.45. Pressure drop variations for the investigated bypass graft models.

Conclusions

Introducing helix turns in the design of the by-pass influences the hemodynamics in graft and draining artery. Helical flow generation leads a complex flow field which reduce the area of zones of unfavorable wall shear stress conditions (associated with risk of intimal hyperplasia).

For helical type design, some advantages are observed in the flow field during experimental measurements. Experimental investigations results demonstrate that the new model provides:

(i) a uniform and smooth flow at the anastomosis, without vortex in the toe region of the bypass graft;

(ii) a spare route for the blood flow to the coronary artery, to avoid re-operation in case of re-stenosis in either of the anastomoses;
(iii) good hemodynamic parameters distribution inside to the coronary artery bed and in the heel region of the anastomosis.

Our results indicated that for helical type grafts, the magnitude of the pressure drop along a helical graft was increased compared with a conventional graft. So, according to the our results the helical type CABG increased the pressure drop with maximum 75% compared with the traditional graft, which is practically out of physiological sense, but can be compensated by optimizing the geometry model.

We expect that a helical-type by-pass graft may decrease the platelets adhesion and clot formation in the graft surface and reduce the risk of IH at the distal anastomosis region.

Quantitative analysis presented in this paper contributes to understanding the impact of the advantages of the helical-type graft to improve the by-pass graft design.

(b-ii).

Scientific, professional and academic further achievement plans

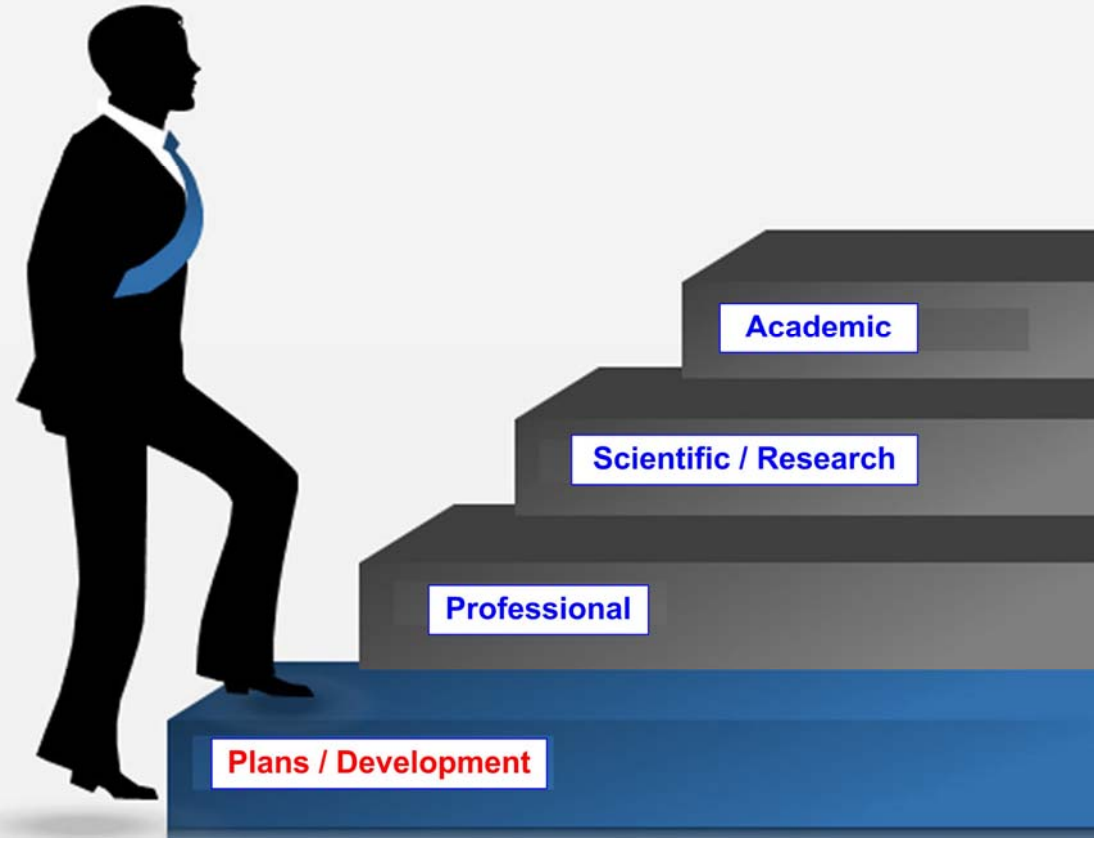

Shakespeare, and how we become more than we are today:

"*We know what we are but know not what we may be.*"

The development of my career practically focuses on the following three directions:

1. research activity,
2. educational activities and
3. publication of the results.

all of them fitted within the targeted scientific domain, namely: **Flow Hydrodynamics in Engineering and Bio-Medical Applications**.

The Development Plan is intended to assist the personal growth and career development of academic faculty, research, and scientific activities.

Formulation of an effective plan involves careful consideration of personal interests and inspirations, sources of fiscal support, and Department priorities.

It is crucial for the Academic/Professional Development Plan (ADP) to contain realistic goals and expectations and achievable ends. Consequently, the ADP should begin with a concise statement of the faculty/research member's long-term professional goals.

The ADP is intended to be a dynamic document that reflects growth and change in the faculty member's academic life over time.

This Personal Plan covers the period 2017-2027. We have shaped the Plan to meet the following aspirations:

- To develop the personal capacity to generate and share knowledge in the field of the Flow Hydrodynamics, and globally, ensuring significant contributions in education and research.
- To work effectively with other institutions and organizations, where such partnerships can lead to outstanding research and teaching.
- To enhance structures for collaboration across departments and the University.
- To recruit and retain the best researchers and academic staff and ensure that each member has equality of opportunity in recruitment, personal development, and career progression in all areas of employment at the Politehnica University of Timisoara and Romania Academy.

Identity and career
(from http://www.tankonyvtar.hu/hu/tartalom/tamop412A/2011-0023_Psychology/080400.scor)

One of the most important aspects of identity is vocational identity that is principal in the fulfilment of individual's career. Donald Super (1990) and other theorists of career development recognize the changes that people go through as they mature. Life and career development are processes that span one's entire lifetime.

Career patterns are determined by:

- mental and physical abilities,
- personal characteristics,
- socioeconomic factors, and
- opportunities to which persons are exposed.

People seek career satisfaction through work roles in which they can express themselves and implement and develop their self-concepts. Individuals' self-concept is a mental model about themselves, career self-concept is a product of the interaction of his/her personality, interests, experiences, skills, values and the ways in which the individual integrates these characteristics into his/her life roles.

Every profession has different characteristics and those who want to be successful on that path have to have suitable personality characteristics, abilities and interest to that career path.

As individuals experience new situations, meet new people, and learn more about the world of work, they are likely to develop their self-concepts.

(b-ii)_1. A few principles of the career development

Donald Super created a developmental model which emphasized how personal experiences interact with occupational preferences in creating one's self-concept. Many theorists before him simply looked at personality and occupation and focused on a trait matching approach.

One of Super's greatest contributions to career development was his emphasis on the importance of developing a self-concept, as well as his recognition that this self-concept can change with new experiences over time. Before this, career development was mostly seen as a singular choice; however, Super viewed career development as a lifelong activity.

In addition to recognizing that people change over their lifetime, he also identified different areas or "life-spaces" that help make a person who they are. The six main life-spaces that make up whom we include: parent/homemaker, worker, citizen, leisure, student, and child. So many of these roles imply that other people are involved in our lives and thus impact who we are. There are many other spaces in one's life – other than work – and Super believed that these inhabited social spaces did not constitute a distraction but were an integral part of the rainbow of our lives.

Super's work was important because his idea of the self-concept profoundly changed the field of career development. It challenged individuals to construct their identification and understanding of their life-space identities including that of their careers.

Super's theory is a good reminder that an individual's life situation changes with time and experience while noting that the concept of vocational maturity may or may not correspond with biological age.

Super's Concept of Career Maturity:
(adapted from https://oregoncis.uoregon.edu/pdf/curriculum/life_roles_rainbow_ms)

Phases of career maturity develop along multisided elements and are a life-long process. The diversity of life roles experienced by individuals over the life span includes biographical (needs, values, and interests), psychological (intelligence, aptitudes), and socioeconomic (community, school, family, peers) determinants (Figure 3.1). Developmental stages from childhood to adulthood are also part of phase development. Finally included are environmental factors such as employment practices and labor markets (Figure 3.1). The keystone of career maturity is always the self or person who experiences the personal and social forces.

Super's Life Space Transition: Roles played by individuals as they progress through career developmental stages, such as a child, student, leisure, citizen, worker, spouse, homemaker or parent, and pensioner lead to achievements and affect other role dimensions.

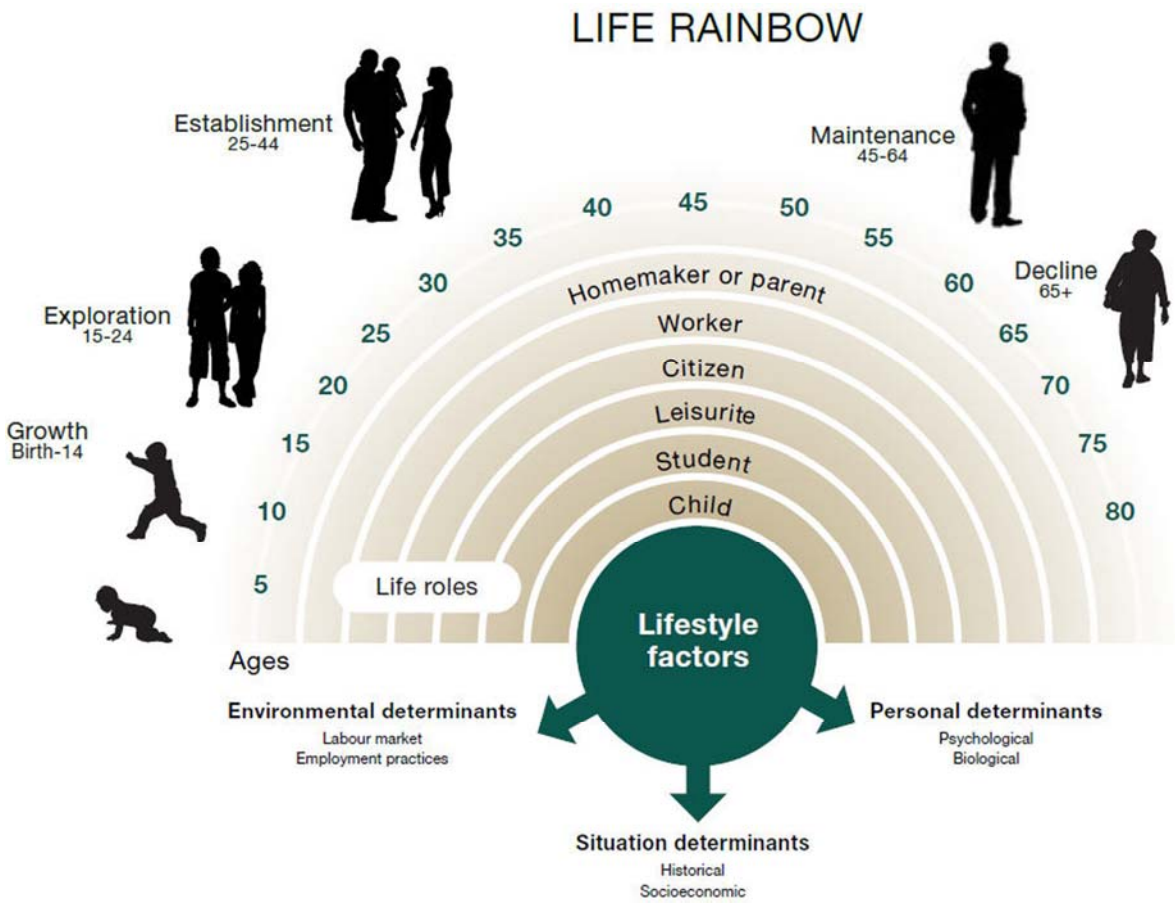

Figure 3.1 Life Rainbow of Super (adapted from [1]). Phases of career maturity develop along multisided elements and are a life-long process. The diversity of life roles experienced by individuals over the life span include biographical (needs, values and interests), psychological (intelligence, aptitudes), and socioeconomic (community, school, family, peers) determinants. Developmental stages from childhood to adulthood are also part of phase development. Finally included are environmental factors such as employment practices and labor markets. The keystone of career maturity is always the self or person who experiences the personal and social forces.

Table 3.1. Super's five life and career development stages [2]:

Stage 1: Growth	Age 0–14	Characteristics: Development of self-concept, attitudes, needs and general world of work
Stage 2: Exploration	Age 15–24	Characteristics: "Trying out" through classes, work experience, hobbies. Tentative choice and skill development
Stage 3: Establishment	Age 25–44	Characteristics: Entry-level skill building and stabilisation through work experience
Stage 4: Maintenance	Age 45-64	Characteristics: Continual adjustment process to improve position
Stage 5: Decline	Age 65+	Characteristics: Reduced output, prepare for retirement

Developmental tasks at the different stages

Super argues that occupational preferences and competencies, along with an individual's life situations all change with time and experience. Super developed the concept of vocational

maturity, which may or may not correspond to chronological age: people cycle through each of these stages when they go through career transitions.

Table 3.2. Super's developmental tasks at the different stages [adapted from 2]:

Decline			
In adolescence: Giving less time to hobbies	**In early adulthood:** Reducing sports participation	**In middle adulthood:** Focusing on essentials	**In late adulthood:** Reducing working hours
Maintenance			
In adolescence: Verifying current occupational choice	**In early adulthood:** Making occupational position secure	**In middle adulthood:** Holding one's own against competition	**In late adulthood:** Keeping what one enjoys
Establishment			
In adolescence: Getting started in a chosen field	**In early adulthood:** Settling down in a suitable position	**In middle adulthood:** Developing new skills	**In late adulthood:** Doing things one has wanted to do
Exploration			
In adolescence: Learning more about opportunities	**In early adulthood:** Finding desired opportunity	**In middle adulthood:** Identifying new tasks to work on	**In late adulthood:** Finding a good retirement place
Growth			
In adolescence: Developing a realistic self-concept	**In early adulthood:** Learning to relate to others	**In middle adulthood:** Accepting one's own limitations	**In late adulthood:** Developing and valuing non-occupational roles

The stages that Super outlined are guides looking at a macro-perspective of one's life. These stages often correlate with important events and denote a time of transition.

(b-ii)_2. Personal career development for the next 10 years

The most important stages of my career development starting to 2000 – up to date

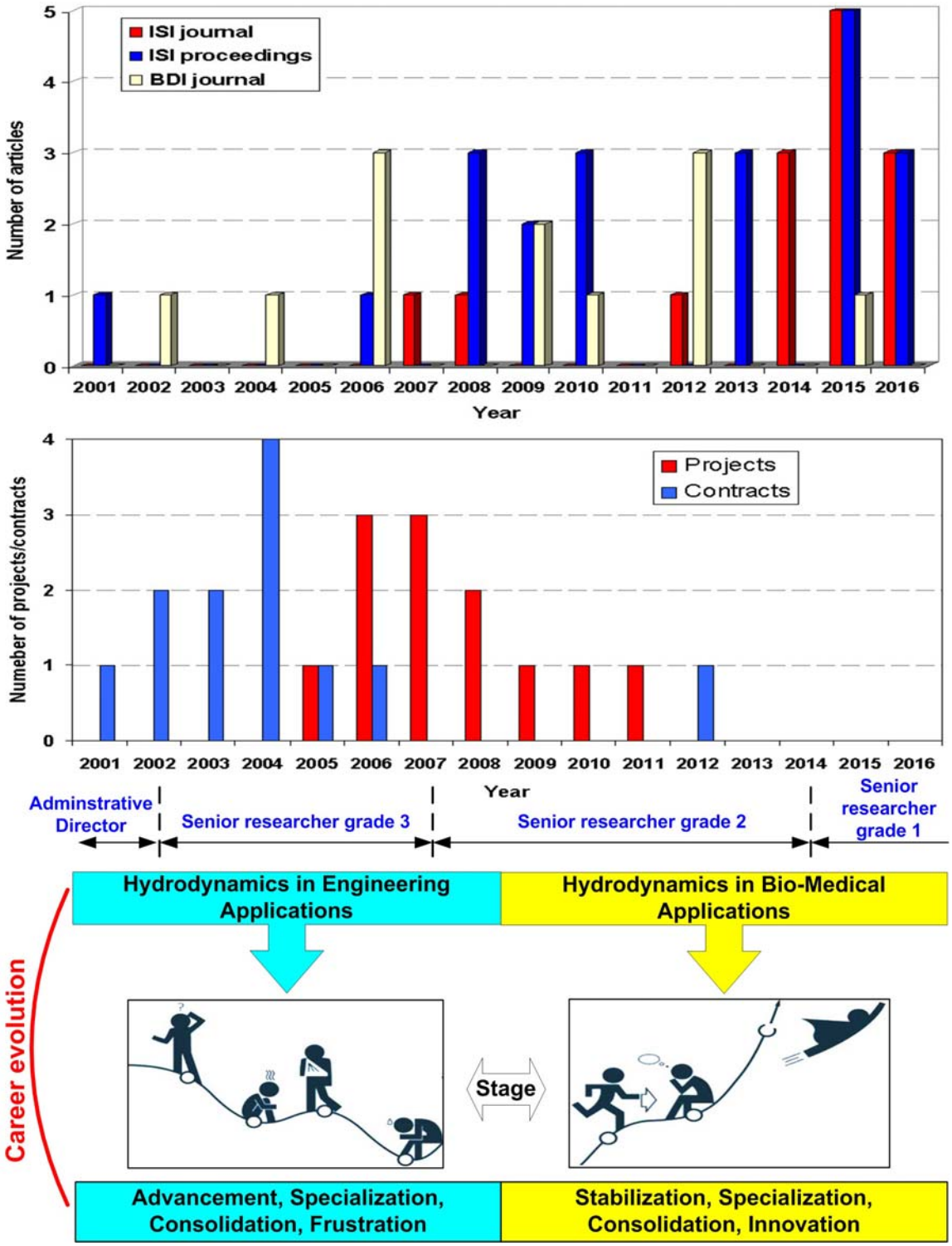

Figure 3.2 Personal career stages and experienced roles in period 2000 – to date.

Super argued that the best career choices people can make be those that provide the possibility for implementing as many parts of their self-concept as possible.
Career maturity is the main concept in Super's theory which means the successful accomplishment of age and stage developmental tasks across the lifespan [1].

By this theory, I Create the personal rainbow portraying life roles over the lifetime (Figure 3.3). In Figure 3.3 I used different colors to vision my future roles on this rainbow and mark the times in my life when I may be playing these functions.

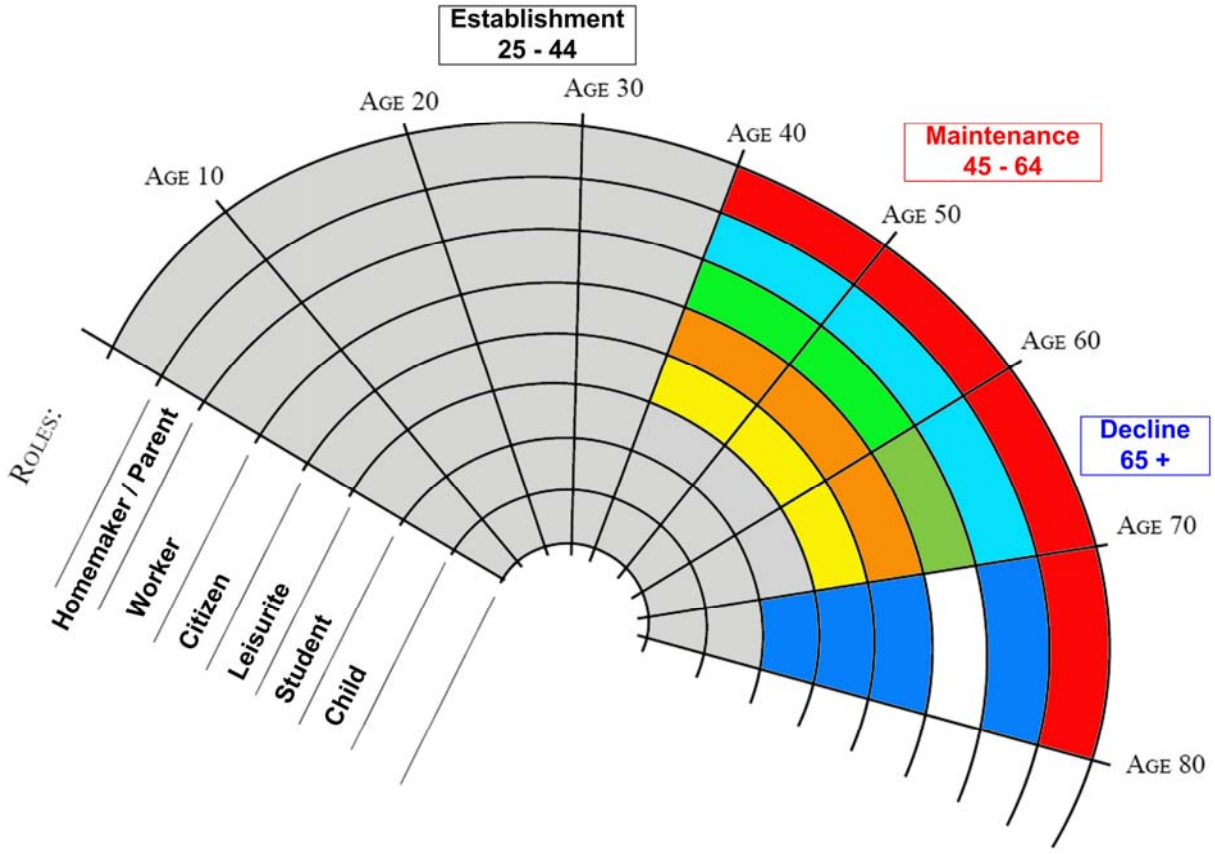

Figure 3.3 Vision of my future roles on the personal rainbow, according to Super's theory.

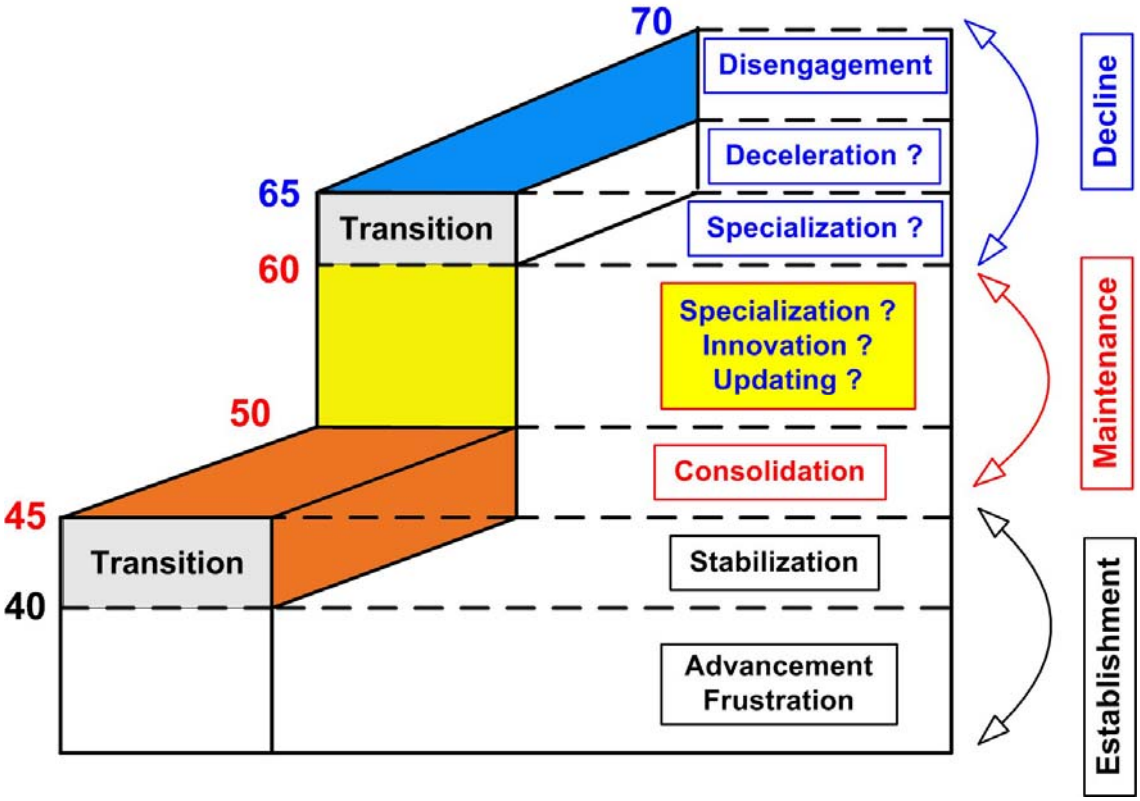

Figure 3.4 Vision and questions regarding to my progress through the career developmental stages for the **next 15 years**. This vision cover ages between 45 – 70 (left side of the scale).

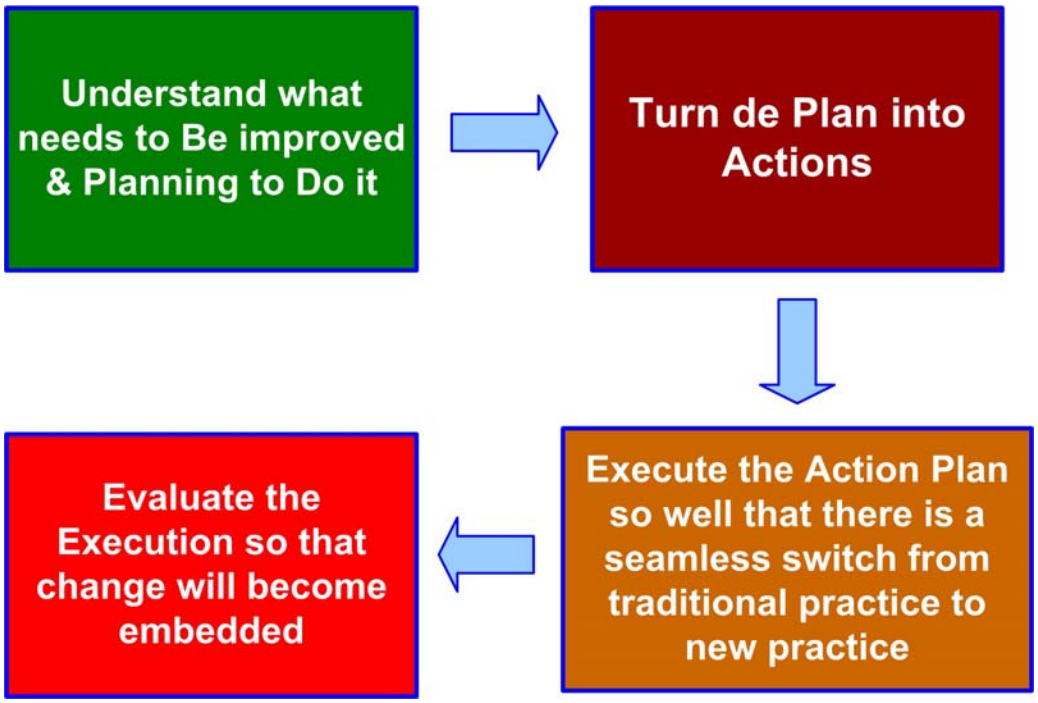

Figure 3.5 The basic principles of the personal career development.

PROFESIONAL

I intend to promote more interaction with business and industry, including through continuing professional development, collaborative research, translational activities and consulting and will be a focus on working in partnership and on developing skills and innovative services.

Priorities

- Staff and students require the best facilities for their work.
- Great science and great educational experiences require excellent laboratories and excellent learning environments.

Background	Task proposed
➢ 2014 – to date, Senior Researcher, grade I, Romanian Academy – Timisoara Branch ➢ July 2002 – to date, Executive Director, Research Center for Engineering of Systems for Complex Fluids, University Politehnica Timisoara • A number of 12 national and international projects as director and team member • A number of 37 national and international research contracts as director and team member	5. Recruit, Retain and develop a cadre of brilliant researchers and academic staff. 6. Establish and support the next generation of senior researcher and scientific leaders. 7. Build sufficient capacity and expertise to support new/challenging research themes, in my field of specialization. 8. Create and develop laboratory facilities and learning environments to provide world-class research facilities while simultaneously creating modern, flexible education instructional spaces. 9. Generate funds through projects proposals submitted at national and European levels, and through projects in collaboration with the industrial partners. 10. Maintain and develop collaboration with a scientist, academic staff, departments, universities, research centers at the national and international level.

ACADEMIC / EDUCATIONAL

Priorities

1. Graduate students, at research and master's level, are fundamental to the provision of the next generation of scientist, academics, and public servants at the national and international level.

2. Build a strong core disciplines in fluid dynamics and this application, and consequently combine with mechanisms to promote collaboration. I will try to build on my current research field to encourage the multidisciplinary cross activities.

3. I will try to bring together scholars across many disciplines and at different stages of their academic careers, to make the University the natural place of study for those who wish to learn across subject boundaries.

Some challenge regarding a successful academic evolution:

1. Create a funding opportunities for early career investigators can be organized by stage of career development and by the type of terminal degree.
2. The early years of the first junior faculty position or junior researcher, represent another critical watershed in the evolution of a successful career in fluid engineering and biomedical research. Most individuals at this stage of career development need additional training to adequately prepare them for independence.
    a. For example, the didactic component of the career development plan from a Ph.D. applicant with extensive prior research experiences and training would be expected to be very different from the didactic program designed for a claimant with little or no prior research exposure during the completion of their education and clinical training. The best candidates must demonstrate a clear commitment to and the potential for a research career, clearly, justify the need for further training, and show how the award will enable the candidate to achieve his or her career goals.
3. The process of fostering faculty development is most successful when motivated Assistant Professors or Senior Instructors work together with senior faculty and research mentors (at the professorial and associate professor, senior researcher levels) to develop a coherently organized plan for mentoring and academic advancement that recognizes the aspirations of junior faculty/researcher, together with the needs of programs and the Department.

Regarding my Educational / Academic career as a researcher with habilitation, peculiar to a certain Doctoral School, I propose to achieve the following objectives:

- **Integrating my personal studies and experience in the framework and research directions** of the Doctoral School at the Politehnica University of Timisoara (UPT), in fluid engineering and biomedical applications domain;
- A scholarship is a key ingredient, the pursuit of new knowledge is an essential feature of any academic department, and particularly critical to the Fluid Engineering domain. Thus, facilitation of the participation in peer-reviewed research is highly regarded, and **obtain as mentor the academic scholarship involving writing and publishing is essential**.
- **Promoting the career development of junior faculty** is fundamental to strengthening and renewing the University achievements and leadership in teaching and research.
- **Develop together and for master and doctoral students**, specific activities of high scientific and academic value, materialized in: projects, publishing articles, database and consistent scientific portfolio update;
- **Developing and extending some specific or new themes** in Fluid Engineering and this Biomedical applications both at the master and Ph.D. level.

SCIENTIFIC / RESEARCH

State of the art

The maintenance of a sustaining research environment is crucial both to the Politehnica University of Timisoara and Romanian Academy.

Careers in fluid engineering and biomedical research offer excellent opportunities for intellectual achievement and personal fulfillment. These careers are clearly marked with the productivity milestones of scientific publications and funding (grants).

Priorities

1. Enhance the infrastructure which supports research at the highest level, including laboratories and information systems.

2. Provide appropriate training in research methods and conduct the young peoples at all career stages from research student to the principal investigator.

3. Increased engagement with departments, university, and industrial collaborators, will enhance the capacity to set research questions in the context of the main international themes.

Challenge

- Maintain the freedom for individuals and research groups to decide what to research, while making it clear where and how to access Politehnica University and Romanian Academy expertise;
- Seek to develop external collaborations, noting that these may be most effective in those areas where research and teaching strengths are complementary while supporting connections between research groups at the level of individual projects.

Regarding my Scientific / research career, I propose to achieve the following objectives:

- Recruit, Retain and develop new young team members and encourage them to build their careers in field of Fluid Engineering and Bio-medical applications;
- Establish and support the next generation of senior researchers;
- Keeping and increase the rhythm of publishing scientific contributions, both in high-level peer-reviewed journals and international conferences;
- Developing a complex investigation system for biomedical fluid flows, with particular focus on the cardiovascular flow;
- Developing and investigation of the different drug targeting techniques for cardiovascular diseases.

The specific objectives of the future scientific activity were grouped on the following directions:

Direction No 1. Coronary artery bypass graft (CABG) flow investigation

1_1. State of the art

The long-term success of arterial bypass surgery is often limited by the progression of intimal hyperplasia at the anastomosis between the graft and the native artery [3].

To prevent the failure of implanted prostheses, the adhesion of proteins or the aggregation of platelets should be inhibited. Once a foreign body is recognized (natural or artificial graft), the proteins and platelets that are usually circulating in the bloodstream start to adhere and aggregate so that they are attached to the surface of the prostheses one by one.

Researchers have attempted various improvements to increase the hemodynamic performance of the implanted grafts [4-6] to regulate the hemodynamic parameters and wall shear stress indices, in order to avoid triggering of the pathogenic factors of IH and thrombosis (e.g., platelet activation, long near-wall residence time, etc., Figure 3.6), as well as provide a smooth blood flow without flow disturbances using the hemodynamically optimized graft and anastomotic configuration.

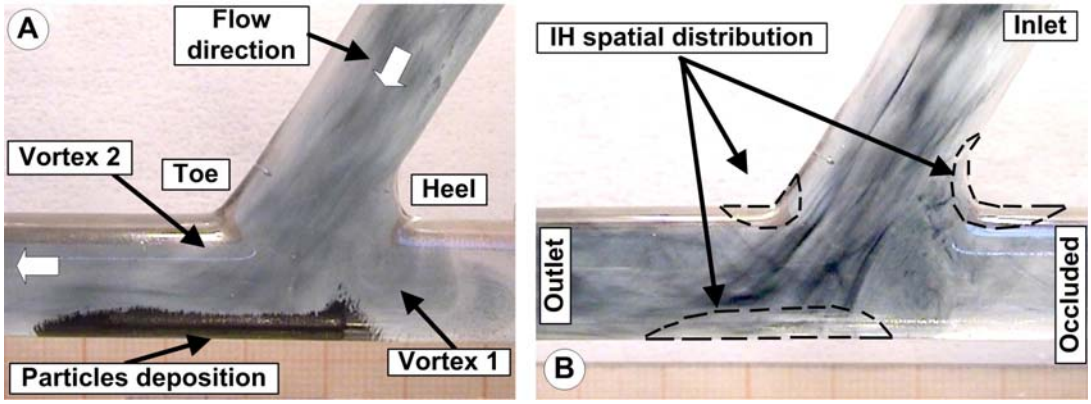

Figure 3.6. A). Experimental visualization and measurements of the particles deposition in the host artery, associated with the region prone to IH development. B) Flow visualization and identification in the distal arterial graft anastomosis the region associated with the development of the intimal hyperplasia (IH) [Bernad et al., 7].

Table 3.3. Performances comparison of the helical bypass graft model and the conventional bypass graft model.

Conventional bypass graft	Generates flow separation and extended recirculation region (Figure 3.7); Flow asymmetry on the symmetry plane of the straight graft model (Figures 3.7 B and 3.8); Strong flow impact on the artery bed and intense vortex at the heel region of the anastomosis (Figures 3.6A and B); Large flow stagnation regions = large regions of low wall shear stress = favorable site to promote inflammatory events (Figure 3.6); Increased particle residence time = possibility of thrombosis formation (Figure 3.6 A).

Helical bypass graft	Suppressing flow disturbance at the distal anastomosis (Figure 3.7 B); Promotes the mixing effect of vortex motion such that the anti-coagulant mixed vigorously into the blood stream (intrinsic coagulation process can be suppressed, so reducing the possibility of thrombosis formation) (Figure 3.7B); Strong secondary flows are present in the downstream section of the host tube, qualitatively similar to Dean-type vortices; Enhanced velocity and wall shear rate near the vessel wall = inhibition of flow stagnation and separation (Figure 3.7 B); Reduce the area of unfavorable wall shear stress conditions associated with the risk of intimal hyperplasia.

Compared to traditional planar grafts, non-planar graft configurations (especially the helical graft) improve flow characteristics by causing swirling and a relatively uniform distribution of axial and near wall velocity, avoinding and flushing of stagnant flow region reducing the potential for deposit build up within and downstream of the graft and consequently reducing potential of the development of vascular pathology [8-10] (Table 3.3).

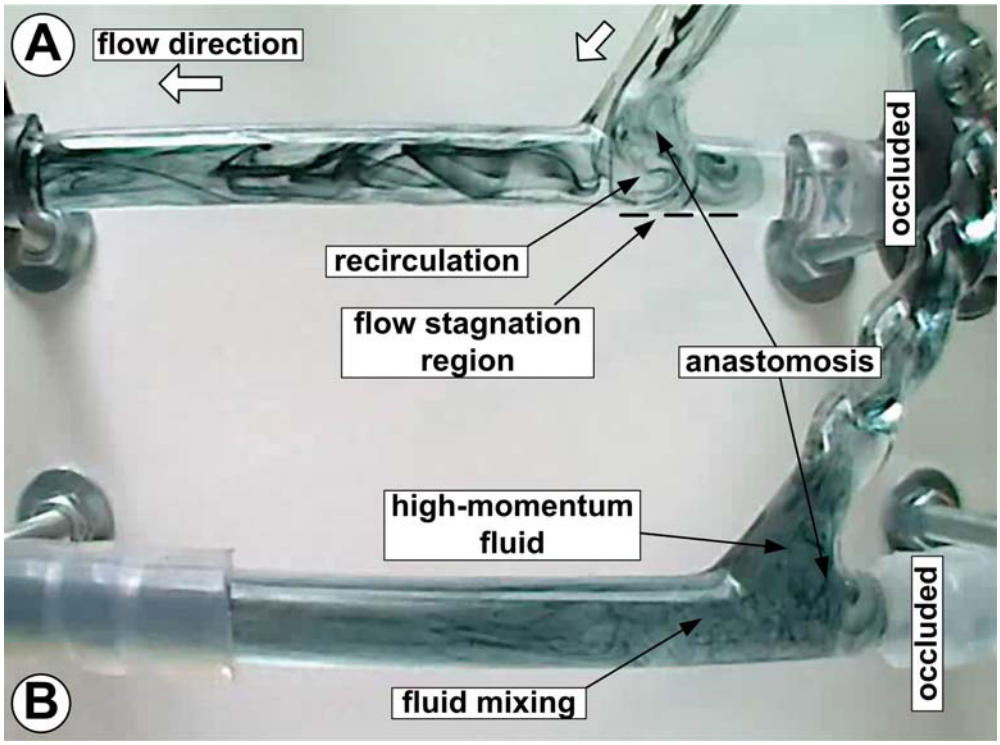

Figure 3.7. Flow visualization. Comparison between: conventional (A), and two turns helical-type artery bypass graft flows (B). Pulsatile flow condition in physiological range [Bernad et al., 7]. Clear evidence of the enhanced mixing effect of the helical flow in the graft anastomosis region (B). Both graft have the same inlet conditions and internal diameter (8 mm).

1_2. Our preliminary results

- Analysis of the hemodynamic performances of the clasical arterial bypass graft in case of the coronary bypass graft (Figure 3.8).

- Result: flow instability in the anastomosis site in terms of flow stagnation region, increased particle residence time, flow asymmetry in the distal region of the graft anastomosis (Figure 3.7).

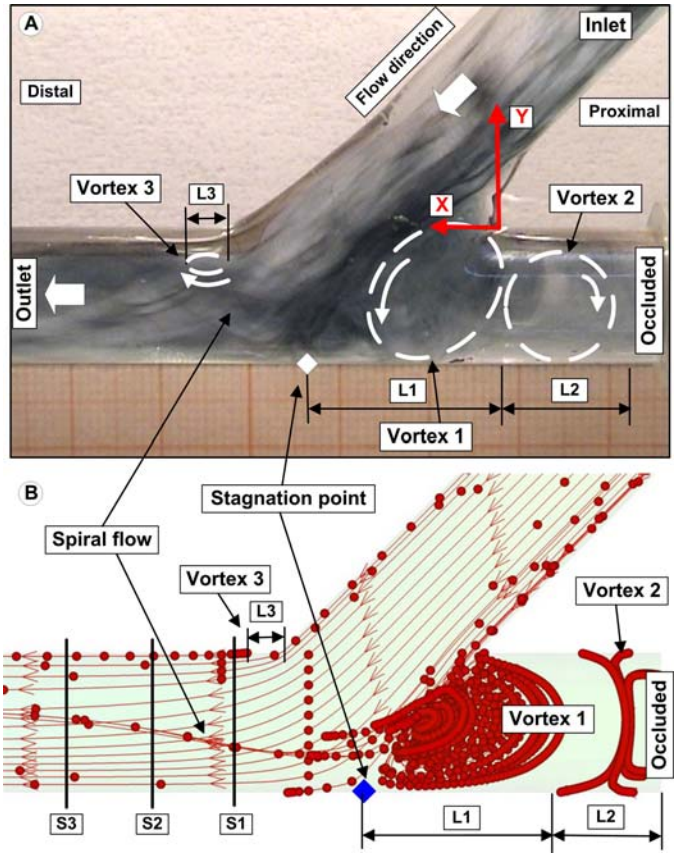

Figure 3.8 Flow visualization in clasical bypass graft anastomosis. Comparison between experimental (A) and numerical results [Totorean et al., 11].

1_3. Future activities

1. Put in evidence the advantages of the helical geometry, namely provide evidence that swirl flow generates by the helical graft operate to inhibit the development of vascular diseases such as thrombosis, atherosclerosis, and intimal hyperplasia.
2. Investigation of the swirling characteristics of the secondary flow produced by helical graft tube with various shapes.
3. Investigation of the helical graft geometries both by numerical simulation and experimental measurements for different geometrical configurations (different turns and helix amplitude, anastomosis angle, bypass graft diameter, a combination of the successive helix with various aspects of the helix amplitude).
4. Investigation hemodynamic stimuli action, such as blood pressure and wall shear stress (WSS) on the abnormal morphological and functional changes in the endothelial cells layer.

5. Comprehensive understanding of the hemodynamic characteristics of a bypass graft anastomosis is critical in identifying effective diagnosis and clinical treatments of the late graft failure.

Direction No 2. Flow investigation in stented coronary arteries

2_1. State of the art

For the treatment of coronary atherosclerotic lesions, stenting is the most commonly performed procedure during the percutaneous interventions.

Many strategies have been attempted to eliminate the acute artery response like neointimal hyperplasia (NH) and in-stent restenosis (ISR), developed after stent insertion [12]. Initialization of the NH is the result of the altered hemodynamics in stented artery. A presence of the stent causes abnormal shear stresses on the endothelial cells leading to an excessive growth of tissue in and around the implanted stent, leading to a decreased blood flow through the vessel [13].

Stent deployment alters the geometric flow boundary conditions, due to the protrusion of stent struts into the flow stream, resulting alteration of the local blood flow patterns. Detailed and accurate quantification of the local hemodynamics requires computational methods. Computational fluid dynamics (CFD) can provide detailed information on critical flow parameters including information near the stent struts and the arterial wall respectively. Different CFD studies have been proposed in the literature, where researchers investigated an idealized model [14-16], or image-based stented artery models [17, 18].

2_2. Our preliminary results

- Investigation of the different stent geometry design, to provide local flow conditions that minimize platelet adhesion while maximizing endothelial cells growth (Figure 3.9).

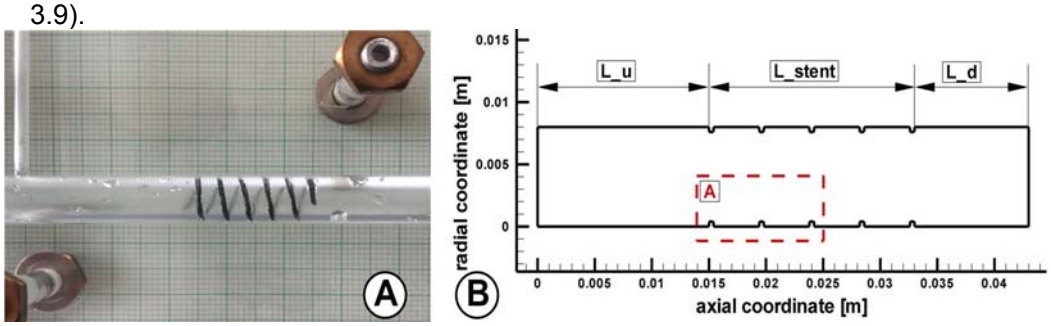

Figure 3.9 Experimental and computational domain used for stent hydrodynamics investigations.

- The flow field in the vicinity of the stent wires demonstrated the presence of the stagnation zones. This zone size is depended on directly by the wire spacing. These stagnation zones contained vortices where the velocities represent a small fraction of the velocities observed above the stent wires (Figure 3.10);

- Thicker and non-streamlined stent designs, such as rectangular strut geometry, precipitate stent thrombosis by:
  - magnifying high WSS induced platelet activation on top of struts;
  - delay re-endothelialization in low-WSS regions downstream of the struts.

- As results of the stent implantation, the vascular deformations modify the flow velocity profiles, reduce the post-implantation WSS along the entire length of the

stent, and alter the focal in-stent WSS distribution. The presence of a recirculation zone induces low values corresponding to the wall shear stress (Figure 3.11).

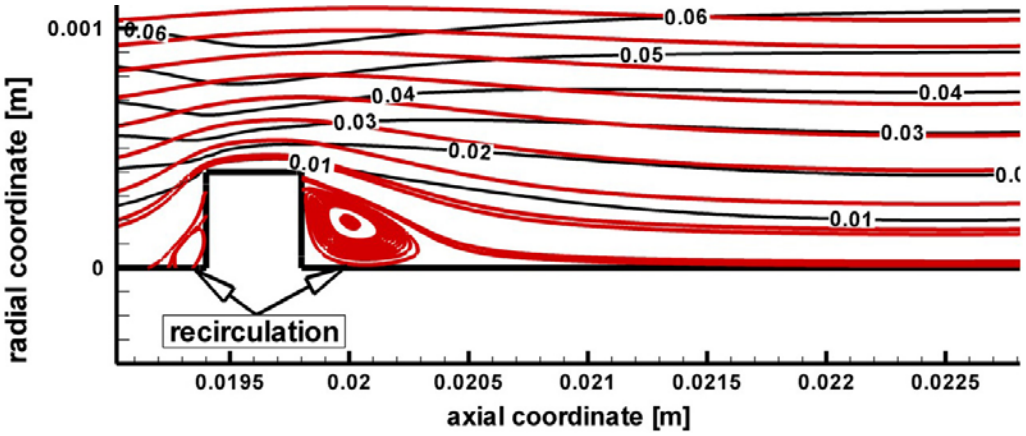

Figure 3.10. Stented coronary artery. Velocity magnitude (red line) and flow streamtrace (black line) corresponding to the different time steps.

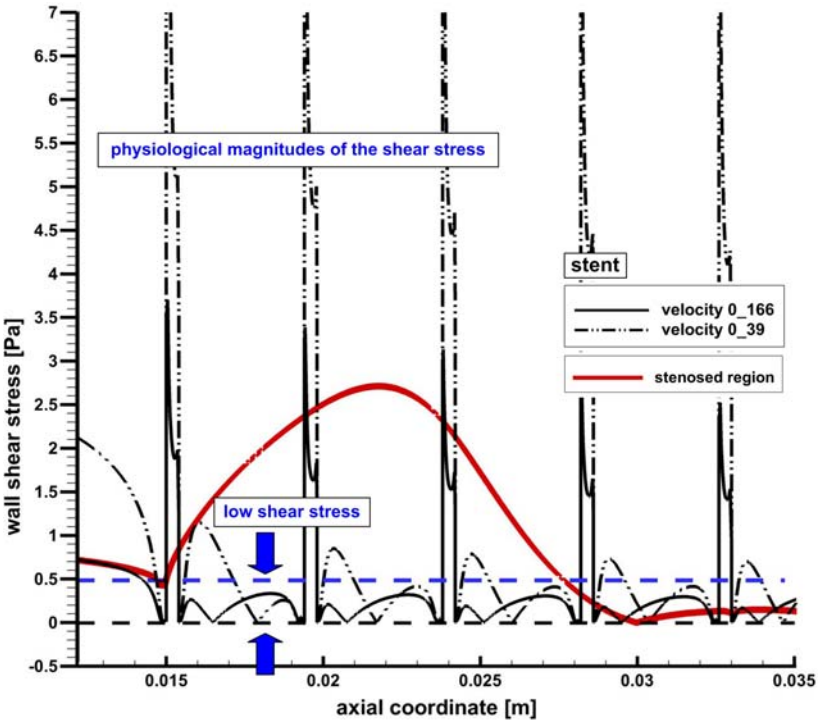

Figure 3.11. Comparison of the wall shear stress distributions between stented and stenosed artery corresponding to different investigated time steps. Wall shear stress threshold value definition used in disease quantification.

2_3. Future activities

1. Investigation of the three-dimensional stent model is required to capture spatial variations of flow hydrodynamics and drug distributions.

2. In future, efforts should be made to introduce asymmetries in artery and plaque models, and extract design metrics, to be able to rank stents based on each of their hemodynamic performances.
3. Development and investigations a stent should provide optimum vessel coverage to ensure that the vessel tissue does not prolapse between the stent struts; however, a low artery-stent contact surface area should also be maintained, because the foreign material of the stent can initiate an aggressive thrombotic response.
4. Realistic estimation of pharmacodynamics compels taking into account the three-dimensional characteristics of blood flow to predict the predecessors of reported clinical outcomes.
5. Investigations of the complex interplay between stent design (distribution of struts, link design, strut thickness, and circumferential ring design) and stent performance, from the perspective of the drug delivery performance.

(b-iii) References

For (b-i)_1

1. ARNDT, R. E. A., Cavitation in Fluid Machinery and Hydraulic Structures, Ann. Rev. of Fluid Mech., vol. 13, pp. 273-328., 1981.
2. Li S.C., Cavitation of Hydraulic Machinery, Imperial College Press, 2000.
3. KUENY, J. L., Cavitation Modeling, Lecture Series: Spacecraft Propulsion, Von Karman Institute for Fluid Dynamics, January 25-29, 1993.
4. WANG, Y-C. AND BRENNEN, C. E., Shock Wave Development in the Collapse of a Cloud of Bubbles, ASME FED, Cavitation and Multiphase Flow, vol. 194, pp. 15–19, 1994.
5. WANG, G., SENOCAK, I., SHYY, W., IKOHAGI, T., AND CAO, S., Dynamics of attached turbulent cavitating flows, Progress in Aerospace Sciences, vol. 37, pp: 551-581, 2001.
6. AVELLAN F., DUPONT P., FARHAT M., GINDROZ B., HENRY P., HUSSAIN M., PARKINSON E., SANTAL O., Flow survey and blade pressure measurements in a Francis turbine model. Proceedings of the XV IAHR Symposium, Belgrade, Yugoslavia, Vol. 2, I5, pp. 1-14, 1990.
7. AVELLAN F., DUPONT P., FARHAT M., GINDROZ B., HENRY P., HUSSAIN M., Experimental flow study of the GAMM turbine model. In Sottas G. and Ryhming I.L., (eds.), 3D-computation of incompressible internal flows, NNFM 39, pp. 33-53, Vieweg Verlag, Braunschweig, 1993.
8. LOHRBERG H., STOFFEL B., FORTES-PATELLA R., COUTIER-DELGOSHA O. REBOUD JL., Numerical and Experimental Investigations on the Cavitating Flow in a Cascade of Hydrofoils, Experiments in Fluids, 33/4, pp: 578-586, 2002.
9. KUBOTA A, KATO H., YAMAGUCHI H., A new modelling of cavitating flows: a numerical study of unsteady cavitation on a hydrofoil section, J. Fluid Mech., vol. 240, pp. 59-96, 1992.
10. SHIN B.R. AND IKOHAGI T, Numerical analysis of unsteady cavity flows around a hydrofoil, ASME-FEDSM 99-7215, San Francisco, 1999.
11. COUTIER-DELGOSHA O., PERRIN J., FORTES-PATELLA R., REBOUD J.L, A numerical model to predict unsteady cavitating flow behaviour in inducer blade cascades, Fifth int. Symp. On Cavitation, Osaka, Japan, 2003.
12. BUNNELL R.A., HEISTER S.D., Three-dimensional unsteady simulation of cavitating flows in injector passages, J. Fluid Eng. vol 122, pp 791-797, 2000.
13. SINGHAL, A. K., VAIDYA, N., AND LEONARD, A. D., Multi-Dimensional Simulation of Cavitating Flows Using a PDF Model for Phase Change, ASME FED Meeting, Paper No. FEDSM'97-3272, Vancouver, Canada, 1997.
14. COKLJAT D., IVANOV V.A., VASQUEZ S.A., Two-Phase Model for Cavitating Flows, in Third International Conference on Multiphase Flow, Lyon, France, Available on ICMF98 CD-ROM, paper 224, 1998.
15. MERKLE, C. L., FENG, J. Z., AND BUELOW P. E. O., 1998, Computational modeling of the dynamics of sheet cavitation, Third International Symposium on Cavitation, pp: 307-311, 1998.
16. KUNZ, R. F., BOGER, D. A., CHYCZEWSKI, T. S., STINEBRING, D. R., AND GIBELING, H. J., Multi-phase CFD Analysis of Natural and Ventilated Cavitation about Submerged Bodies, Proc. 3rd ASME/JSME Joint Fluid Engineering Conference, Paper FEDSM99-7364, 1999.
17. FLUENT 6.3.26, Ansys Fluent, Ansys Inc, 2006.
18. ROUSE, H., AND MCNOWN, J. S., Cavitation and Pressure Distribution, Head Forms at Zero Angle of Yaw, Studies in Engineering Bulletin 32, State University of Iowa, 1948.
19. SUSAN-RESIGA, R. F., MUNTEAN S., **BERNAD S**., ANTON, I., Numerical investigation of 3D cavitating flow in Francis turbines, Proceedings of the Conference on Modelling Fluid Flow, CMFF'03, Budapest, Hungary, pp: 950-957, 2003, ISBN 963 420 778 2.

20. DUPONT P., Etude de la Dynamique d'une Poche de Cavitation Partielle en Vue de la Prediction de l'Erosion dans les Turbomachines Hydrauliques, PhDTthesis, These No. 931, EPFL – Lausanne, 1991.
21. SENOCAK, I., AND SHYY, W., Evaluation of cavitation models for Navier-Stokes computations, Proceedings of the 2002 ASME Fluids Engineering Division Summer Meeting, Paper FEDSM2002-31011, 2002.
22. POPP, S., Mathematical Models in Cavity Theory, Technical Publishing House, Bucharest, 1985.
23. KRISHNASWAMY, P., Flow Modelling for Partially Cavitating Hydrofoils, PhD Thesis, Technical University of Denmark, 2000.
24. VAN DER HEUL, D. R., VUIK, C., WESSELING, P., Efficient computation of flow with cavitation by compressible pressure correction, European Congress on Computational Methods in Applied Sciences and Engineering ECCOMAS 2000, 2000.
25. SCHNERR, G. H., AND SAUER, J., Physical and Numerical Modeling of Unsteady Cavitation Dynamics, Proc. 4th International Conference on Multiphase Flow, New Orleans, U.S.A., 2001.
26. BULLOUNGH W.A. AND CHIN S.B., A numerical study of the effects of poppet valve geometry on its flow characteristics, Proceedings of The Ninth International Symposium on Transport Phenomena in Thermal-Fluids Engineering, Singapore, June 25-28, pp: 579-584, 1996.
27. DAVIS J.A., STEWART M., Predicting globe Control Valve performance – part I: CFD modeling, Journal of Fluid Engineering, Vol. 124, pp: 772-777, 2002.
28. HENRIK L. SORENSEN, Numerical and experimental analyses of flow and flow force characteristics for hydraulic seat valves with difference in shape, Proceedings of the Bath Workshop on Power Transmission & Motion Control, University of Bath, U.K, 1999.
29. MAIER A., SHERLDRAKE T.H., WILCOCH D., Geometric parameters influencing flow in a axisymmetric IC engine inlet port assembly – part II: parametric variation of valve geometry, Journal of Fluid Engineering, Vol. 122, pp: 658-665, 2000.
30. VON MISES, R., The Calculation of Flow Coefficient for Nozzle and Orifice, VDA, 61, pp. 21-23, 1916.
31. MAIER A., SHERLDRAKE T.H., WILCOCH D., Geometric parameters influencing flow in a axisymmetric IC engine inlet port assembly – part I: valve flow characteristics, Journal of Fluid Engineering, Vol. 122, pp: 650-657, 2000.
32. TANAKA K., Airflow Through Suction Valve of Conical Seat, Aeronautical Research Institute Report, Tokyo Imperial University, Part 1, p. 262; Part 2, p. 361., 1929.
33. JOHNSTON D.N., EDGE K.A., VAUGHAN N.D., Experimental investigation of flow and force characteristics of hydraulic poppet and disc valves, Proc Instn.Mech.Engrs. Vol. 205, pp: 161-171, A01889 ImechE, 1991.
34. SCHRENK E., Disc Valves, Flow Patterns, Resistance, and Loading, BHRA Publications, T547, 1957.
35. STONE J. A., Discharge Coefficients and Steady State Flow Forces for Hydraulic Poppet Valves, Trans. ASME, 144., 1960.
36. McCLOY D., and McGUIGAN R. H., Some Static and Dynamic Characteristics of Poppet Valves, Proc. Inst. Mech. Eng., 179, 1964.
37. VAUGHAN N.D., JOHNSTON D.N., Numerical simulation of fluid flow in poppet valves, Proc Instn. Mech. Engrs., C413/0779 ImechE, pp: 119-127, 1991.
38. WECLAS M., MELLING A., AND DURST F., Flow Separation in the Inlet Valve Gap of Piston Engines, Prog. Energy Combust. Sci., 24, No. 3, pp.165–195, 1998.
39. **BERNAD S.**, SUSAN-RESIGA R., ANTON I., ANCUŞA V., Vortex Flow Modeling Inside The Poppet Valve Chamber - Part 2, Bath Workshop on Power Transmission & Motion Control, PTMC 2001, Bath, UK, 12 – 14 September, 161-176, 2001.
40. DIETZE M., Messung und Berechnung der Innenströmung in hydraulischen Sitzventilen, Ph.D. Thesis, Düsseldorf, 1996.

41. RESIGA R., **BERNAD S.I.**, ANTON I., Vortex Flow Modeling Inside the Poppet Valve Chamber, The Seventh Scandinavian International Conference on Fluid Power, SICFP'01, May 30 - June 1, Linkoping, Sweden, 2001.
42. **BERNAD S.**, SUSAN-RESIGA R., ANTON I., ANCUŞA V., Numerical Simulation of Cavitating Flow in Hydraulic Poppet Valve, In I. Anton, V. Ancuşa, R. Resiga (Eds.), Proceedings of the Workshop on Numerical Simulation for Fluid Mechanics and Magnetic Liquids, Editura Orizonturi Universitare, Timişoara, 140-146, 2001.
43. Muntean S., Susan-Resiga R., **Bernad S.**, Anton I., Analysis of the GAMM Francis Turbine Distributor 3D Flow for the Whole Operating Range and Optimization of the Guide Vane Axis Location, Scientific Bulletin of the 'Politehnica' University of Timisoara, Transactions on Mechanics, Tom 49(63), Special Issue, pp: 131- 136, 2004.
44. **Bernad S**, Susan-Resiga R, Muntean S, Anton I. Numerical analysis of the cavitating flows. Proceedings of the Romanian Academy, Series A: Mathematics, Physics, Technical Sciences, Information Science, 7(1):1–13, 2006.
45. **Bernad S.**, Susan-Resiga R., Muntean S., Anton I., Cavitation phenomena in hydraulic valves. Numerical modelling, Proceedings of the Romanian Academy, Series A, Vol. 8, No. 2/2007, pp: 117-126, 2007.

For (b-i)_2

[1] D. Bluestein, C. Gutierrez and M. Londono M. Schoephoerster, Vortex shedding in steady flow through a model of an arterial stenosis and its relevance to mural platelet deposition, Annals of Biomedical Engineering 27 (1999), 763–773.
[2] J. Stroud, S. Berger and D. Saloner, Influence of stenosis morphology on flow through severely stenotic vessels: implications for plaque rupture, Journal of Biomechanics 33 (2000), 443–455.
[3] J.K. Morton, Curriculum in Interventional Cardiology: Coronary Pressure and Flow. Measurements in the Cardiac Catheterization Laboratory, Catheterization and Cardiovascular Interventions 54 (2001), 378–400.
[4] K.L. Gould and K. Lipscomb, Effects of coronary stenoses on coronary flow reserve and resistance, Am. J. Cardiol 34 (1974), 48–55.
[5] K.L. Gould, R.L. Kirkeeide and M. Buchi, Coronary flow reserve as a physiologic measure of stenosis severity, J Am CollCardiol 15(1990), 459–474.
[6] N. Talukder, P.E. Karayannacos, R.M. Nerem and J.S. Vasko, An experimental study of the fluid dynamics of multiple noncritical stenoses, ASME Biomechanical Engineering, (1977), 74–82.
[7] S.C. Van Dreumel and G.D.C. Kuiken, Steady flow through a double converging–diverging tube model for mild coronary stenoses, Journal of Biomechanical Engineering 111(1989), 212–221.
[8] D. Kilpatrick, S.D. Webber and J-P. Colle, The vascular resistance of arterial stenoses in series, Angiol 41(1990), 278–285.
[9] K.l. Gould, K. Lipscomb and G.W. Hamilton, Physiologic basis for assessing critical coronary stenosis: instantaneous flow response and regional distribution during coronary hyperemia as measures of coronary flow reserve, Am J Cardiol 33 (1974), 87–94.
[10] H.N. Sabbah and P.D. Stein PD, Hemodynamics of multiple versus single 50 percent coronary arterial stenoses, Am. J. Cardiol 50 (1982), 276–280.
[11] Johnston, B.M., Johnston, P.R., Corney, S. & Kilpatrick, D., Non-Newtonian blood flow in human right coronary arteries: transient simulations. Journal of Biomechanics, 39, pp. 1116–1128, 2005.
[12] **Bernad S.I.**, Totorean A., Bernad E.S. & Susan-Resiga R., "Particle motion in coronary serial stenoses" WIT Transaction on Biomedice and Health, Vol 17, WIT Press, 2013, ISSN: 1743-3525, doi. 10.2495/BIO130151.

[13] C. Bertolotti, Z. Qin, B. Lamontagne, L-G. Durand, G. Soulez and G. Cloutier, Influence of multiple stenoses on echo-Doppler functional diagnosis of peripheral arterial disease: a numerical and experimental study, Ann. Biomed. Eng 34 (2006), 564–574.

[14] M.J. Kern, B. De Bruyne and N.H. Pijls, From research to clinical practice: current role of intracoronary physiologically based decision making in the cardiac catheterization laboratory, J Am CollCardiol 30 (1997), 613–20.

[15] N.H. Pijls, J.A. van Son, R.L. Kirkeeide, B. De Bruyne, K.L. Gould, Experimental basis of determining maximum coronary, myocardial, and collateral blood flow by pressure measurements for assessing functional stenosis severity before and after percutaneous transluminal coronary angioplasty, Circulation 87 (1993), 1354–67.

[16] B. De Bruyne, J. Bartunek, S.U. Sys, N.H. Pijls, G.R. Heyndrickx and W. Wijns, Simultaneous coronary pressure and flow velocity measurements in humans. Feasibility, reproducibility, and hemodynamic dependence of coronary flow velocity reserve, hyperemic flow versus pressure slope index, and fractional flow reserve, Circulation 94 (1996), 1842–9.

[17] S.A. Chamuleau, M. Meuwissen, K.T. Koch, et al, Usefulness of fractional flow reserve for risk stratification of patients with multivessel coronary artery disease and an intermediate stenosis, Am J Cardiol 89 2002), 377– 80.

[18] C.E.E. Hanekamp, J.J. Koolen, N.H. Pijls, et al. Comparison of quantitative coronary angiography, intravascular ultrasound, and coronary pressure measurement to assess optimum stent deployment, Circulation 99 (1999), 1015–21.

[19] N.H.J. Pijls, B. De Bruyne, G. Jan Willem Bech, F. Liistro, G.R. Heyndrickx, H.J.R.M. Bonnier and J.J. Koolen, Coronary pressure measurement to assess the hemodynamic significance of serial stenoses within one coronary artery: validation in humans, Circulation102 (2002), 2371–2377.

[20] Johnston, P.R. & Kilpatrick, D., Mathematical modeling of paired arterial stenoses, Proc. Comput. Cardiol, pp. 229–232, 1990.

[21] **S.I. Bernad**, E. Bernad, T. Barbat, V. Albulescu and R. Susan-Resiga, Effects of different types of input waveforms in patient-specific right coronary atherosclerosis hemodynamics analysis, Int. J. of Design & Nature and Ecodynamics 5(2) (2010), 1-18.

[22] S.R. Dodds, The haemodynamics of asymmetric stenoses, European Journal of Vascular Endovascular Surgery24 (2002), 332–337.

[23] B. Liu, The influences of stenosis on the downstream flow pattern in curved arteries, Medical Enginnering& Physics29 (2007), 868–876.

[24] M. Eliasziw, R.F. Smith, N. Singh, et al., Further comments on the measurement of carotid stenosis from angiograms: North American Symptomatic Carotid Endarterectomy Trial (NASCET) Group. Stroke25 (1994), 2445–49.

[25] P.M. Rothwell, M. Eliasziw, S.A. Gutnikov SA, et al., Analysis of pooled data from the randomized controlled trials of endarterectomy for symptomatic carotid stenosis, Lancet361 (2003), 107–16.

[26] FLUENT 6.3 User's Guide. Ansys Fluent Incorporated (2006).

[27] Clark, C., The propagation of turbulence produced by a stenosis. J. Biomech, 113, pp. 591–604, 1980.

[28] Khalifa, A.M.A. & Giddens, D.P., Characterization and evolution of poststenotic flow disturbances. J. Biomech., 14, pp. 279–296, 1981.

[29] Kim, B.M. & Corcoran, W.H., Experimental measurements of turbulence spectra distal to stenoses. J. Biomech., 7, pp. 335–342, 1974.

[30] Ghalichi, F. & Deng, X., Turbulence detection in a stenosed artery bifurcation by numerical simulation of pulsatile blood flow using the low-Reynolds number turbulence model. Biorheology, 40, pp. 637–654, 2003.

[31] Mittal, R., Simmons, S.P. & Udaykumar, H.S., Application of large-eddy simulation to the study of pulsatile flow in a modeled arterial stenosis. J. Biomech. Engrg, 123, pp. 325–332, 2001.

[32] Rayz, V.T., Berger, S.A. & Salomer, D., Transitional flow in arterial fluid dynamics. Comput. Methods Appl. Mech. Engrg, 196, pp. 3043–3048, 2007.

[33] Loree, H.M., Ramm, R.D., Atkinson, C.M. & Lee, R.T., Turbulent pressure fluctuations on surface of model vascular stenoses, Am. J. Physiol, 261, H644–H650, 1991.
[34] E.S. Bernad, **S.I. Bernad**, M.L. Craina, Hemodynamic parameters measurements to assess severity of serial lesions in patient specific right coronary artery, Bio-Medical Materials and Engineering, Volume 24(1), 2014, pp: 323-334, DOI 10.3233/BME-130814,
[35] Di Mario, C., Meneveau, C., Gil, R., Jaegere, P. Feyter, P.J., Slager, C., Roelandt, J.R.T.C. & Serruys, P.W., Maximal blood flow velocity in severe coronary stenoses measured with a doppler guidewire, Limitations for the application of the continuity equation in the assessment of stenosis severity. American Journal of Cardiology, 71, pp. 54D-61D, 1993.
[36] Li, L.X., Beech-Brandt, J.J., John, L.R., Hoskins, P.R. & Easson, W.J., Numerical analisys of pulsatile blood flow and vessel wall mechanics in different degrees of stenoses. Journal of Biomechanics, 40, pp. 3715-3724, 2007.
[37] Siebes, M., Verhoeff, B-J., Meuwissen, M., de Winter, J., Jos, R., Spaan A.E. & Piek, J.J., Single-Wire Pressure and Flow Velocity Measurement to Quantify Coronary Stenosis Hemodynamics and Effects of Percutaneous Interventions. Circulation, 109, pp. 756-762, 2004.
[38] **S.I. Bernad**, E.S. Bernad, A.F. Totorean, M.L. Craina, I. Sargan, Clinical important hemodynamic characteristics for serial stenosed coronary artery, International Journal of Design & Nature and Ecodynamics, 2015, 10(2):97-113, 2015
[39] Goldsmith, H.L. & Turitto, V.T., Rheological aspects of thrombosis and haemostasis: Basic principles and applications. Thromb Haemost, 55, pp. 415–435, 1986.
[40] Davies, P.F., Remuzzi, A., Gordon, E.J., Dewey Jr., C.F. & Gimbrone Jr., M.A., Turbulent fluid shear stress induces vascular endothelial cell turnover in vitro. Proc NatlAcad Sci USA, 83, pp. 2114-2117, 1986.
[41] Langille, B.L. & O'Donnell, F., Reductions in arterial diameter produced by chronic decrease in blood flow are endothelium dependent. Science, 231, pp. 405-407, 1986.
[42] **BERNAD Sandor**, BERNAD Elena, CRAINA Marius, Sargan Izabella, TOTOREAN Alin, BRISAN Cosmin, Particle Depositions and Related Hemodynamic Parameters in the Multiple Stenosed Right Coronary Artery, Journal of Clinical Medicine Research, vol 4, no 3, pp: 177-189, doi:10.4021/jocmr843w, 2012.
[43] Zand, T., Manjo, G., Nunnari, J.J., Hoffman, A.H., Savilonis, B.J., MacWilliams, B. & Joris, I., Lipid Deposition and Intimal Stress and Strain—A Study in Rats With Aortic Stenosis. American Journal of Pathology, 139(2), pp. 101-113, 1991.
[44] Schoephoerster, R.T., Gynes, F., Nunez, G., Kapadvanjwala M. & Dewanjee, M.K., Effects of Local Geometry and Fluid Dynamics on Regional Platelet Deposition on Artificial Surfaces. Arteriosclerosis and Thrombosis, 13(12), pp. 1806-1813, 1993.
[45] H. Suma, T. Isomura, T. Horii, T. Sato, Late angiographic result of using the right gastroepiploic artery as a graft, J. Thorac. Cardiovasc. Surg, 2000, 120:496–8.
[45] A.J. Tector, T. M. Schmahl, Techniques for multiple internal mammary artery bypass grafts, Ann Thorac Surg, 1984, 38:281– 6.
[46] B. F. Buxton, J. S. Raman, P. Ruengsakulrach, et al., Radial artery patency and clinical outcomes: five-year interim results of a randomized trial, J Thorac Cardiovasc Surg, 2003, 125:1363–71.
[47] R. Dion, D. Glineur, D. Derouck, et al., Complementary saphenous grafting: long-term follow-up, J Thorac Cardiovasc Surg, 2001, 122: 296–304.
[48] G. M. Fitzgibbon, H. P. Kafka, A. J. Leach, W. J. Keon, G. D. Hooper, J. R. Burton, Coronary bypass graft fate and patient outcome: angiographic follow-up of 5,065 grafts related to survival and reoperation in 1,388 patients during 25 years, J Am Coll Cardiol 1996, 28:616-626.
[49] J. T. Lie, G. M. Lawrie, G. C. Morris Jr., Aortocoronary bypass saphenous vein graft atherosclerosis. Anatomic study of 99 vein grafts from normal and hyperlipoproteinemic patients up to 75 months postoperatively, Am J Cardiol, 1977, 40:906-914.
[50] S. Bhardwaj, H. Roy, S. Ylä-Herttuala, Gene therapy to prevent occlusion of venous bypass grafts, Expert Rev Cardiovasc Ther, 2008, 6:641–652.

[51] R. Berguer, R. F. Higgins, D. J. Reddy, Intimal hyperplasia, Arch Surg, 1980, 115:332–335.
[52] P. B. Dobrin, F. N. Littooy, E. D. Endean, Mechanical factors predisposing to intimal hyperplasia and medial thickening in autogenous vein grafts, Surgery, 1989, 105:393–400.
[53] Z. Jiang, L. Wu, B. L. Miller, D. R. Goldman, C. M. Fernandez, Z. S. Abouhamze, C. K. Ozaki, S. A. Berceli, A novel vein graft model: adaptation to differential flow environment, Am J Physiol Heart Circ Physiol, 2004, 286:H240–H245.
[54] S. Goldman, J. Copeland, T. Moritz, et al., Saphenous vein graft patency one year after coronary artery bypass surgery and effects of antiplatelet therapy, Circulation, 1989, 80:1190 –7.
[55] S. Goldman, J. Copeland, T. Moritz T, et al., Internal mammary artery and saphenous vein graft patency: effects of aspirin, Circulation, 1990, 82 Suppl IV:IV-237–42.
[56] S. Goldman, J. Copeland, T. Moritz, et al., Starting aspirin therapy after operation: effects on early graft patency, Circulation, 1991, 84:520–6.
[57] K. Nieman, M. Oudkerk, B. J. Rensing, P. van Ooijen, A. Munne, R. J. van Geuns, P. j. de Feyter, Coronary angiography with multi-slice computed tomography, Lancet, 2001, 357:599-603.
[58] T. Schlosser, T. Konorza, P. Hunold, H. Kuhl, A. Schmermund, J. Barkhausen, Noninvasive visualization of coronary artery bypass grafts using 16-detector row computed tomography, J Am Coll Cardiol, 2004, 44:1224-1229.
[59] M. H. Song, T. Ito, T. Watanabe, H. Nakamura, Multidetector computed tomography versus coronary angiogram in evaluation of coronary artery bypass grafts, Ann Thorac Surg, 2005, 79:585-588.
[60] T. S. Hall, J. Ferguson, J. Sines, A. J. Spotnitz, Comparison of the flow capacity of free arterial grafts and saphenous vein grafts for coronary bypass surgery, Cardiovascular Surgery, Vol. 9, No. 1, pp. 27–32, 2001.
[61] R. Torii, N.B. Wood, N. Hadjiloizou, A.W. Dowsey, A.R. Wright, A.D. Hughes, J. Davies, D.P. Francis, J. Mayet, G-Z. Yang, S.A.McG. Thom, X.X. Yun, Fluid-structure interaction analysis of a patient-specific right coronary artery with physiological velocity and pressure waveforms. Communications in Numerical Methods in Engineering, 25, 2009, 565-580.
[62] D. Zeng, E. Boutsianis, M. Ammann, K. Boomsma, S. Wildermuth, D Poulikakos, A study on the Compliance of a Right Coronary Artery and Its Impact on Wall Shear Stress, Journal of Biomechanical Engineering, 2008, 130, 041014-1:11.
[63] E. S. Houslay, T. Lawton, A. Sengupta, N. G. Uren, G. McKillop, D. E. Newby, Non-invasive assessment of coronary artery bypass graft patency using 16-slice computed tomography angiography, Journal of Cardiothoracic Surgery, 2007, 2:27
[64] **S.I. Bernad**, E.S. Bernad, Coronary venous bypass graft failure, hemodynamic parameters investigation, International Conference Biomedical Engineering (BioMed 2012), February 15-17, 2012 Innsbruck, Austria, pp. 509-515.
[65] T. Chaichana, Z. Sun, J. Jewkes, Computational Fluid Dynamics Analysis of the Effect of Plaques in the Left Coronary Artery, Computational and Mathematical Methods in Medicine, Volume 2012, Article ID 504367, 9 pages doi:10.1155/2012/504367.
[66] E. Kouhi, Y. S. Morsi, S. H. Masood, Haemodynamic analysis of coronary artery bypass grafting in a non-linear deformable artery and Newtonian pulsatile blood flow, Proc. IMechE Vol. 222 Part H: J. Engineering in Medicine, 2008, 222, 1273-1287.
[67] R. Torii, N.B. Wood, N. Hadjiloizou, A. W. Dowsey, A. R. Wright, A. D. Hughes, J. Davies, D. P. Francis, J. Mayet, G-Z Yang, S. A. Thom, X. X. Yun, Differences in coronary artery haemodynamics due to changes in flow and vascular geometry after percutaneous coronary intervention, Heart, 2008, 94, A1–A4.
[68] J. P. Ku, C. J. Elkins, C. A. Taylor, Comparison of CFD and MRI Flow and Velocities in an In Vitro Large Artery Bypass Graft Model, Annals of Biomedical Engineering, 2005, Vol. 33, No. 3, pp. 257–269.
[69] J. A. Moore, D. A. Steiman, D. W. Holdsworth, C. R. Ethier, Accuracy of computational hemodynamics in complex arterial geometries reconstructed from magnetic resonance imaging, Ann. Biomed. Eng.,1999; 27: 32–41.

[70] D. L. Fry, Acute vascular endothelial changes associated with increased blood velocity gradients, Circulation Research, 1968, 22:165–197.
[71] C. G. Caro, J. M. Fitz-Gerald and R. C. Schroter, Atheroma and arterial wall shear. Observation, correlation and proposal of a shear dependent mass transfer mechanism for atherogenesis, Proc.R. Soc. B, Biol. Sci., 1971, 177(46), 109–159.
[72] B. B. Lieber and D. P. Giddens, Poststenotic core flow behavior in pulsatile flow and its effects on wall shear-stress, J. Biomechanics, 1990, 23(6), 597–605.
[73] L. Goubergrits, K. Affeld, E. Wellnhofer, R. Zurbrugg and T. Holmer, Estimation of wall shear stress in bypass grafts with computational fluid dynamics method, Int. J. Artif. Organs, 2001, 24(3), 145–151.
[74] M. G. Bourassa, Fate of venous grafts: the past, the present and the future, J Am Coll Cardiol, 1991, 5:1081–1083.
[75] B. Jung, M. Markl, D. Foll, J. Hennig, Investigating myocardial motion by MRI using tissue phase mapping, Eur J Cardiothorac Surg, 2006, 29 (Suppl. 1):S150-7.
[76] E. Weigang, F. A. Kari, F. Beyersdorf, et al., Flow-sensitive fourdimensional magnetic resonance imaging: flow patterns in ascending aortic aneurysms, Eur J Cardiothorac Surg, 2008, 34:11-6.
[77] M. Markl, M. T. Draney, M. D. Hope, et al., Time-resolved 3-dimensional velocity mapping in the thoracic aorta: visualization of 3-directional blood flow patterns in healthy volunteers and patients, J Comput Assist Tomogr, 2004, 28:459-68.
[78] P. A. Stonebridge, C. M. Brophy, Spiral laminar flow in arteries?, Lancet, 1991, 338: 1360 - 1360
[79] C. G. Caro, N. J. Cheshire, N. Watkins, Preliminary comparative study of small amplitude helical and conventional ePTFE arteriovenous shunts in pigs, J R Soc Interface, 2005, 2:261-6.
[80] Z. Zhang, Y. Fan, X. Deng, et al., Simulation of blood flow in a small-diameter vascular graft model with a swirl (spiral) flow guider, Sci China C Life Sci, 2008, 51:913-21.
[81] D. Zeng, Z. Ding, M. H. Friedman, C. R. Ethier, Effects of Cardiac Motion on Right Coronary Artery Hemodynamics, Annals of Biomedical Engineering, 2003, 31:420–429.
[82] A. M. Malek, S. Izumo, Molecular aspects of signal transduction of shear stress in the endothelial cell, J Hypertens, 1994,12:989-99.
[83] A. M. Malek, R. Jackman, R. D. Rosenberg, et al, Endothelial expression of thrombomodulin is reversibly regulated by fluid shear stress, Circ Res, 1994, 74:852-60.
[84] J. G. Motwani and E. J. Topol, Aortocoronary Saphenous Vein Graft Disease: Pathogenesis, Predisposition, and Prevention, Circulation, 1998, 97;916-931.
[85] FINLAY W.H., Nandakumar K., Onset of two-dimensional cellular flow in finite curved channels of large aspect ratio, Phys. Fluids A 2 (7), pp: 1163–1174, 1990.
[86] DEAN W.R., Note on the motion of fluid in a curved pipe, Philos. Mag. 4, pp: 208–223, 1927.
[87] OTTINO J.M., Mixing, chaotic advection and turbulence, Annu. Rev. Fluid Mech. 22, pp: 207–253, 1990.
[88] PELLEGRINI M., ENDO H., NINOKATA H., Numerical investigation of bent pipe flows at trasitional Reynolds number, Progress in Nuclear Energy 53, pp: 916-920, 2011.
[89] JONES S.W., THOMAS O.M., AREF H., Chaotic advection by laminar flow in a twisted pipe, J. Fluid Mech. 209, pp: 335–357, 1989.
[90] CASTELAIN C., MOKRANI A., LEGENTILHOMME P., PEERHOSSAINI H., Residence time distribution in twisted pipe flows: helically coiled system and chaotic system, Exp. Fluids 22, pp: 359–368, 1997.
[91] DOORLY D., SHERWIN S.J., Geometry and flow. In: Formaggia L, Quarteroni A, Veneziani A, editors. Cardiovascular mathematics, vol. 1. Springer; 2009.
[92] AREF H., Stirring by chaotic advection, J. Fluid Mech. 143, pp: 1–21, 1984.
[93] P.M. O'Flynn, G. O'Sullivan and A.S. Pandit, Methods for threedimensional geometric characterization of the arterial vasculature, Ann Biomed Eng 35 (2007), 1368–1381.

[94] C.G. Caro, J.C. Nick and W. Nick, Preliminary comparative study of small amplitude helical and conventional ePTFE arteriovenous shunts in pigs, J R Soc Interface 2 (2005), 261-266.
[95] A.F. Totorean, A.I. Bosioc, **S.I. Bernad** and R. Susan-Resiga, Identification and visualization of vortices in by-pass graft flow, Proceedings of the Romanian Academy Series A 15/1 (2014), 52-59.
[96] J.S. Cole, J.K. Watterson and O. Reilly, Numerical investigation of the haemodynamics at a patched arterial bypass anastomosis, Med Eng Phys 24 (2002), 393-401.
[97] S. Giordana, S.J. Sherwin, J. Peiro, D.J. Doorly, J.S. Crane, K.E. Lee, N.J.W. Cheshire and C.G. Caro, Local and global geometric influence on steady flow in distal anastomoses of peripheral bypass grafts, J Biomech Eng 127 (2007), 1087–1098.
[98] F. Loth, P.F. Fischer and H.S. Bassiouny, Blood flow in end-to-side anastomoses, Annu Rev Fluid Mech 40 (2008), 367–393.
[99] K.V. Canneyt, U. Morbiducci, S. Eloot, G. de Sanstis and P. Verdock, A computational exploration of helical arterio-venous graft designs, Journal of Biomechanics 46 (2013), 345-353.
[100] **S.I. Bernad**, A. Bosioc, E.S. Bernad and M.L. Craina, Comparison between experimentally measured flow patterns for straigth and helical graft, Bio-Medical Materials and Engineering 24 (2014), 853–860.
[101] U. Morbiducci, R. Ponzini, M. Grigionid and A. Redael, Helical flow as fluid dynamic signature for atherogenesis risk in aortocoronary bypass. A numeric study, J Biomech 40 (2007), 519-534.
[102] T.H. Zheng, Y.B. Fan, Y. Xiong, W.T. Jiang and X.Y. Deng, Hemodynamic performance study on small diameter helical grafts, ASAIO J 55\3 (2009), 192-199.
[103] T. Zheng, W. Wang, W. Jiang, X. Deng and Y. Fan, Assessing hemodynamic performances of small diameter helical grafts: transient simulation, Journal of Mechanics in Medicine and Biology 12\1 (2012), 1250008.
[104] G. Coppola and C. Caro, Oxygen mass transfer in a model threedimensional artery, J R Soc 5 (2008), 1067–1075.
[105] A.N. Cookson, D.J. Doorly and S.J. Sherwin, Mixing through stirring of steady flow in small amplitude helical tubes, Ann Biomed Eng 37(2009), 710–721.
[106] Z. Chen, Y.B. Fan, X.Y. Deng and Z. Xu, Swirling flow can suppress flow disturbances in endovascular stents: A numerical study, ASAIO J 55 (2009), 543–549.
[107] F. Zhan, Y.B. Fan and X.Y. Deng, Swirling flow created in a glass tube suppressed platelet adhesion to the surface of the tube: Its implication in the design of small-caliber arterial grafts, Thromb Res 125 (2010), 413–418.
[108] A. Sun, Y. Fan and X. Deng, Numerical comparative study on the hemodynamic performance of a new helical graft with noncircular cross section and swirlgraft, Artificial Organs 34 (2010), 22–27.
[109] **S.I. Bernad**, A. Bosioc, A. Totorean, R. Stanciu and E.S. Bernad, Vortices in By-pass Graft Flow, 11th International Conference of Numerical Analysis and Applied Mathematics (ICNAAM), SEP 21-27, 2013, Greece, AIP Conference Proceedings, 1558 (2013), 160-163.
[110] B. Prabhakarpandian, K. Pant, R. Scott, C. Patillo, D. Irimia, M. Kiani, S. Sundaram, Synthetic microvascular networks for quantitative analysis of particle adhesion, Biomedical Microdevices 10 (4) (2008) 585–595.
[111] F. Migliavacca, G. Dubini, Computational modeling of vascular anastomoses, Biomech Model Mechanobiol 3 (2005) 235–250.
[112] D. Zeng, E. Boutsianis, M. Ammann, K. Boomsma, S. Wildermuth, D. Poulikakos, A study of the compliance of a right coronary artery and its impact on wall shear stress. Journal of Biomechanical Engineering 130 (2008) 041014–11.
[113] A.J. Reininger, U. Heinzmann, C.B. Reininger, P. Friedrich, L.J. Wurzinger, Flow mediated fibrin thrombus formation in an endothelium-lined model of arterial branching, Thrombosis Research 74(6) (1994) 629–641.
[114] V.S. Sottiurai, Distal anastomotic intimal hyperplasia: Histocytomorphology, pathophysiology, etiology, and prevention, International Journal of Angiology 8(1) (1999) 1–10.

[115] M. Sunamura, H. Ishibashi, T. Karino, Flow patterns and preferred sites of intimal thickening in diameter-mismatched vein graft interpositions, Surgery 141(6) (2007) 764–776.
[116] S.W. Lee, D. Smith, F. Loth, P. Fischer and H. Bassiouny, Importance of flow division on transition to turbulence within an arteriovenous graft. Journal of Biomechanics, 40 (2007), 981–992.
[117] U. Morbiducci, R. Ponzini, G. Rizzo, M. Cadioli, A. Esposito, F. Montevecchi and A Redaelli, Mechanistic insight into the physiological relevance of helical blood flow in the human aorta: an in vivo study. Biomechanics and Modeling in Mechanobiology, 10 (2011), 339–355.
[118] I.C. Campbell, L.H. Timmins, D.P. Giddens, R. Virmani, A. Veneziani, S.T. Rab, H. Samady, M.C. McDaniel, A.L. Finn, W.R. Taylor and J.N. Oshinski, Computational Fluid dynamics Simulations of Hemodynamics in Plaque erosion, Cardiovascular Engineering and Technology 4/4 (2013), 464-473.
[119] N. Watanabe, T. Masuda, T. Iida, H. Kataoka, T. Fujimoto and S. Takatani, Quantification of the secondary flow in a radial coupled centrifugal blood pump based on particle tracking velocimetry. Artif Organs, 29 (2005), 26-35.
[120] A.K. Politis, G.P. Stavropoulos, M.N. Christolis, F.G. Panagopoulos, N.S. Vlachos and N.C. Markatos, Numerical modeling of simulated blood flow in idealized composite arterial coronary grafts: Steady state simulations, Journal of Biomechanics, 40 (2007), 1125-1136.

For (b-ii)

[1] Donald E Super, A life-span, life-space approach to career development, Journal of Vocational Behavior, Volume 16, Issue 3, June 1980, Pages 282-298.
[2] Donald Super Developmental self-concept, Downloaded from www.careers.govt.nz.
[3] V.S. Sottiurai, J.S.T. Yao, W.R. Flinn, R.C. Baston, Intimal hyperplasia and neointima: an ultrastructural analysis of thrombosed grafts in humans. Surgery, 93 (1983), 809-17.
[4] Perek B, Malinska A, Stefaniak S, Ostalska-Nowicka D, Misterski M, et al. Predictive Factors of Late Venous Aortocoronary Graft Failure: Ultrastructural Studies. PLoS ONE 8(8): e70628, (2013), doi:10.1371/journal.pone.0070628.
[5] Dhanjoo N Ghista and Foad Kabinejadian, Coronary artery bypass grafting hemodynamics and anastomosis design: a biomedical engineering review, BioMedical Engineering OnLine (2013), 12:129.
[6] Tingting Fan, Yuan Lu, Yan Gao, Jie Meng, Wenchang Tan, Yunlong Huo, Ghassan S. Kassab, Hemodynamics of left internal mammary artery bypass graft: Effect of anastomotic geometry, coronary artery stenosis, and postoperative time, Journal of Biomechanics 49, 645–652, (2016).
[7] **S.I. Bernad**, A. Bosioc, E.S. Bernad, M.L. Craina, Comparison between experimentally measured flow patterns for straigth and helical type graft, Bio-Medical Materials and Engineering, Volume 24/1, (2014), pp: 853-860, DOI 10.3233/BME-130877.
[8] Kyung E. Lee, Jeong S. Lee, Jung Y. Yoo, A numerical study on steady flow in helically sinuous vascular prostheses, Medical Engineering & Physics 33, 38–46, (2011).
[9] U., Morbiducci, R., Ponzini, G., Rizzo, M., Cadioli, A., Esposito, F. M., Montevecchi, A., Redaelli, Mechanistic insight into the physiological relevance of helical blood flow in the human aorta: an in vivo study, Biomech Model Mechanobiol (2011), 10, 339-355.
[10] Caro CG, Cheshire NJ, Watkins N. Preliminary comparative study of small amplitude helical and conventional ePTFE arteriovenous shunts in pigs. Journal of the Royal Society Interface (2005), 2(3):261–6.
[11] Alin F. Totorean, Alin I. Bosioc, **Sandor I. Bernad**, Romeo Susan-Resiga, Critical Flow Regions in the Coronary Bypass Graft Anastomosis, Proceedings of the Romanian

Academy, Series A-Mathematics Physiscs Technical Sciences Information Science, 16 (2):201–208, (2015).

[12] PARK S.-J., KANG, S.-J.,VIRMANI R., NAKANO M., UEDA Y., *In-stent neoatherosclerosis: a final common pathway of late stent failure*, J. Am. Coll. Cardiol., 59, pp: 2051–2057, 2012.

[13] WENTZEL J.J., GIJSEN F.J.H., SCHUURBIERS J.C.H., VAN DER STEEN A.F.W., SERRUYS P.W., *The influence of shear stress on in-stent restenosis and thrombosis*, EuroIntervention, 4 (Supl.C), pp: C27–C32, 2008.

[14] GUNDERT T.J., DHOLAKIA R.J., MCMAHON D., LADISA JR. J.F., *Computational fluid dynamics evaluation of equivalency in hemodynamic alterations between Driver, Integrity, and similar stents implanted into an idealized coronary artery*, J. Med. Devices, 7, 011004, 2013.

[15] MURPHY J.B., BOYLE F.J., *Predicting neointimal hyperplasia in stented arteries using time-dependant computational fluid dynamics: a review*, Comput. Biol. Med., 40, pp: 408–418, 2010.

[16] PANT S., BRESSLOFF N.W., FORRESTER A.I.J., CURZEN N., *The influence of strut-connectors in stented vessels: a comparison of pulsatile flow through five coronary stents*, Ann. Biomed. Eng., 38, pp: 1893–1907, 2010.

[17] MIGLIAVACCA F, MARTINEZ M.A., MALVE M., CHIASTRA C, *On the necessity of modelling fluid–structure interaction for stented coronary arteries*, Journal of the Mechanical Behavior of Biomedical Materials, 34**,** pp: 217–230, 2014.

[18] ELLWEIN L.M., OTAKE H., GUNDERT T.J., KOO B., SHINKE T., HONDA Y., SHITE J., LaDISA JR. J.F., *Optical coherence tomography for patient-specific 3D artery reconstruction and evaluation of wall shear stress in a left circumflex coronary artery*, Cardiovasc. Eng. Technol, 2, pp: 212–227, 2011.